Multi-scale modelling of diamond grown via chemical vapour deposition

William Jeffrey Rodgers

A thesis submitted to the University of Bristol in accordance with the requirements of the Degree of Doctor of Philosophy in the School of Chemistry, Faculty of Science.

September 2014

Abstract

A multi-scale simulation approach has been used to study the theoretical physical and chemical properties of the chemical vapour deposition (CVD) of diamond. A new 3-dimensional kinetic Monte Carlo (kMC) model of CVD diamond growth was developed and implemented. Reactive molecular dynamics simulations using the empirical valence bond (EVB) approach were used to study both the non-equilibrium dissociation and the thermal decomposition of CH_3 from the (100):(2×1):H surface.

In Chapter 3, the systematic exploration of the input parameter space of the 3-D kMC model was completed to determine the sensitivity of the output to changes in the input. This was done in order to validate the model and see if the errors in energetics used for the rate constants which were obtained from experiments and theoretical calculations would produce spurious effects in the kMC model. In this validation procedure it was found that the parameter that most affects the growth rate and surface morphology of the simulated diamond is the concentration of CH_3 above the surface. This investigation also reproduced results observed experimentally which show that a smoother surface is produced with slower growth rates. Finally, for the first time an increase, peak, and decrease in growth rates was observed on the (100) surface as the temperature of the substrate T_s was increased which agrees with experiment.

The kMC model was used to study the effect that the etching of CH_3, the adsorption of CH_3, and the migration of a CH_2 on the surface structure in Chapter 4. Three different models of etching where tested with kMC simulations, as well as a new model for the adsorption of CH_3. The critical nucleus, the smallest unetchable configuration that can nucleate a new layer, was found to be the 2-block dimer in all cases except for two when the migration was turned off.

In Chapter 5 an analytical reactive potential energy surface was created to study the dynamics of methyl dissociation. It was found that the while the non-equilibrium effects on desorption are non-trivial its rate is dwarfed by the rate of the thermal decomposition of CH3 from the (100):(2×1):H surface.

Acknowledgements

Firstly I would like to thank my supervisors, Professors Neil Allan and Jeremy Harvey, for giving me the opportunity to undertake my research here at Bristol. The support and guidance of both of you throughout the process of completing a PhD has been invaluable. Of course finishing this thesis could not have happened without all of the help and tuition that I have received from both of you over the course of my four years here at Bristol. I would also like to thank Professor Paul May whose previous work the work in this thesis is based upon. Also, acknowledgements and thanks to the EPSRC who's funding allowed me the financial resources to pursue this research.

I would also like to thank all members of the Harvey and Allan groups past and present along with all of the other members of the CCC for the discussions scientific and otherwise. Special mention goes to the other members of my cohort Pat, Chris, and Dave. The problem with naming names, you're likely to forget someone; Laura, Richard, Josh, James, Adam, Martina, Stéphanie, Rob, and Clem you've all made my time here at Bristol truly wonderful time. Special mention goes to the Friday evening club! If I've missed anyone out I apologise, but you are probably at least included in that group. Most times the only reason I didn't work from home and commuted in from Cardiff is because of all of you.

Very special mention goes to my Parents. They have always been there for me, no matter how much land and sea have separated us. I would not be the man I am today if it was not for both of you. You are the reason I've made it to where I have! I cannot possibly thank you both enough for all that you have ever done for me. I love you both.

As well as my Parents, I am grateful to have a supporting, understanding, and loving set of 'second' Parents. Thank you so much Chris and Eric for all the encouragement you shown me through my studies.

Finally, but most importantly, this thesis would never have been completed without Sarah. Your love and support not only for the last four years but for the last 14 years has enabled me to do everything that I have. I love you! Thank you!

Declaration

I declare that the work in this thesis was carried out in accordance with the regulations of the University of Bristol and no part of the thesis has been submitted for any other academic award. The work is original, except where indicated by special reference in the text and any work done in collaboration with, or with the assistance of others, is indicated as such. Any views expressed in the thesis are those of the author.

William Jeffrey Rodgers

University of Bristol

September 2014

Table of Contents

List of acronyms

AFM – Atomic force microscopy
B3LYP – Hybrid DFT functional
BDE – Bond dissociation energy
BXD – Boxed molecular dynamics
CASPT2 – Complete active space perturbation theory
CASSCF – Complete active space self-consistent field theory
CCSD(T) – Coupled cluster theory, full treatment of singles and doubles with triples calculated based on many-body perturbation theory
CVD – Chemical vapour deposition
DFT – Density functional theory
EVB – Empirical valence bond
HF- Hot filament
HPHT – High pressure high temperature
KMC – kinetic Monte Carlo
MC – Monte Carlo
MCD – Microcrystalline diamond
MCMM – Multi configuration molecular mechanics
MD – Molecular dynamics
ML - Monolayer
MM – Molecular mechanics
MMFF94 - Merck Molecular Force Field 1994
MWPE – Microwave plasma enhanced
NCD – Nanocrystalline diamond
NN – Nearest neighbour
NVE – Microcanonical statistical ensemble
NVT- Canonical statistical ensemble
PES – Potential energy surface
QM – Quantum mechanics
QM/MM – Quantum mechanics embedded molecular mechanics methods
RMSD – Root mean square standard deviation
SCD – Single crystal diamond
SCF – Self-consistent field theory
TST – Transition state theory
UNCD – Ultra-nanocrystalline diamond
UNCD(HF) - Ultra-nanocrystalline diamond hot filament reactor
UNCD(MW) - Ultra-nanocrystalline diamond microwave plasma enhanced reactor

Chapter 1

Introduction

Diamond has long been prized by human culture as a source of beauty when cut and source of value due to its scarcity in nature. However, materials scientists and engineers prize diamond due to the potential diamond offers thank to its exceptional physical characteristics[1].

1.1. Diamond—more than just a gemstone

Diamond is a metastable allotrope of carbon, that is to say that it is kinetically stable while being thermodynamically unstable. The two most common allotropes of carbon found in nature are graphite (Figure 1 (a)) and diamond (Figure 1 (b)). At standard temperatures and pressures, there is only a 2 kJ mol^{-1} difference in enthalpy between the two with graphite being the lowest and thus the thermodynamically stable allotrope of carbon. However, there is a large kinetic barrier that means that diamond, once formed, is unlikely to decompose

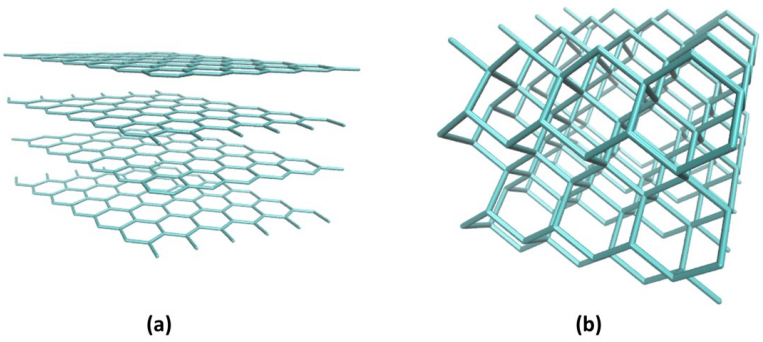

Figure 1-The two most common allotropes of carbon (a) graphite, and (b) diamond

to graphite at standard temperature and pressure, thus making it stable. At 298 K diamond becomes the more stable allotrope at pressures of around 2 GPa. The relation between the different phases of carbon is shown below in Figure 2. This figure has been adapted from extensive study of the characteristics of carbon at many temperatures and pressures by numerous researchers. A review of these studies was produced by Bundy in 1979[2].

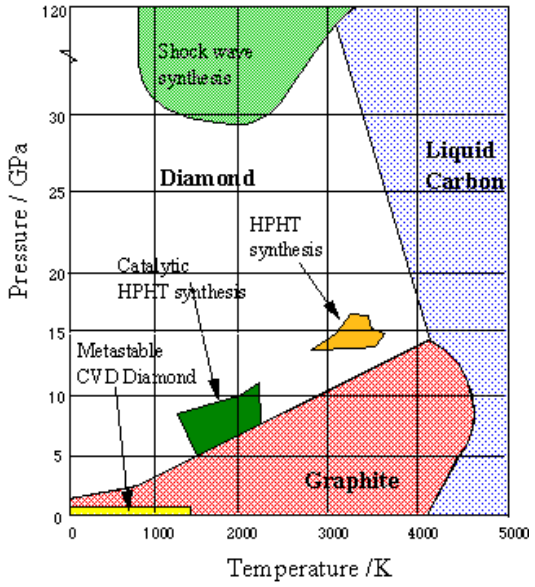

Figure 2-The phase diagram (P, T plot) for carbon reproduced from reference[3], which was adapted from the original source material[2,4,5].

Diamond is formed in nature by a geological process in the depths of the earth's mantle (~150 to 200 km) where the high temperatures and high pressures (~45 to 55 kbar and 1050 to 1200 °C)[6] necessary for their production exist naturally. They are brought to the earth's crust and surface through magma flows and volcanic activity, where they are cooled and normally found in igneous rock formations. This, along with the thermodynamics and kinetics of carbon crystallization, leads to the scarcity of naturally occurring diamond on earth.

1.2. Crystal structure of diamond

A brief description of the crystal structure of diamond is necessary for further discussion of the morphology of diamond later in this thesis. The structure of Diamond, as can be seen in Figure 1 (b), is a system of tetrahedrally coordinated (sp^3 hybridised bonding) carbons[7]. Unlike graphite (Figure 1 (a)) in which the carbons are bonded in a trigonal planar geometry (sp^2 hybridised bonding) with the third electron forming a delocalised π-bond that is free to move between layers. The tetrahedral covalent bonding of all carbons in the diamond structure leads to a very strongly bonded structure, one of the more well know material properties of diamond.

Bulk diamond

An unreconstructed surface of a diamond can be described as a plane through the bulk. These are designated by three numbers called Miller indices (*hkl*) which define the orientation of the plane cut though the bulk crystal relative to a common origin. There are three important planes along which the diamond naturally cleaves the (100), (110), and (111). These faces are important in understanding the synthesis via chemical vapour deposition, so they are presented below in Figure 3.

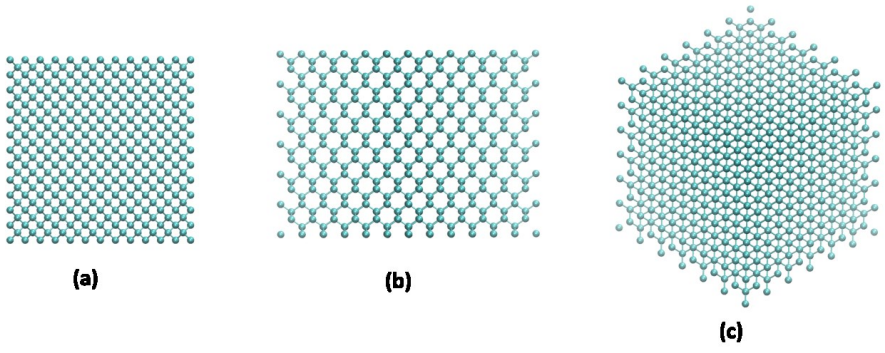

Figure 3-Main crystallographic faces of diamond (a) (100) (b) (110) (c) (111)

Reconstructed (100):(2×1):H surface

The work in this thesis is concerned entirely with the (100) surface of the diamond as this is the surface where most reactions predicted by the standard model of CVD diamond growth occurs. The surfaces of most crystals do not have the same structure as the bulk crystal. The differentiation between the surface and the bulk is called a surface reconstruction; the atoms at the surface form a stable terminating structure. This is the case for diamond and each face of the diamond has its own unique reconstruction. As all carbons in the diamond bulk are tetrahedrally bonded the surface of a slice of the bulk structure will have atoms with excess valence electrons.

The (100) surface of the diamond has what is termed a 2×1 reconstruction. This surface reconstruction consists of a dimer bond, which is two surface atoms whose bond length is shorter than bulk diamond C–C bond; this is notated as the (100):(2×1) surface. Each carbon still has an excess valence electron that bonds with a hydrogen atom. The (100):(2×1):H surface of the diamond is shown in Figure 4. The dimer bonds form in to a closely spaced regular row on the surface. There is a larger trough separating each row from the next. The structure along the direction of the trough this is sometimes referred to as the dimer chain.

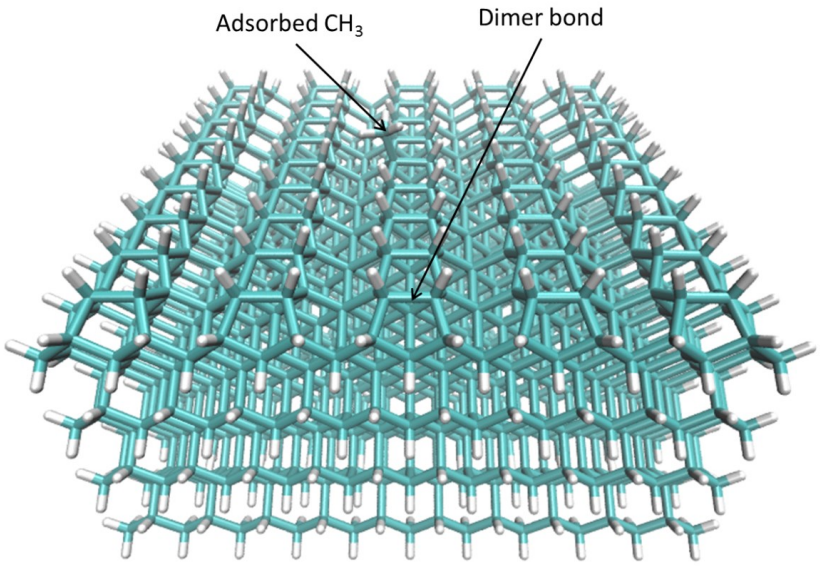

Figure 4-Diamond model looking down on the (100):(2×1):H reconstructed surface

1.3. Material characteristics and uses

It is not an exaggeration to say that diamond is one of the most superlative materials found in nature from an engineering perspective. In a catalogue of material properties commonly sought in science and engineering applications diamond is a very often the highest or the lowest (Table 1). Diamond has the highest thermal conductivity, the lowest compressibility, extreme mechanical hardness and very good wear resistance to name but a few.

Table 1-A list of some of the outstanding material properties of diamond

Mechanical hardness	ca. 90	GPa
Bulk Modulus	1.2	GPa
Compressibility	8.3×10^{-13}	Pa^{-1}
Thermal conductivity	2×10^{3}	$W\ m^{-1}\ K^{-1}$
Speed of sound	17,500	$m\ s^{-1}$
Thermal coefficient of expansion	1×10^{-6}	K
Electrical resistivity	1013	Ω cm

The applications of synthetic diamond are numerous. They range from the obvious and mundane industrial applications to futuristic biomedical uses[8]. The broad optical transparency, high thermal conductivity, and low expansion make diamond an ideal material for high power laser application[9] as well as X-ray lenses[10]. Diamond is naturally an outstanding insulator (5.45 eV band gap) and when doped it becomes a conducting material[11–13]. Its thermal and electrical properties make diamond a perfect candidate for electronic applications. One of the more promising avenues of diamond application are in the biomedical field[14,15]. The bio-inertness of diamond makes it ideal as an implant and *in vivo* uses. There are researchers successfully using flexible diamond microelectrode arrays to implant into the retinas of people born blind in order to act as a light detector as a route to artificial sight[16]. Also functionalised nanodiamonds are being studied for use in the precision chemotherapeutic treatment of cancer patients, precisely targeting the cancer cells with stronger drugs while not affecting the healthy tissue[17]. Diamond truly is a superb material and therefore, due to its scarcity, the only route fully utilizing diamonds fantastic potential is through synthesis.

1.4. Synthetic diamond

Due to its valued status as a superlative engineering material, attempts have been made to synthesise diamonds for over 150 years. It was not until the phase diagram of Carbon was more fully understood by the 1940's that it was actually possible to successfully create synthetic diamond[7,18]. In this section, the two most common routes to diamond synthesis are discussed.

1.4.1. High pressure high temperature diamonds (HPHT)

The first route to producing synthetic diamond logically followed the hypothesized geological process, to attempt to create diamond from graphite under a large pressure at a high temperature. The first synthetic diamond was

produced by this method at the General Electric research laboratories in the late 1950's[19]. Graphite is placed in a hydraulic press so that it is compressible and put under more than 10000 atmospheres of pressure while being heated to more than 2000 K. This process has subsequently been successfully used to produce 'industrial diamond' and is still used today to make diamonds for machining tools, the polishing and grinding of optics, and any industrial activity where the hardness and durability of diamond are useful. However, one of the major drawbacks to this method of making synthetic diamond is that it can only produce single crystal diamond of sizes in the order of magnitude from nanometres to millimetres.

The HPHT method of producing sythetic diamond merely mimics nature. However, it was improved by the use of catalysts to produce diamond closer to the graphite diamond line (Figure 2) and shock wave systhesis which greatly impoved reproducability[18]. While this is useful for many applications, there are a number of engineering applications that would benefit from the use of polycrystalline diamonds which can be grown by the next method described in this chapter.

1.4.2. Chemical vapour deposition (CVD) of diamond

A method for synthesising diamond in a way that does not imitate nature was discovered in the late 1950's. Experiments at the Union Carbide company with carbon containing gases in sub-atmospheric pressures produced diamond growth on an existing diamond substrate[20]. A review of the history of the chemical vapour deposition of diamond is beyond the scope of this thesis but the history from Eversole to the present can be found in textbooks[7,18,21] and review articles[1]. It is sufficient to say that the chemical vapour deposition of diamond is now a mature field but there are still unanswered questions about the theoretical mechanisms behind CVD diamond growth[22].

Growth of diamond via CVD starts with the addition of a mixture of H_2 and a small amount (generally ~ 1-5%) of CH_4 into a low pressure vessel(typically in

the order of 20 Torr)[23]. This mixture of gas (sometimes containing partial fractions of Ar, N, and other gases) then passes through an activation region where the excess energy dissociates the H_2 molecules into $2H\cdot$ and the CH_4 into various radical carbon containing molecules. This radical 'soup' of molecules, shown below in Figure 5, then flows and reacts above the substrate surface creating more complex hydrocarbons. Some of these hydrocarbons then diffuse to the growing substrate where gas-surface reactions contribute to the growing diamond surface.

Figure 5 is a generalised picture of what happens in a non-specific CVD reactor for growing diamond. There are numerous types of reactors that have been used to produce diamond via CVD. There are two types however which dominate the field; these are the hot filament (HF) reactor and the microwave plasma enhanced reactor (MWPE) both described below.

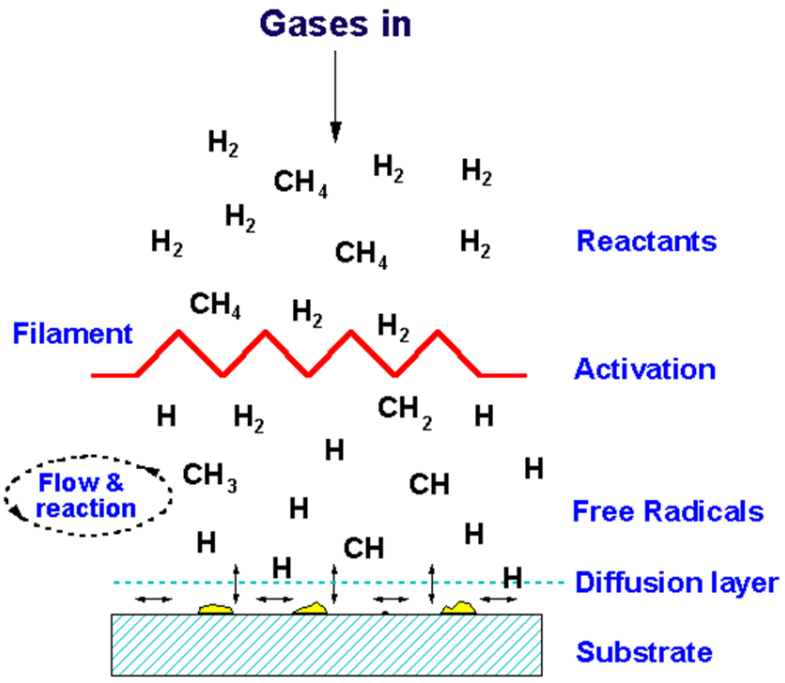

Figure 5-Diagram of general CVD reactor showing the main process occurring (reproduced from[1])

Different types of diamond grown via CVD are discussed throughout this thesis. CVD reactors can grow single crystal diamond (SCD) as well as polycrystalline diamond film with crystal size ranging from mm called microcrystalline diamond (MCD), to 100 – 5 nm in size which are called nanocrystalline and ultrananocrystalline diamond (NCD & UNCD).

Hot filament CVD reactor

The distinguishing property of a hot filament (HF) CVD reactor is in its name. The method by which the process gases are activated is a metal wire filament, usually made of tungsten or tantalum. This wire is resistively heated to around 2000 K which heats the gas in the activation region adding energy to the system and initiating the H dissociation described above. The substrate is heated by a separate device. The nascent diamond film is generally grown from a silicon (Si) or molybdenum (Mo) substrate, which has a crystal structure similar to diamond, seeded with diamond nanoparticles as nucleation sites. A diagram containing the important parts of an HF CVD reactor is shown in Figure 6.

The advantages of this method of producing diamond are that it is a relatively inexpensive and established technique, however it does have a number of undesirable side effects; the first being that the filament degrades over time, resulting in a smaller growth period than other methods. Particles from the degrading filament can also become incorporated in the growing diamond as impurities. This eliminates this method as a way to produce high purity diamonds for electronic purposes. Finally, the filament restricts the types of gases that can be used in the process because certain gases can oxidise or otherwise corrupt the filament prematurely.

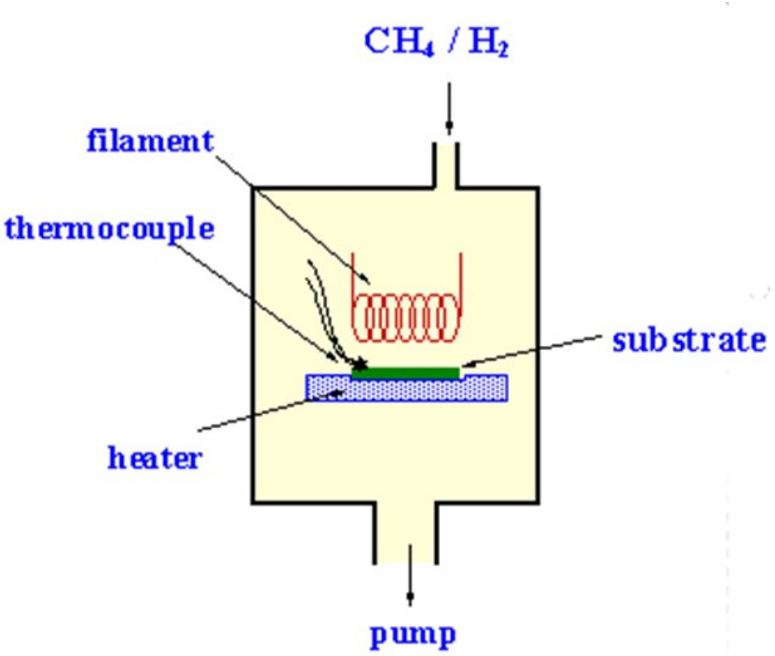

Figure 6-Schematic diagram of a hot filament (HF) CVD reactor reproduced from[1]

Microwave plasma enhanced CVD reactor

The solution to many of the problems presented by HF CVD reactors are solved by the microwave plasma enhanced (MWPE) CVD reactor. This type of reactor is the state of the art in producing high quality synthetic diamond films and single crystals. A schematic of a MWPE CVD reactor is shown in Figure 7, and as was the case for the HF reactor the name of the reactor is indicative of the way in which the gases are activated. The activation of an electron plasma gas is created by energy from the microwave radiation coupling with the electrons in the incoming process gases. The gas then reacts and diffuses between the activation area and the growing substrates. The plasma gas typically heats the substrate negating a separate heating apparatus.

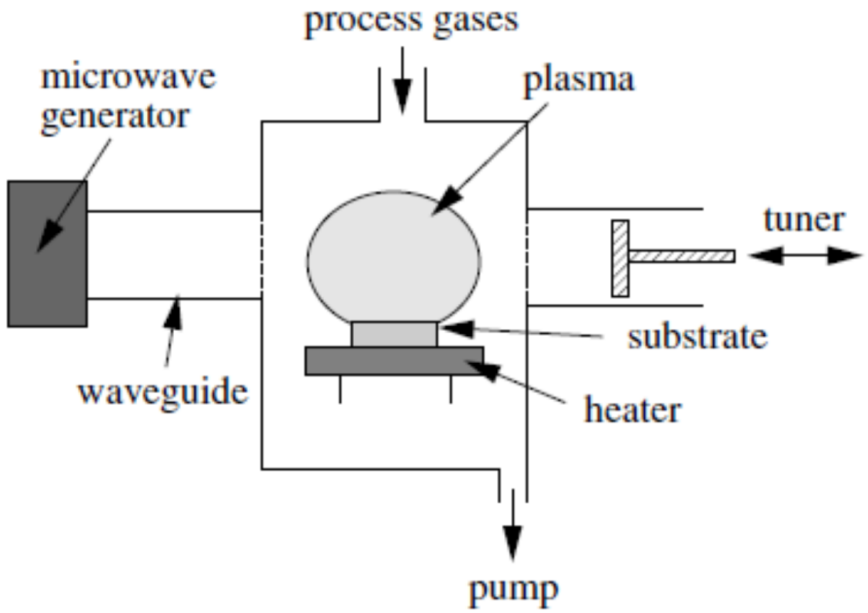

Figure 7-Schematic diagram of a microwave (plasma enhanced) CVD reactor reproduced from[1]

1.5. Theoretical modelling of CVD diamond

The research contained in this thesis is concerned with the theoretical modelling of various aspects relating to the chemical vapour deposition of diamond. In this section a brief overview of the theoretical research in CVD diamond growth is presented.

The CVD process is an inherently multi-scale process. There are macro scale properties such as gas flow rates and temperature, mesoscale phenomena such as diffusion, and microscopic chemical reactions. In order to accurately model the growth of diamond by CVD it is necessary to model processes that occur on disparate time and space scales. Thus multiple approaches are required. In this section the multi-scale modelling of diamond growth is discussed with a brief review of the literature of research that has gone before.

1.5.1. Gas phase reactions

The first aspect of the reactor that requires attention is the complex chemistry occurring in the gas phased in the reactor after the process gases have been activated (Figure 5). Comprehensive research done in collaboration between the diamond group at Bristol University and Moscow State University has resulted in a detailed model, described by Mankelevich et al.[24,25] and Ma et al.[26], of the gas phase chemistry in CVD reactors.

The 2D theoretical model calculates the temperature variation and the mole fraction of gas concentration above the surface. This model has been extensively validated though the precise monitoring of the plasma during growth experiments with optical emission and cavity ring-down spectroscopy.[25] A 2D model is sufficient as the concentration of gases only vary in the vertical direction of the reactor and is symmetrical about the central heat source. This model was used to estimate the concentration of gas-phase species above the growing diamond surface used in the kinetic Monte Carlo (kMC) model introduced in Chapter 2. In Figure 8a below is a plot of the concentration of certain gas-phase species as a function of height above the surface from z = 0 to 50 mm. There is a large variation of the concentration of all the gases over this range. For the kMC the concentration close to the surface needs to be known in order to estimate the flux of reactive species on the surface. Figure 8b shows an expanded scale of the same data which has been extrapolated to near the surface by the fitting of a power law expression in the form of $[X]=pz^q$ where [X] is the concentration of the gas, z is the height above the surface, and p and q are fitting parameters. The data in Figure 8 is taken from a simulation of a reactor that produces single crystal growth, but similar simulations were performed to produce data for the following reactors; microcrystalline (MCD), nanocrystalline (NCD), UNCD (HF) ultra nanocrystalline (hot filament), and UNCD (MW) ultra nanocrystalline (microwave).

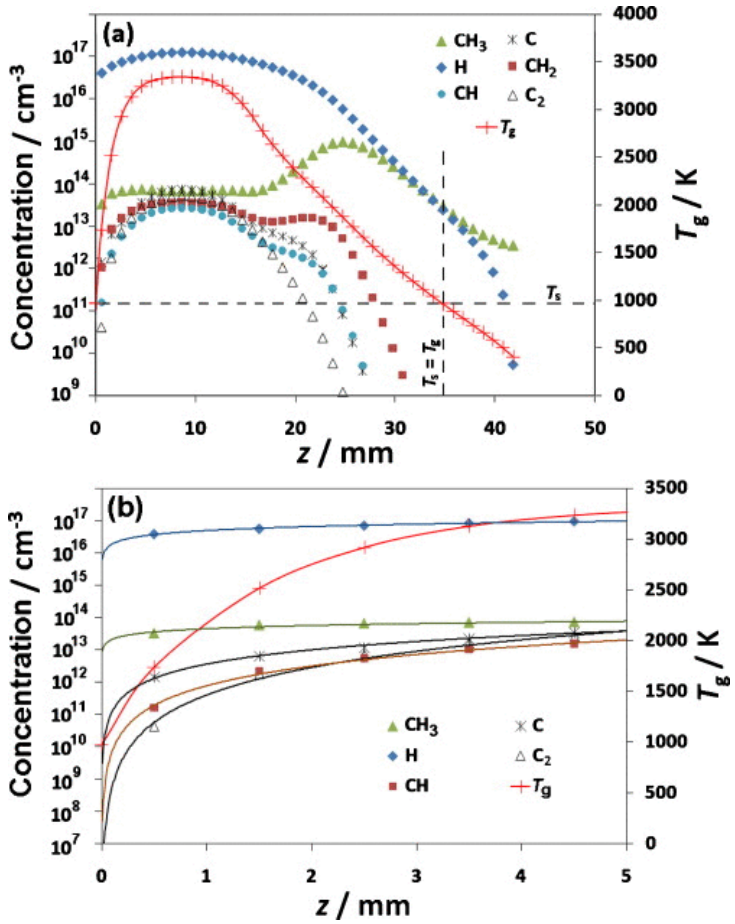

Figure 8-Concentration of some of the gas-phase species above the diamond surface simulated for a MW plasma under single crystal diamond (SCD) growth conditions using the 2D model described above. (a) The full data set from z=0 to 50 mm (b) is the same data on an expanded scale near the substrate with curves showing an extrapolation of the data to near the surface (~z=0 mm). (figure reproduced from [27])

1.5.2. Gas surface reactions

In order to understand how the chemical vapour deposition of diamond works from a theoretical basis, it is necessary to understand the chemistry of the chemical reactions occurring at the surface. This is a molecular and atomistic process which requires another level of simulation. As chemical reactions require knowledge of the position of the electron it is a quantum process. Therefore quantum mechanical electronic structure calculations are required to understand

the energetics of a reaction on the diamond surface. These methods are only mentioned in passing here, but are discussed further in Chapter 2. Reactions can be proposed from the chemical intuition of a research and then the energetics of these reactions are determined through calculations and experiments to determine their likelihood.

Many researchers' mechanisms for growth have been proposed over the last three decades[23,28,29]. Electronic structure calculations were used to investigate the energetics of proposed mechanisms to determine the likelihood of these being possible reactions leading to carbon incorporation into the growing diamond lattice[30–35]. While the main chemical species responsible for diamond growth has not been conclusively determined, it is generally accepted in the CVD diamond community that the methyl radical is the most likely candidate. The 'standard growth' mechanism was generally accepted to proceed via the route shown by the 1990's.

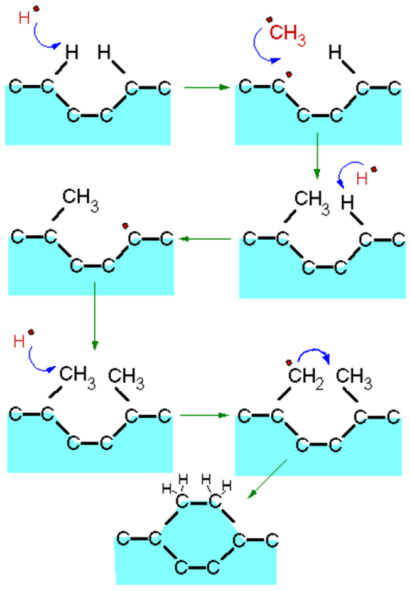

Figure 9-Diagram of the accepted 'standard growth' model for CVD diamond reproduced from[1]

More recent work done by our group in Bristol used this method to look at the energetics involved in boron doping[36] of diamond and more pertinent to this

thesis, the incorporation of carbon on (100) diamond surface (see Chapter 3)[37]. An example of one of the potential energy surfaces calculated for this study is shown below in Figure 10. This is the insertion of a CH_3· into a dimer bond on the (100) surface. This is another possible route to carbon inclusion in the diamond structure. This study suggests that the primary mechanism by which diamond grows under CVD conditions is by the route shown in Figure 10. A methyl is inserted into a reconstructed surface dimer by a ring opening and closing mechanism. This is slightly different from the 'standard model' illustrated above, but it still considers the CH_3 radical as the main growth species.

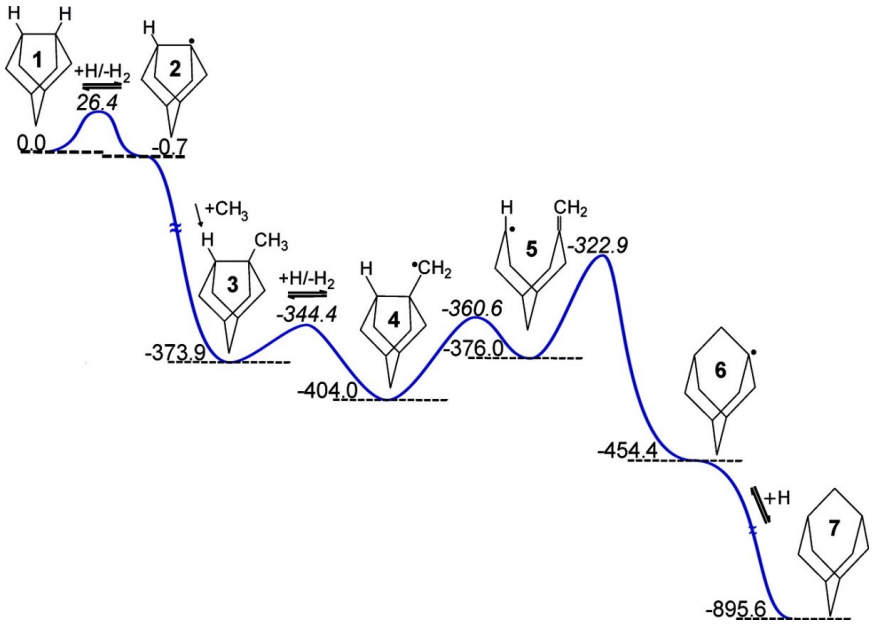

Figure 10-Reaction path (energies are in kJ mol^{-1}) for incorporating a +CH_3· into a C-C dimer bond (figure taken from Cheesman et al[37])

1.5.3. Kinetic Monte Carlo models

Understanding which reaction mechanisms are possible is useful, but by itself not capable of providing information about the macroscopic properties observed experimentally, such as growth rates, surface roughness, and crystal size. Another type of modelling is needed to bridge the length and timescale differences between micro and macroscopic phenomena. The kinetic Monte

Carlo (kMC) method does this and will be discussed in more detail in the next chapter. However some of the relevant kMC models of diamond growth in the literature are discussed in this section.

Battaile et al.[38] were the first to use previous energetics studies to create a rate catalogue for a kMC simulation. This model reproduced some growth rates for the (111) surface of diamond that compared favourably with experiments[39]. It also produced surfaces with qualitatively compared surface morphologies and no quantitative measurement. The work of Battaile et al. had the problem of accurate estimation of the rate constants for processes due to the nature of the level of electronic structure theory available at the time. The most recent state of the art in kMC models for CVD diamond growth was developed and presented by Netto and Frenklach.[40] They modelled the (100) surface and used an updated kinetic catalogue with better kinetic data and a relatively rigorous estimation of the gas concentrations which determine the flux of growth species. Netto and Frenklach produced some growth rates that agreed with experiments and calculated the surface roughness but did not relate this measure to diamond grown via CVD. The model also failed to reproduce the peak and subsequent decrease of growth rates of the (100) surface observed experimentally[41].

1.6. Aims and outline of thesis

Work presented in this thesis has used various theoretical and computational techniques to study the chemical vapour deposition of diamond. A particular focus of this thesis is on the mechanisms that affect the structure of the surface. The kinetics of the etching of carbon from the (100):(2×1):H surface was studied. This along with other kinetic information was used in a kinetic Monte Carlo model of CVD diamond growth with was developed in the course of this work to study macroscopic effects on diamond growth. A brief outline of this thesis follows.

- Chapter 2 – Theoretical methods

- In this chapter the main theoretical methods used in the rest of the thesis are briefly introduced and discussed.

- Chapter 3 – 3-dimensional kinetic Monte Carlo model of diamond grown by chemical vapour deposition (CVD)
  - The 3-dimensional kinetic Monte Carlo model of CVD diamond growth developed for this work is presented. Extensive testing of the parameter space of the program is presented as a validation and test of the sensitivity of output.
- Chapter 4 – Surface morphology
  - Three surface restructuring processes are systematically tested to determine their effect on the resultant surface morphology of diamond simulated using the kMC model outlined in Chapter 3.
  - Three different models for etching and two models for CH_3 adsorption are included in these tests.
- Chapter 5 – Studies of methyl desorption
  - An analytical reactive potential energy surface (PES) is created from accurate electronic structure calculation. This PES is used to study the thermal decomposition as well as the non-equilibrium dissociation of CH_3 from the (100):(2×1):H surface of diamond.
- Chapter 6 - Conclusions

1.7. References

(1) May, P. W. Diamond Thin Films: A 21st-Century Material. *Philos. Trans. R. Soc. Lond. Ser. Math. Phys. Eng. Sci.* **2000**, *358*, 473–495.

(2) Bundy, F. P. The P, T Phase and Reaction Diagram for Elemental Carbon, 1979. *J. Geophys. Res. Solid Earth* **1980**, *85*, 6930–6936.

(3) Cheesman, A. Investigations into the Fundamentals of Gas-Phase and Gas-Surface Chemistry Prevalent in Growth of Chemical Vapour Deposited Diamond Films, University of Bristol, 2006.

(4) Bundy, F. P. Pressure-Temperature Phase Diagram of Elemental Carbon. *Phys. Stat. Mech. Its Appl.* **1989**, *156*, 169–178.

(5) Bundy, F. P.; Bassett, W. A.; Weathers, M. S.; Hemley, R. J.; Mao, H. U.; Goncharov, A. F. The Pressure-Temperature Phase and Transformation Diagram for Carbon; Updated through 1994. *Carbon* **1996**, *34*, 141–153.

(6) Erlich, E.; Hausel, W. D. *Diamond Deposits: Origin, Exploration, and History of Discovery*; SME, 2002.

(7) Field, J. E. *The Properties of Natural and Synthetic Diamond*; Academic Press, 1992.

(8) Lettington, A. H. Applications of Diamond-like Carbon Thin Films. *Carbon* **1998**, *36*, 555–560.

(9) Sabella, A.; Piper, J. A.; Mildren, R. P. 1240 Nm Diamond Raman Laser Operating near the Quantum Limit. *Opt. Lett.* **2010**, *35*, 3874–3876.

(10) Alianelli, L.; Sawhney, K. J. S.; Malik, A.; Fox, O. J. L.; May, P. W.; Stevens, R.; Loader, I. M.; Wilson, M. C. A Planar Refractive X-Ray Lens Made of Nanocrystalline Diamond. *J. Appl. Phys.* **2010**, *108*, 123107.

(11) Gildenblat, G.; Grot, S.; Badzian, A. The Electrical-Properties and Device Applications of Homoepitaxial and Polycrystalline Diamond Films. *Proc. Ieee* **1991**, *79*, 647–668.

(12) K, D. H.; J, T. D.; A, K. R. U. Single Crystal Chemical Vapor Deposited Synthetic Diamond Material Used in E.g. Electronic, Optical Applications Has a Specific Total as-Grown Nitrogen Concentration and a Uniform Distribution of Defects.

(13) Bustarret, E.; Gheeraert, E.; Watanabe, K. Optical and Electronic Properties of Heavily Boron-Doped Homo-Epitaxial Diamond. *Phys. Status Solidi A* **2003**, *199*, 9–18.

(14) Tang, L.; Tsai, C.; Gerberich, W. W.; Kruckeberg, L.; Kania, D. R. Biocompatibility of Chemical-Vapour-Deposited Diamond. *Biomaterials* **1995**, *16*, 483–488.

(15) Schrand, A. M.; Hens, S. A. C.; Shenderova, O. A. Nanodiamond Particles: Properties and Perspectives for Bioapplications. *Crit. Rev. Solid State Mater. Sci.* **2009**, *34*, 18–74.

(16) Bergonzo, P.; Bongrain, A.; Scorsone, E.; Bendali, A.; Rousseau, L.; Lissorgues, G.; Mailley, P.; Li, Y.; Kauffmann, T.; Goy, F.; et al. 3D Shaped Mechanically Flexible Diamond Microelectrode Arrays for Eye Implant Applications: The MEDINAS Project. *Irbm* **2011**, *32*, 91–94.

(17) Huang, H.; Pierstorff, E.; Osawa, E.; Ho, D. Active Nanodiamond Hydrogels for Chemotherapeutic Delivery. *Nano Lett.* **2007**, *7*, 3305–3314.
(18) Liu, H.; Dandy, D. S. *Diamond Chemical Vapor Deposition*; Material science and process technology series; Noyes publications: Park Ridge, NJ, 1995.
(19) Bovenkerk, H. P.; Bundy, F. P.; Hall, H. T.; Strong, H. M.; Wentorf, R. H. Preparation of Diamond. *Nature* **1959**, *184*, 1094–1098.
(20) G, E. W. Synthesis of Diamond. US3030188 A, April 17, 1962.
(21) Prelas, M. A.; Popovici, G.; Bigelow, L. K. *Handbook of Industrial Diamonds and Diamond Films*; CRC Press, 1997.
(22) Butler, J. E.; Mankelevich, Y. A.; Cheesman, A.; Ma, J.; Ashfold, M. N. R. Understanding the Chemical Vapor Deposition of Diamond: Recent Progress. *J. Phys. Condens. Matter* **2009**, *21*, 364201.
(23) Goodwin, D. G.; Butler, J. E. Chapter 11. In *Handbook of industrial Diamond and Diamond Films*; Prelas, M. A.; Popovici, A.; Bigelow, L. K., Eds.; Marcel Dekker Inc., 1998; pp. 527–581.
(24) Mankelevich, Y. A.; Ashfold, M. N. R.; Ma, J. Plasma-Chemical Processes in Microwave Plasma-Enhanced Chemical Vapor Deposition Reactors Operating with C/H/Ar Gas Mixtures. *J. Appl. Phys.* **2008**, *104*, 113304.
(25) Mankelevich, Y. A.; Ashfold, M. N. R.; Comerford, D. W.; Ma, J.; Richley, J. C. Boron Doping: B/H/C/O Gas-Phase Chemistry; H Atom Density Dependences on Pressure and Wire Temperature; Puzzles Regarding the Gas-Surface Mechanism. *Thin Solid Films* **2011**, *519*, 4421–4425.
(26) Ma, J.; Richley, J. C.; Davies, D. R. W.; Ashfold, M. N. R.; Mankelevich, Y. A. Spectroscopic and Modeling Investigations of the Gas Phase Chemistry and Composition in Microwave Plasma Activated B2H6/CH4/Ar/H2 Mixtures. *J. Phys. Chem. A* **2010**, *114*, 10076–10089.
(27) May, P. W.; Harvey, J. N.; Allan, N. L.; Richley, J. C.; Mankelevich, Y. A. Simulations of Chemical Vapor Deposition Diamond Film Growth Using a Kinetic Monte Carlo Model and Two-Dimensional Models of Microwave Plasma and Hot Filament Chemical Vapor Deposition Reactors. *J. Appl. Phys.* **2010**, *108*, 114909.
(28) Harris, S. J. Mechanism for Diamond Growth from Methyl Radicals. *Appl. Phys. Lett.* **1990**, *56*, 2298–2300.
(29) Frenklach, M.; Skokov, S.; Weiner, B. An Atomistic Model for Stepped Diamond Growth. *Nature* **1994**, *372*, 535–537.
(30) Huang, D.; Frenklach, M.; Maroncelli, M. Energetics of Acetylene-Addition Mechanism of Diamond Growth. *J. Phys. Chem.* **1988**, *92*, 6379–6381.
(31) Huang, D.; Frenklach, M. Potential Energy Calculations of Diamond Growth by Methyl Radicals. *J. Phys. Chem.* **1991**, *95*, 3692–3695.
(32) Skokov, S.; Weiner, B.; Frenklach, M. Elementary Reaction Mechanism for Growth of Diamond (100) Surfaces from Methyl Radicals. *J. Phys. Chem.* **1994**, *98*, 7073–7082.
(33) Frenklach, M.; Skokov, S. Surface Migration in Diamond Growth. *J. Phys. Chem. B* **1997**, *101*, 3025–3036.
(34) Skokov, S.; Weiner, B.; Frenklach, M. Chemistry of Acetylene on Diamond (100) Surfaces. *J. Phys. Chem.* **1995**, *99*, 5616–5625.

(35) Butler, J. E.; Woodin, R. L.; Brown, L. M.; Fallon, P. Thin Film Diamond Growth Mechanisms [and Comment]. *Philos. Trans. R. Soc. Lond. Ser. Phys. Eng. Sci.* **1993**, *342*, 209–224.
(36) Cheesman, A.; Harvey, J. N.; Ashfold, M. N. R. Computational Studies of Elementary Steps Relating to Boron Doping during Diamond Chemical Vapour Deposition. *Phys. Chem. Chem. Phys.* **2005**, *7*, 1121–1126.
(37) Cheesman, A.; Harvey, J. N.; Ashfold, M. N. R. Studies of Carbon Incorporation on the Diamond {100} Surface during Chemical Vapor Deposition Using Density Functional Theory. *J. Phys. Chem. A* **2008**, *112*, 11436–11448.
(38) Battaile, C. C.; Srolovitz, D. J.; Butler, J. E. A Kinetic Monte Carlo Method for the Atomic-Scale Simulation of Chemical Vapor Deposition: Application to Diamond. *J. Appl. Phys.* **1997**, *82*, 6293–6300.
(39) Battaile, C. C.; Srolovitz, D. J. Kinetic Monte Carlo Simulation of Chemical Vapor Deposition. *Annu. Rev. Mater. Res.* **2002**, *32*, 297–319.
(40) Netto, A.; Frenklach, M. Kinetic Monte Carlo Simulations of CVD Diamond growth—Interlay among Growth, Etching, and Migration. *Diam. Relat. Mater.* **2005**, *14*, 1630–1646.
(41) Kweon, D.-W.; Lee, J.-Y.; Kim, D. The Growth Kinetics of Diamond Films Deposited by Hot-filament Chemical Vapor Deposition. *J. Appl. Phys.* **1991**, *69*, 8329–8335.

Chapter 2

Theoretical Background

2.1. Introduction

The chemical kinetics of gas-surface and surface reactions lies at the heart of understanding the theoretical basis behind the chemical vapour deposition of diamond (CVD). These reactions are atomistic by nature, and thus occur on time and length scales of an order of Å and ps respectively. The feasibility of these reactions can be probed by molecular simulation methods. Free energies can be obtained via these methods and within the framework of transition state theory (TST) the rate constants of these reactions can be estimated. A certain amount of chemical intuition is required to propose reaction mechanisms to test in this manner. However, even then, it is difficult to connect these molecular reactions to the macroscopic picture of growth observed experimentally. This is because the macroscopic features of growth are a sum of multiple reactions occurring many times over a long time span.

This final product of CVD diamond growth occurs at time and length scales of an order cm and hours respectively. The disparate time and length scales that separate the molecular reactions underpinning growth and the resultant grown diamond pose a significant problem when trying to understand how the atomistic description of growth affects the macroscopic product. This is where the kinetic Monte Carlo method plays an important role. The kMC method, described below, allows a simulation to follow the state to state trajectory of each reaction when the respective rate constant for each process is supplied to the model. This allows the user to follow the micro-structural

evolution of diamond given a certain set of atomistic reactions governing the system.

In this chapter only the basic theory behind the methods used in this research is discussed. This theory is expanded upon in much more detail in numerous textbooks. [1,2] The more technical and specific methods used to obtain the different results in this research are presented before the appropriate results section in later chapters.

2.2. Electronic structure theory

In order to study the reactivity of a set of chemical species it is necessary to consider the electrons of the system in question. The electron is a sub-atomic particle, a fermion, and classical mechanics fail to describe their interactions. The quantum state of the electron is described by a wave function, conventionally known as Ψ. The electronic wave function of any given chemical species is described by the stationary states predicted by the time independent Schrödinger equation (Equation 1) where $\hat{H}$ is the Hamiltonian operator and E is the potential energy of the state described by Ψ. This equation describes the quantum mechanics (QM) of a particle or molecule.

$$\hat{H}\psi = E\psi \tag{1}$$

There are numerous ways to find the approximate solution to the Schrödinger equation for a given system. It is not the goal of this chapter to describe the many different QM electronic structure methods. It is sufficient to say that the most important methods used in the current state of the art of research can be grouped into two main types; *ab initio* and density functional theory (DFT) methods. The basic theory of methods used for the electronic structure calculations performed in this work is discussed here. There is a considerable amount of literature devoted to the thorough derivation and explanation of these methods and we direct the reader to these for more detail.[2]

2.2.1. Density functional theory (DFT)

Density functional theory (DFT) is an extensively used method in electronic structure calculations as it is computationally cheaper than high level *ab initio* methods, while still giving accurate relative energies. This method, initially developed by Kohn and Sham,[3] is theoretically exact for the electronic ground state energy which is determined by the electron density.[4] The general form of the energy as a function of the electron density is shown in Equation 2 where $T_s[\rho]$ is the kinetic energy of non-interacting electrons, $E_{ne}[\rho]$ is the electron nucleus energy, $J[\rho]$ is the Coulombic electron-electron repulsion energy, and $E_{xc}[\rho]$ is the exchange correlation energy (which includes the additional energetic contributions not include in the previous terms mentioned). While the exact ground state energy is a function of the electron density, the form of this functional is as yet unknown so DFT remains an approximate approach.

$$E_{DFT}[\rho] = T_s[\rho] + E_{ne}[\rho] + J[\rho] + E_{xc}[\rho] \quad (2)$$

All of the energy terms in the equation can be found exactly, except for the exchange-correlation functional, $E_{xc}[\rho]$. Finding an appropriate form for the exchange correlation functional is one of the main problems of DFT. The energy functional can be approximated by fitting parameters to certain sets of molecules based on higher level *ab initio* data,[2] and there are also some known theoretical constraints that the exact exchange-correlation functional must respect. Depending on how these two approaches are combined, there are many approximate functionals available. A popular hybrid functional that has proved accurate for many types of chemistry is the B3LYP functional.[5,6] This is a hybrid functional, which means that it includes a portion of the Hartree-Fock or "exact" expression for the exchange energy within the exchange-correlation functional. The B3LYP functional has proved useful in the field of solid state chemistry,[7] and is used to produce results presented in Chapter 5.

2.2.2. *Ab initio* methods

Ab initio methods are a class of methods that solve the Schrödinger equation by approximating the wave function. One of the most basic of these and one of the first to be developed is the Hartree-Fock method. Some of the first ab initio calculations performed on a computer for simple molecules were Hartree-Fock calculations in the 1950's.[8] This method is computationally simple but not very accurate for most systems. A classic example is the method's inability to predict the curve for the dissociation of H_2 correctly. Some of the work presented in Chapter 5 was done using highly accurate wave function methods, called post Hartree-Fock methods.[9] These methods are used for the accurate treatment of the diradical state resulting from the dissociation of CH3 from neopentane. Hartree-Fock methods overestimate these types of energies. The methods used in this work, CASSCF corrected CCSD(T), are considered the 'gold standard' of quantum chemistry calculations.[10]

2.3. Molecular mechanics

Solving the Schrödinger equation to find the potential energy of a system is the most accurate way of modelling molecular interactions and necessary when modelling reactions, specifically covalent bond breaking. However, as the size of the molecular system increases the cost of the calculation scales considerably. Molecular mechanics (MM) uses simple analytical expressions to calculate the potential energy of a set of interacting particles. This expression is evaluated much faster, and provides a much more efficient way to calculate the potential.

Interactions between non-bonded atoms are obtained by modelling the particles as spheres with a defined radius and charge both of which are determined by either experiment or ab initio quantum calculations. Simple Columbic and Lenard-Jones potentials are used here. Additionally, for atoms that are chemically bonded there are additional terms based on Hooke's law describing the stretching and bending of these bonds. The force fields are

parameterised functions that are developed for certain types of molecules which share similarities in their interactions. The combination of the functional form of these terms and the parameters constitutes the force field for the system being considered. These are determined using a combination of data from experiments and electronic structure calculations like the sphere radius and charge mentioned above. Force fields contain many different functions which are summed for each particle to calculate the total potential energy of a system. These functions are divided into two classes of interactions these terms are described below. In this work the MMFF94[11–16,16,17] set of force fields was used for most of the MM work as they are well parameterised for hydrocarbon chemistry.

2.3.1. MMFF94 energy

The MMFF94 energy is calculated as a sum of bonded and non-bonded energies shown in Equation 3. The bonded energies include E_{bond}, the energy of the bond stretch, E_{θ} the energy of the bond angle, $E_{stretch\text{-}bend}$, E_{OOP} the out of plane bending energy term, and $E_{torsion}$ the torsional bending energy term. The non-bonded terms include the van der Waals and electrostatic interactions.

$$E_{MMFF94} = E_{bond} + E_{\theta} + E_{stretch-bend} + E_{OOP} + E_{torsion} + E_{vdW} + E_{electrostatic} \quad (3)$$

The bond stretching energy term, E_{bond}, is based on Hooke's law. Many MM force fields use a quadratic form for this term. While this is computationally efficient, it can produce energies that are too large for some elongated bonds. The MMFF94 force field uses a quartic form (Equation 4) which produces more accurate energies for bond lengths stretched beyond equilibrium.

$$E_{bond} = \sum_{ij} K_{bond}(r_{ij} - r_{ij}^{o})^2 \left(1 + cs(r_{ij} - r_{ij}^{o}) + \frac{7}{12}\left(cs^2(r_{ij} - r_{ij}^{o})^2\right)\right) \quad (4)$$

The E_{bond} term is summed over two bonded atoms i and j with a bond length of $r_{ij.}$ The fitted terms include r_{ij}^{o} which is the reference bond length, K_{bond} is the force constant, and cs a cubic term stretch constant.

The angle bending energy term is in a cubic form. The change in energy due to a change in angle, θ_{ijk}, between three atoms i, j, and k is determined by

equation 5 where θ_{ijk}^{o} is the reference angle, K_θ is the force constant, and *cb* is the cubic bending parameter.

$$E_\theta = \sum_{ijk} K_\theta(\theta_{ijk} - \theta_{ijk}^{o})^2 \left(1 + cb\left(\theta_{ijk} - r\theta_{ijk}^{o}\right)\right) \quad (5)$$

There is also a nonlinear stretch-bend (Equation 6) term that includes effects from both bond stretching and angle bending. The fitted terms are similar to those found in Equations 4 and 5 but unique to the $E_{stretch-bend}\ term$.

$$E_{stretch-bend} = \sum_{ijk}\left(K_{ijk}\left(r_{ij} - r_{ij}^{o}\right) + K_{kji}\left(r_{kj} - r_{kj}^{o}\right)\right)\left(\theta_{ijk} - r\theta_{ijk}^{o}\right) \quad (6)$$

The next term in the force field is a quadratic term for the out of plane bending, E_{OOP} (Equation 7), this term is sometimes known as the improper torsional energy term in other force fields. A schematic diagram of this type of bending angle is shown in Figure 11. Here K_{OOP} is the empirical force constant and $\chi_{ijk;l}$ is the angle, known as the Wilson angle,[18] illustrated in the figure below.

$$E_{OOP} = \sum_{ijk;l} K_{OOP}(\chi_{ijk;l})^2 \quad (7)$$

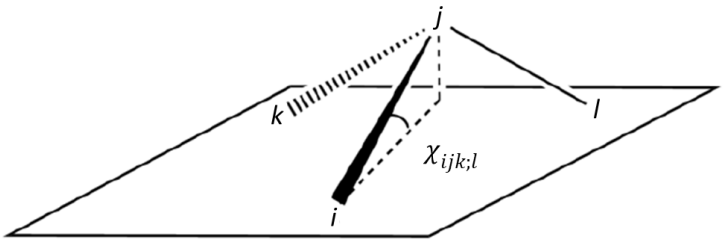

Figure 11-Schmatic diagram of the improper torsion or out of plane bending angle

The E_{OOP} term is important when simulating benzene type planar molecule. This term helps to preserve planarity in these types of molecules.

The final term modelling bonded interactions is the torsional energy term (Equation 8). This is the energy associated with the rotation of a molecule about a bond. In Figure 12 an ethane molecule is used to demonstrate the torsion angle.

$$E_{torsion} = \sum_{ijkl} \frac{1}{2}\left(V_1(1 + \cos\Phi) + V_2(1 + \cos 2\Phi) + V_3(1 + \cos 3\Phi)\right) \quad (8)$$

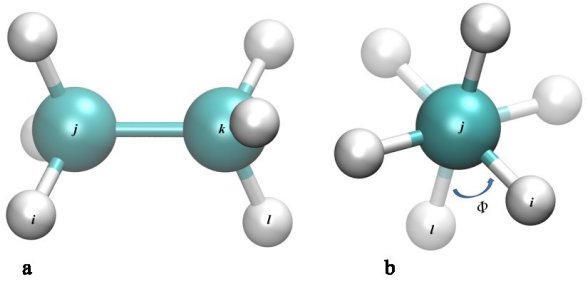

Figure 12-Ethane molecule used to show the torsion angle Φ about bond j-k

The angle Φ is the dihedral angle about the bond j-k. The torsional energy term is a sum of three periodic repeating functions where V_i is a fitted force constant.

The final two terms in the force field describe the non-bonded interactions between the particles. The electrostatic interaction between particles is described by a modified columbic form (Equation 9). This calculates the potential energy due to two point charges q_i and q_j separated by a distance R_{ij}; ε_0 is the dielectric constant and δ is a small electrostatic buffering constant (δ=0.05) to prevent electrostatic collapse.

$$E_{electrostatic} = \frac{332.071 q_i q_j}{\varepsilon_0 (R_{ij}+\delta)} \tag{9}$$

The final term takes into account all of the other non-bonded interactions in the form of the van der Waals interaction (Equation 10). The MMFF94 family of force fields employs a non-standard form for the van der Waals interaction called a 'buffered-14-7' form.[11]

$$E_{vdW} = \sum_{ij} \varepsilon_{ij} \left(\frac{1.07 R_{ij}^*}{R_{ij}+0.07 R_{ij}^*} \right)^7 \left(\frac{1.12 {R_{ij}^*}^7}{{R_{ij}}^7+0.07 {R_{ij}^*}^7} - 2 \right) \tag{10}$$

R_{ij}^* is the minimum-energy separation for unlike pairs i and j, included to prevent collapse at short inter-nuclear distances. The term ε_{ij} determines the well depth and is a function which includes both like and unlike pairs interaction terms.

2.4. Molecular dynamics

Molecular dynamics (MD) simulations propagate a system of particles interacting on a potential energy surface through space and time. This is done by numerically integrating[19] Newton's classical equations of motion (4). In this equation, **r** is the coordinate vector of a particle and V is the potential energy of the particle calculated using the MM force field.

$$\frac{-dV}{d\mathbf{r}} = m\frac{d^2\mathbf{r}}{dt^2} \tag{4}$$

The main advantage of an MD simulation is of course being able to evolve the real physical dynamic trajectory of a system and learn about its structural evolution. Another advantage of a time dependent simulation of a very large system is the ability to take time averages of the entire system. These average properties can then be related to macroscopic observables using statistical mechanics (discussed further in Section 1.5). However, before examining the different facets of an MD simulation, the technique for solving the equations of motion of a large system is discussed.

2.4.1. Numerical integration

In a system of many particles, there will be a number of differential equations in the form of Equation 4, and they will be coupled to each other making an analytical solution impossible. Thus these differential equations must be solved numerically by a computer. In order to do this the equations of motion are discretised using the finite difference method.

Verlet algorithm

The most common algorithm for solving the equations of motion in this manner is the Verlet algorithm developed in 1967.[19] By expanding the position ***r*** both forward and backward in time in a Taylor series, equations 5 and 6 are obtained. In these equations v_i are the velocities at time step i, a_i is the set of

instantaneous atomic accelerations, and b_i is the set of third derivative of the positions r_i.

$$\mathbf{r}_{i+1} = \mathbf{r}_i + v_i\Delta t + \frac{1}{2}a_i(\Delta t)^2 + \frac{1}{6}b_i(\Delta t)^3 + \cdots \quad (5)$$

$$\mathbf{r}_{i-1} = \mathbf{r}_i - v_i\Delta t + \frac{1}{2}a_i(\Delta t)^2 - \frac{1}{6}b_i(\Delta t)^3 + \cdots \quad (6)$$

Adding these two together and solving for r_{i+1} gives Equation 7:

$$\mathbf{r}_{i+1} = (2\mathbf{r}_i - \mathbf{r}_{i-1}) + a_i(\Delta t)^2 + \cdots \quad (7)$$

This is the basis of the Verlet algorithm, which has the obvious problem of no information about the velocities of the particles being directly generated from the numerical integration. There is a modified form known as the velocity-Verlet algorithm which calculates the position (Equation 8, a truncated Equation 5) and the velocity explicitly at the same time step (Equation 9).

$$\mathbf{r}_{i+1} = \mathbf{r}_i + v_i\Delta t + \frac{1}{2}a_i(\Delta t)^2 \quad (8)$$

$$v_{i+1} = v_i + \frac{a_i + a_{i+1}}{2}\Delta t \quad (9)$$

The so called leapfrog modification of the Verlet integration algorithm is also used in this work. The velocities are calculated at time i+½ initially using Equation 10 and then the positions are calculated at time i+1. The name derives from the positions 'leapfrogging' over the previously calculated velocities by ½ time step. The advantage of this method is that it explicitly calculates velocities, but not at the same time as the positions.

$$v_{i+\frac{1}{2}} = v_{i-\frac{1}{2}} + a_i\Delta t \quad (10)$$

$$\mathbf{r}_i = \mathbf{r}_{i-1} + v_{i-\frac{1}{2}}\Delta t \quad (11)$$

2.4.2. Thermostats

For MD simulations in the canonical ensemble (see below) there is a need to maintain a constant average temperature. This can be achieved in numerous ways, but in the work a Langevin thermostat has been used. This means that a stochastic force, *f'* is added to the sum of forces, *f*(*r*), acting on each particle in the

manner described by Equation 12, where ζ is the friction coefficient which is a small.[2,8]

$$ma = -\zeta v + f(r) + f' \quad (12)$$

This thermostat method requires fewer computations per time step so long thermal equilibrations are more efficient. However, this method does influence momentum transfer,[8] but this is not a problem in this work as temperature dependent simulations are used to equilibrate a system.

2.5. Statistical mechanics

The subject of statistical mechanics is concerned the study of large systems of particles where the exact state of each individual particle is unknown. The average behaviour of such systems is considered, and as such probability theory is used to describe them. These systems are divided into statistical ensembles which describe the average behaviour of a collection of systems.[20,21] Molecular dynamics simulations can reproduce the conditions required by these ensembles. Two types of ensembles were used in the work presented in this thesis and are shown below.

2.5.1. Statistical Ensembles

The canonical ensemble N, V, T

The canonical ensemble represents all of the possible states of a system which is in thermal equilibrium with a heat bath. It is often referred to as an NVT ensemble as the following quantities have to remain constant; the number of particles (N), the volume of the system (V), and the temperature of the system (T). In practice an NVT molecular dynamics simulation requires a thermostat maintain the average temperature of the system. The thermostat used in this work was discussed in section 2.4.2 above. NVT simulations are used in this work to equilibrate a system to a certain temperature be NVE simulations are performed.

The microcanonical ensemble N, V, E

The microcanonical ensemble represents all the possible states of a system with a defined constant total energy. It is also known as the NVE ensemble which refers to the constant quantities; number of particles in the system (N), the volume of the system (V), and the total amount of energy in the system(E). This ensemble is used in this work to study the flow of energy though a system over a short time scale. In order to obtain a realistic physical result from these NVE simulations they must begin with the right initial conditions. A snapshot of positions and velocities from an NVT simulation of the system at the desired physical temperature; this simulation much be in thermal equilibrium with the temperature bath, which means if should be run for a sufficient period of time.

2.5.2. Transition state theory (TST)

The transition state of a system is the highest point on a free energy surface between a reactant and a product. The difference in energy from the reactant to the product is the Gibbs free energy of activation $\Delta G^{\ddagger}$ (Figure 13). In its most basic form, classical transition state theory[22] (TST) relates the rate of a reaction to the Gibbs free energy of activation by the Eyring equation[23] (Equation 5).

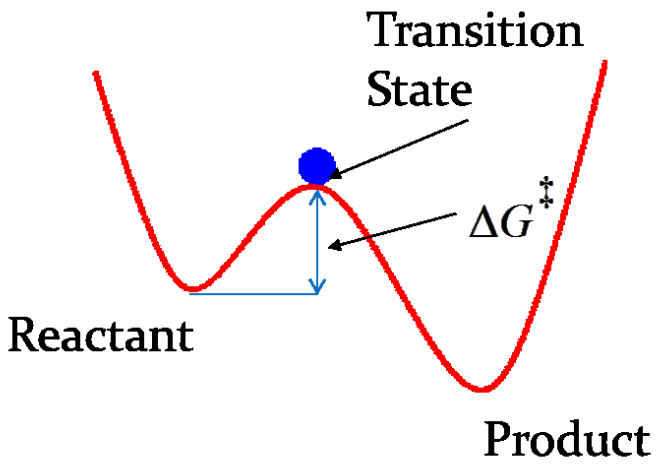

Figure 13-Diagram of a potential energy surface of a reaction with the activated complex at the transition state.

$$k = \frac{k_B T}{h} e^{-\Delta G^{\ddagger}/RT} \tag{13}$$

In this work the Eyring equation (Equation 13) is used to calculate the rate constants of unimolecular reactions for inclusion in the kinetic Monte Carlo model.

2.6. Kinetic Monte Carlo method

The work presented in this thesis is concerned with simulating the growth of synthetic diamond via chemical vapour deposition (CVD, see Chapter 1). The individual atomistic processes governing the growth of diamond occur at much smaller time scales (ps) than the experimental observables of growth rate and surface morphology (hr). The time scales of the individual reactions make them amenable to study by molecular dynamics simulations. In fact, growth mechanisms previously unknown can be elucidated by molecular dynamics simulations on an accurate potential energy surface. There have been studies of this type conducted recently by the Bogaerts group in Antwerp in order to determine how C_xH_y gas species react with the surface at step edges.[24]

In theory it is possible to simulate the growth of diamond on an accurate potential surface up to the point where macroscopic properties of diamond are observable. In practice this is impossible, as the computational expense would by far outstrip the current state of the art. One of the main reasons that this problem is computationally intractable with MD methods is due a large contribution from rare events in the system and the other is that simulations must have a small enough time step to accurately resolve the fastest atomic vibrations. Take for instance the 2D potential contour surface presented in Figure 14. A molecule bound in the central well will potentially spend a considerable amount of time in that well before transition over the reaction barrier into another well. This transition could take anywhere between 1fs and 1s of molecular dynamics simulation time, the latter being a considerable about of time for one molecule. The same thing is happening for every molecule in the simulation obviously quickly leading to a problem beyond the reach of current computing technology.

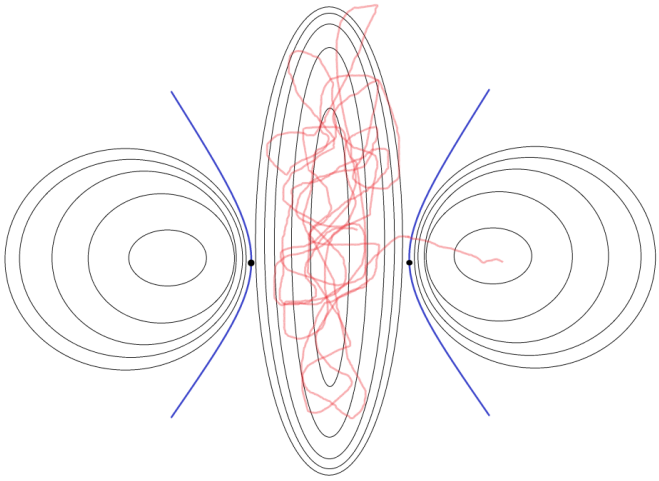

Figure 14-A simple 2d potential energy contour plot used to illustrate a rare event system. The red line illustrates the trajectory of a particle confined within a well for a certain time before transitioning into an adjacent potential well.

The kinetic Monte Carlo (kMC) method can evolve the state to state dynamics of a complicated system with numerous infrequent events in an accelerated manner. In order for the kMC method by itself to accurately predict the

dynamics of system modelled a complete catalogue of all possible transitions must be known. It is necessary to know the rate constant for each transition. Transition state theory allows the determination of the rate constant for a unimolecular reaction. By using highly accurate *ab initio* methods to calculate the Gibbs free energy of a likely reaction profile the rate constant for that reaction can be estimated using equation 5. The simulated trajectory of the system is propagated via a weighted probability of each possible transition occurring.

In Figure 15 the algorithm for the implementation of the kMC method is shown in a flow chart. At each Monte Carlo (MC) time step the rate for each process is determined. These are stored in an ordered array of rates, *r(i)*; an example of this is shown below in Figure 16a. A random number u between (0, 1] is chosen. The rates are summed into an ordered array of sums, *S(j)*, in the manner shown by Figure 16Figure 15. The cumulative sum of all of the rates, the final number in the array *S(j)*, is then multiplied by the random number u. This new number points to the process in array *r(i)* via Equation 14.

$$\sum_{i=1}^{i-1} r_i < u \cdot S(i) \leq \sum_{i=i+1}^{k_{tot}} r_i \tag{14}$$

The simulation time is then updated stochastically by incrementing t_{total} by Δt shown in Equation 15 below.

$$\Delta t = \frac{\log(u)}{S(k_{tot})} \tag{15}$$

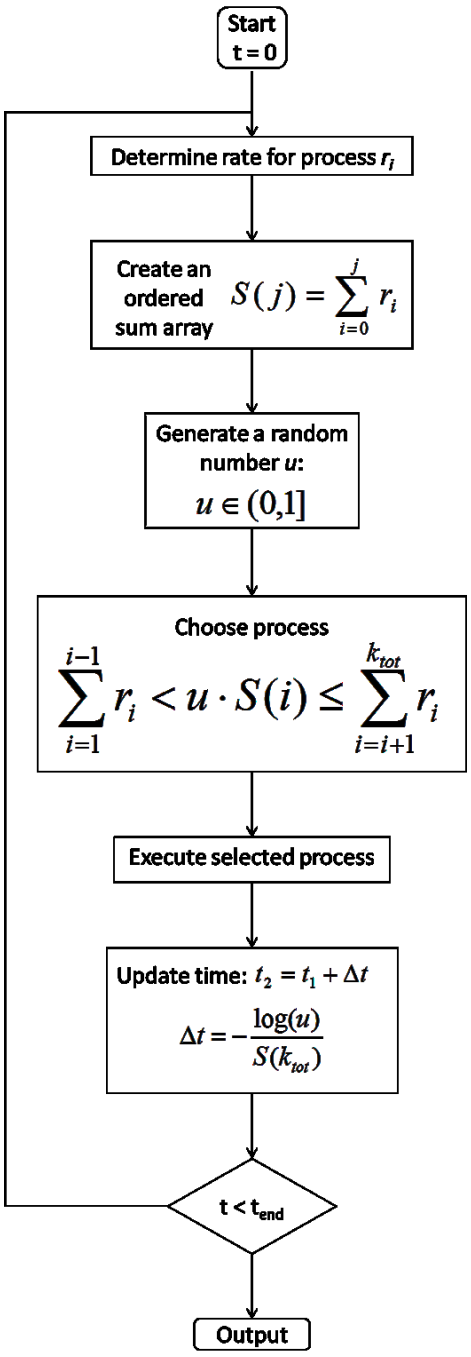

Figure 15-The kinetic Monte Carlo algorithm as implemented in this work.

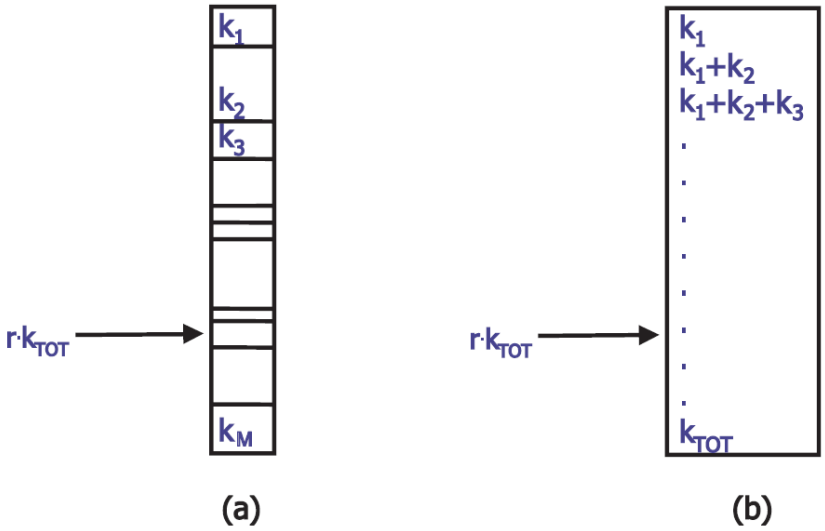

Figure 16-The kinetic rate catalogue (a) is a list of all of the rate constants for each possible transition in the system and (b) is the order list of sums of these rates.

This algorithm is then repeated until the desired length of simulation time has been achieved. In practice, this method can reproduce state to state dynamics of a system on the order of almost any time (depending on the rates). The advantage to using the kMC over molecular dynamics is that every time step is a transition, whereas in MD the time scales of the simulation might only allow one transition to occur. The disadvantage of the kMC method is that if every possible transition in the system is not known, which is the case for all but the simplest of systems, then the method is not exact and may not even be useful if the rate catalogue is too poorly considered.

2.7. References

(1) Frenkel, D.; Smit, B. *Understanding Molecular Simulation: From Algorithms to Applications*; Academic Press, 2001.

(2) Jensen, F. *Introduction to Computational Chemistry*; John Wiley & Sons, 2007.

(3) Kohn, W.; Sham, L. J. Self-Consistent Equations Including Exchange and Correlation Effects. *Phys. Rev.* **1965**, *140*, A1133–A1138.

(4) Hohenberg, P.; Kohn, W. Inhomogeneous Electron Gas. *Phys. Rev.* **1964**, *136*, B864–B871.

(5) Becke, A. D. Density-functional Thermochemistry. III. The Role of Exact Exchange. *J. Chem. Phys.* **1993**, *98*, 5648–5652.

(6) Stephens, P. J.; Devlin, F. J.; Chabalowski, C. F.; Frisch, M. J. Ab Initio Calculation of Vibrational Absorption and Circular Dichroism Spectra Using Density Functional Force Fields. *J. Phys. Chem.* **1994**, *98*, 11623–11627.

(7) Corà, F.; Alfredsson, M.; Mallia, G.; Middlemiss, D. S.; Mackrodt, W. C.; Dovesi, R.; Orlando, R. The Performance of Hybrid Density Functionals in Solid State Chemistry. In *Principles and Applications of Density Functional Theory in Inorganic Chemistry II*; Structure and Bonding; Springer Berlin Heidelberg, 2004; pp. 171–232.

(8) Leszczynski, J. *Handbook of Computational Chemistry*; Springer Science & Business Media, 2011.

(9) Bartlett, R. J.; Stanton, J. F. Applications of Post-Hartree—Fock Methods: A Tutorial. In *Reviews in Computational Chemistry*; Lipkowitz, K. B.; Boyd, D. B., Eds.; John Wiley & Sons, Inc., 1994; pp. 65–169.

(10) Watts, J. D.; Gauss, J.; Bartlett, R. J. Coupled-cluster Methods with Noniterative Triple Excitations for Restricted Open-shell Hartree–Fock and Other General Single Determinant Reference Functions. Energies and Analytical Gradients. *J. Chem. Phys.* **1993**, *98*, 8718–8733.

(11) Halgren, T. A. Merck Molecular Force Field. I. Basis, Form, Scope, Parameterization, and Performance of MMFF94. *J. Comput. Chem.* **1996**, *17*, 490–519.

(12) Halgren, T. A. Merck Molecular Force Field. I. Basis, Form, Scope, Parameterization, and Performance of MMFF94. *J. Comput. Chem.* **1996**, *17*, 490–519.

(13) Halgren, T. A. MMFF VI. MMFF94s Option for Energy Minimization Studies. *J. Comput. Chem.* **1999**, *20*, 720–729.

(14) Halgren, T. A. Merck Molecular Force Field. II. MMFF94 van Der Waals and Electrostatic Parameters for Intermolecular Interactions. *J. Comput. Chem.* **1996**, *17*, 520–552.

(15) Halgren, T. A. Merck Molecular Force Field. III. Molecular Geometries and Vibrational Frequencies for MMFF94. *J. Comput. Chem.* **1996**, *17*, 553–586.

(16) Halgren, T. A.; Nachbar, R. B. Merck Molecular Force Field. IV. Conformational Energies and Geometries for MMFF94. *J. Comput. Chem.* **1996**, *17*, 587–615.

(17) Halgren, T. A. MMFF VI. MMFF94s Option for Energy Minimization Studies. *J. Comput. Chem.* **1999**, *20*, 720–729.
(18) Wilson, E. B. *Molecular Vibrations: The Theory of Infrared and Raman Vibrational Spectra*; Courier Dover Publications, 1955.
(19) Verlet, L. Computer "Experiments" on Classical Fluids. I. Thermodynamical Properties of Lennard-Jones Molecules. *Phys. Rev.* **1967**, *159*, 98–103.
(20) Chandler, D. Introduction to Modern Statistical Mechanics. *Introd. Mod. Stat. Mech. David Chandl. Pp 288 Foreword David Chandl. Oxf. Univ. Press Sep 1987 ISBN-10 0195042778 ISBN-13 9780195042771* **1987**, *-1*.
(21) Gibbs, J. W. *Elementary Principles in Statistical Mechanics: Developed with Especial Reference to the Rational Foundation of Thermodynamics*; Cambridge University Press, 2010.
(22) Laidler, K. J.; King, M. C. Development of Transition-State Theory. *J. Phys. Chem.* **1983**, *87*, 2657–2664.
(23) Eyring, H. The Activated Complex in Chemical Reactions. *J. Chem. Phys.* **1935**, *3*, 107–115.
(24) Eckert, M.; Neyts, E.; Bogaerts, A. Differences between Ultrananocrystalline and Nanocrystalline Diamond Growth: Theoretical Investigation of CxHy Species at Diamond Step Edges. *Cryst. Growth Des.* **2010**, *10*, 4123–4134.
(25) Voter, A. F. INTRODUCTION TO THE KINETIC MONTE CARLO METHOD. In *Radiation Effects in Solids*; Sickafus, K. E.; Kotomin, E. A.; Uberuaga, B. P., Eds.; NATO Science Series; Springer Netherlands, 2007; pp. 1–23.

Chapter 3

3–dimensional kinetic Monte Carlo (kMC) model of diamond grown by chemical vapour deposition (CVD)

In this chapter the development of a novel 3–dimensional kinetic Monte Carlo (kMC) computational model for chemical vapour deposition grown (CVD) diamond is discussed. This model is an extension of extensive theoretical work on diamond growth previously carried out by the Bristol University diamond group.[1–7] A fully 3-dimensional kMC program simulating CVD diamond growth was written in Fortran 90 (Appendix). After the development of the new model extensive sensitivity analysis was carried out to evaluate its strengths and weaknesses. These tests are included in the results at the end of this chapter.

3.1. Chemical model of growth

The kMC model of growth requires two types of information: first, which type of molecular species is being modelled, and secondly what type of chemical reactions can occur to each of these species. By knowing all of the elements in these two sets of information (a non–trivial exercise) a detailed dynamic, macroscopic simulation of diamond growth can be obtained.[8] In practice, it is not possible to know every potential reaction and product in any complicated system. However, if the important pieces of information for a system are known, then a relatively accurate kMC simulation can hopefully be achieved, though it is possible that the gaps in the microscopic process catalogue can cause certain macroscopic affects to be missed.[9,10] A kMC model can be an ideal platform to

test potential reaction mechanisms for CVD diamond growth as hypothetical kinetic mechanisms can be included in the system and the resulting simulation can be analysed to determine how the macroscopic growth is affected. Here with detailed sensitivity testing to understand its limitations, we aim to generate an accurate microscopic model of reaction mechanisms leading to a simulation with macroscopic characteristics which can be directly compared to experimental growth results.

The growth of diamond by CVD is essentially a steady state non–equilibrium process. A complicated set of chemical reactions, discussed in Chapter 1, governs this process. These reactions can be divided into two distinct sets: gas phase reactions and surface reactions. For the purposes of this description, reactions that include gas–surface interactions are considered surface reactions. This study is only explicitly concerned with surface reactions, the kinetic rates of which are included in the kMC catalogue. However, the kMC model does depend on an accurate knowledge of the gas phase reactions. As the concentration of different molecules above the surface directly determine the rates of reaction for certain surface and adsorption processes. The surface reactions are discussed here, but the modelling of the gas phase reactions was discussed in Chapter 1.

3.1.1. Molecular species

There are six distinct molecular species explicitly included in the model, and one which is implicit. Each species represents a molecular 'group' that can react on the (100) surface of diamond with other species in predefined ways, with a known rate. These species and their approximation in the model are described below.

An **inactivated surface species** represents a hydrogen terminated carbon on the surface. This corresponds to half of a dimer pair on the (2x1):(100):H reconstructed diamond surface. An **activated surface species** corresponds to half of a surface dimer with no terminating hydrogen, thus leaving a 'dangling bond'

on the surface. This surface radical is the primary route to growth in the model, whereby a CH_x is bonded to form an ad species. The CH_3 molecule is the most common species near the surface and the reaction path, examined by Cheesman et al. [6], by which it is inserted into the dimer bond is shown in Figure 10 from the introduction chapter is the most probable mechanism contributing to growth. In the model the end point of this reaction is represented by the **inactivated ad species**. This species corresponds to an isomerisation between a CH_3 molecule and a CH_2 bridge species between the two dimer carbons. This ad species can then be 'activated' by a hydrogen abstraction reaction thus becoming an **activated ad species.** This process can occur two more times producing a **doubly activated ad species**, and a **triply activated ad species**.

3.1.2. Kinetic processes

The chemical reactions involved in CVD diamond growth (Table 2) and used by the kMC model are described here. A simple and instructive way of illustrating these processes is to describe a sample simulation in which all of these processes occur. The initial conditions of this simulation consist of a small (N×N) grid of **inactivated surface species** with other gas and temperature settings, not yet described, which are arbitrarily sufficient to produce simulated diamond growth.

Table 2– Reactions for each process included in model and their associated rate constants. C_d represents a carbon bonded into the diamond surface, and * represents a missing C in the lattice. (see below for description of all the processes).

Process	Reaction	Rate constant
a) Surface activation Ad–species activation	**(i)** $^{\bullet}H(g) + HC_d–C_dH \rightarrow {}^{\bullet}C_d–C_dH + H_2(g)$ **(ii)** $HC_d–C_dH \rightarrow {}^{\bullet}C_d–C_dH + {}^{\bullet}H(g)$ **(iii)** $H(g) + CH_{x(1–3)}–C_d–C_dH \rightarrow {}^{\bullet}CH_{x(0–2)}–C_d–C_dH + H_2(g)$ **(iv)** $CH_{x(1–3)}–C_d–C_dH \rightarrow {}^{\bullet}CH_{x(0–2)}–C_d–C_dH + H(g)$	$k_{activate}$
b) Surface deactivation Ad–species deactivation	**(i)** $H_2(g) + {}^{\bullet}C_d–C_dH \rightarrow H(g) + HC_d–C_dH_d$ **(ii)** $H^{\bullet}(g) + {}^{\bullet}C_d–C_dH \rightarrow HC_d–C_dH_d$ **(iii)** $H_2(g) + {}^{\bullet}CH_{x(0–2)}–C_d–C_dH \rightarrow H(g) + CH_{x(1–3)}–C_d–C_dH$ **(iv)** $H^{\bullet}(g) + {}^{\bullet}CH_{x(0–2)}–C_d–C_dH \rightarrow CH_{x(1–3)}–C_d–C_dH$	$k_{deactivate}$
c) CH_2/CH_3 etch	$H(g) + {}^{\bullet}C_d–C_dH \rightarrow {}^{*}–C_dH + CH_3(g)$	k_{etch}
d) CH_x add	$CH_x(g) + {}^{\bullet}C_d–C_dH \rightarrow {}^{\bullet}CH_x–C_d–C_dH$	$k_{CHx–add}$
e) Migration in 4 directions	$H–C_d–CH_2–C_d–H \ldots {}^{\bullet}C_d–C_d–H \rightarrow H–C_d–{}^{\bullet}C_d \ldots H–C_d–CH_2–C_d–H$	$k_{migration}$
f) Sticking in 4 directions	$H–C_d–CH_2–C_d–H \ldots H–C_d– C_dH_2–C_d–H \rightarrow$ $H–C_d–C_dH_2–C_d–H \ldots H–C_d–C_dH_2–C_d–H$	$k_{migration}$
g) β scission	$H(g) + CH_3–CH_2–C_d–C_dH \rightarrow {}^{\bullet}C_d–C_dH + CH_3(g)$	k_{β}
h) Surface radical migration	$HC_d–C_dH \ldots {}^{\bullet}C_d–C_dH \rightarrow HC_d–C_d{}^{\bullet} \ldots HC_d–C_dH$	See text

Surface activation

To start this mock example simulation one site, inevitably an inactive surface site, is chosen on the grid and the only possible process which can occur to it is a surface activation (Table 1(a)). This process is modelled as a combination of two surface reactions. The first is an abstraction reaction of surface terminal hydrogen by an energetic •H radical from the gas phase producing an activated surface species, or a 'dangling bond' on the surface, and an H_2 molecule in the gas phase (reaction a–i, table 1). The second but much slower process is the thermal decomposition of an inactivated surface species into an activated surface species and a gas phase •H radical (reaction a–ii, table 1). The rate constant for surface activation is a linear combination of the rate constants for these two reactions (Equation 1) multiplied by the concentrations of surface sites that can be activated. The rate constants for the individual reactions a–i and a–ii are given in equations 2 and 3 below.

$$k_{activate} = (k_{a-i}[H] + k_{a-ii})N_a \quad (1)$$

$$k_{a-i} = A_{a-i}\sqrt{T_{ns}}\, exp\left(-\frac{E_{a-i}}{T_s}\right) \quad (2)$$

$$A_{a-i} = 3.2 \times \frac{10^{-12}}{s^{-1}}, E_{a-i} = 3430/K \quad (2a)$$

$$k_{a-ii} = 1.66 \times 10^{-11}\exp\left(-\frac{49675}{T_s}\right) \quad (3)$$

The pre–exponential factors and energy terms for the rate constants in Equations 2,3,5 and 6 are taken from previous experimental kinetic studies of hydrogen reactions on the diamond surface.[5, 11] Krasnoperov and Kalinovski performed extensive experimental and theoretical research on the kinetics of H and CH3 reactions on the diamond surface. The experimental errors measured in the activation energies (~ 1 kcal mol^{-1}) and exponential prefactors for the rate constants of these reactions range from 3% to 8 %. These are very accurate experiments and by testing the sensitivity of output for the kMC simulation program to variations in the data within the experimental errors given above more confidence can be placed in the results of the simulations affected by this

process. Since the activation of the surface is critical for the addition of any new species it is therefore vital that this process is modelled as accurately as possible.

Surface deactivation

Now in this hypothetical simulation, there is one activated surface species. If this surface site is chosen to advance the simulation, then there are two possible processes which can occur; surface deactivation and CH_X addition. Surface deactivation is the reverse process of surface activation and in this model the rate is determined by the reverse reactions of those described in the previous section. The rate constant, $k_{deactivate}$ (Equation 4) is a linear combination of the rate constants (Equations 5 and 6) for reactions b–i and b–ii (Table 1) and the concentrations of [H•] and [H_2] in the gas phase directly above the surface.

$$k_{deactivate} = (k_{b-ii}[\mathrm{H}] + k_{b-i}[\mathrm{H_2}])N_\mathrm{d} \tag{4}$$

$$k_{b-ii} = 9.6 \times 10^{-13}\sqrt{T_\mathrm{ns}} \tag{5}$$

$$k_{b-i} = 3.2 \times 10^{-13}\sqrt{T_\mathrm{ns}}\exp\left(-\frac{7850}{T_\mathrm{s}}\right) \tag{6}$$

This is the per site rate constant and is multiplied by the total number of possible deactivation sites on the reacting surface to get the absolute rate constant per time step for surface deactivation.

The ratio of the concentration of surface radical sites (active) and hydrogen terminated surface sites (inactive) is an important steady state quantity during CVD diamond growth. This quantity will determine how other microscopic chemical processes affect overall macroscopic CVD properties such as growth rate and surface morphology. Carbon can only be added to the diamond via an activated surface site; therefore a larger concentration of these will lead to a higher growth rate. Also, surface radical species (discussed below) can only migrate to an adjacent active surface site. Surface ad–species migration is believed to significantly affect the surface morphology of CVD diamond.

The ratio of concentrations of active and inactive surface sites determines how many open sites are available for migration and CH_X adsorption. Under a typical CVD diamond growth regime the ratio of active to inactive surface sites

will reach an equilibrium value of approximately 10%. So this measurement is a useful benchmark to test.

CH_x(x: 0–3) addition

The other process which can occur at activated surface site is the chemisorption of another carbon containing species onto this site; thus beginning the first surface restructuring step towards growth. This is a key process which should be a primary determinant of growth rates in simulations of CVD-like conditions. The resulting growth rate can then be compared with experimental data. Therefore, it is important to correctly estimate this rate of adsorption.

The rate of chemisorption of a gas species onto the growing surface is a function of the flux of the species onto the surface and the percentage of this flux that is actually absorbed. The rate constant for CH_x adsorption was modelled using collision theory and the detailed knowledge of the concentration of the gases directly above the surface (Equation 7 and 7a). The average velocity of a molecule just above the surface is $\overline{v}$ (Equation 8), where m_{CHx} is the molecular weight of the molecule in question and T_{NS} is the temperature near the surface (~0.5 mm above the substrate) The average velocity of the molecule is multiplied by the concentration of the gas and two local factors. The *s* factor is number on the interval [0,1] which represents the steric hindrance of the molecule. The *g* factor is a similar number which represents electronic effects.

$$k_{\mathrm{CH}_x\mathrm{add}} = \frac{s_{\mathrm{CH}_x} g_{\mathrm{CH}_x} [\mathrm{CH}_x]\overline{v}}{4N_s} \tag{7}$$

$$k_{\mathrm{CH}_x\mathrm{add}} = \frac{s_{\mathrm{CH}_x} g_{\mathrm{CH}_x} [\mathrm{CH}_x]\overline{v}}{4N_s(N_N+1)} \tag{7a}$$

$$\overline{v} = \sqrt{\frac{8RT_{NS}}{\pi m_{\mathrm{CH}_x}}} \tag{7b}$$

While the steric and electronic hindrance of an adsorbing species is accounted for in our original model (Equation 7), it is the same for any configuration of adsorbing site. This approximation was tolerated in 2–dimensions as the effects of local structure were deemed to be less important.

However, it could have a more profound effect on the surface morphology of a 3–dimensional simulation. In Figure 17 the different 3-d geometries which can affect the rate of adsorption on a surface site with a particular local geometry is shown. The arrows denote an absorption reaction.

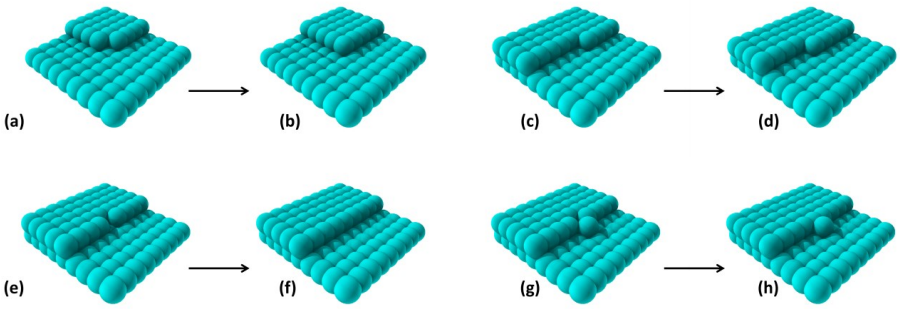

Figure 17 – A list of 3–dimensional structures affecting adsorption rates not found in the 2-d model.

The effect of local structure near an adsorption site on the rate of adsorption was modelled with a scaling factor proportional to one over the number of nearest neighbours. This can be seen in the small change to Equation 7 in Equation 7a, where *NN* is the number of nearest neighbours. This change can be physically justified by associating the $1/NN$ variable with the steric factor s_{CH_x}. As the number of nearest neighbours increases, the term S_{CH_x}/NN decreases producing a smaller rate constant making an adsorption event less likely due to increased steric hindrance of more neighbours surrounding the adsorbing site.

Ad–species activation/deactivation

Now that an ad–species has been chemisorbed onto the surface there are more processes which can now occur depending on whether or not this adsorbed species is a radical. For the purpose of our simple simulation description we will say a CH_3 species was adsorbed. This results in an inactive ad–species to which only one possible process can occur, activation. Ad–species activation (Table 1–a, iii & iv) is governed by reactions similar to those that govern surface species activation. Whilst the reactions are subtly different in reality (a surface ad-atom is

either a pendant CH_3 or a CH_2 bridge across a dimer, and a surface site is half of a reconstructed dimer), the rate constants used in our model for this reaction are the same as those used for surface species activation (Equations 1–3). The same applies to ad–species deactivation, which is governed by very similar reactions (Table 1–b, iii & iv) and the rate constants for this reaction are the same as surface species deactivation (Equations 4–5).

Once our hypothetical ad–species has been activated there are a plethora of processes that can occur. It can deactivate as described above, or it can undergo ad–species activation to become a 'doubly activated ad–species'; which represents a CH• / –C•– (bridge) species. It can then be activated again to a triply activated ad–species. The singly and doubly activated ad–species can both be activated and deactivated. The triply activated ad–species can only be deactivated and the inactive ad–species can only be activated. As well as this competition of activation and deactivation, an activated ad–species can then do many other things. It can etch away from the surface, migrate to an adjacent radical surface site, or bond to a neighbouring lattice site if available.

CH_2/CH_3 etch

The activated ad–species can then be etched from the surface. The mechanism by which this occurs is not well understood and is debated in the literature.[2,12,13] This uncertainty is the subject of enquiry later in this thesis. Whatever is the true mechanism, it is governed in this kMC model by one rate constant. In all models of etching this rate constant will almost certainly be derived from multiple complicated reaction pathways. The overall reaction should be modelled as an activated process. Previous kMC studies of CVD diamond growth, including our own, have made attempts to do this. However, none of these investigations have accurately captured the macroscopic effects of etching on the growing diamond. In order to empirically reproduce experimentally observed etching effects the previous 2–dimensional simulations of our group at Bristol used an approximation based on scaling the rate of CH_3 adsorption (Equation 3).[1,2]

Original: $$k_{etch} = N_{etch} \times f k_{CH_x add} \quad (8)$$

While this does not have an explicit theoretical basis it was used because experiments at Bristol [14] show that the rate of carbon mass loss of CVD diamond in a reactor with no CH_4 input (just H_2) is proportional to the carbon addition observed under growth conditions with CH_4 input.

The first difference examined in 3–d was the dependence of the rate of etching on the local structure. An activated ad–species can etch with a rate based on the Eyring Equation (Equation 9a). However, governed by this rate the molecule will etch with the same rate regardless of local structure. This is not a suitable approximation of the actual dependence on chemical bonding, electronic, and steric effects that will affect the etching of the ad–species. A snapshot of each different structure for which the rate is treated differently is shown in Figure 18 below. The local geometry around the molecule which represents an activated surface species should cause the rate of etching to vary. In this model, an exponential dependence on the number of nearest neighbours (NN,Equation 11) was chosen as a suitable model. Previously a linear dependence on the nearest neighbour was used (Equation 10).This puts an equal weight on the influence of each such neighbour.

Eyring: $$k_{etch} = N_{etch} \frac{k_B T_s}{h} exp\left(\frac{-\Delta G^{\ddagger}_{etch}}{RT_s}\right) \quad (9)$$

Linear: $$k_{etch} = \frac{N_{etch}}{(N_N+1)} \frac{k_B T_s}{h} exp\left(-\frac{\Delta G^{\ddagger}_{etch}}{RT_s}\right) \quad (10)$$

Exponential: $$k_{etch} = N_{etch} \frac{k_B T_s}{h} exp\left(-\frac{\Delta G^{\ddagger}_{etch} + N_N E_{wall}}{RT_s}\right) \quad (11)$$

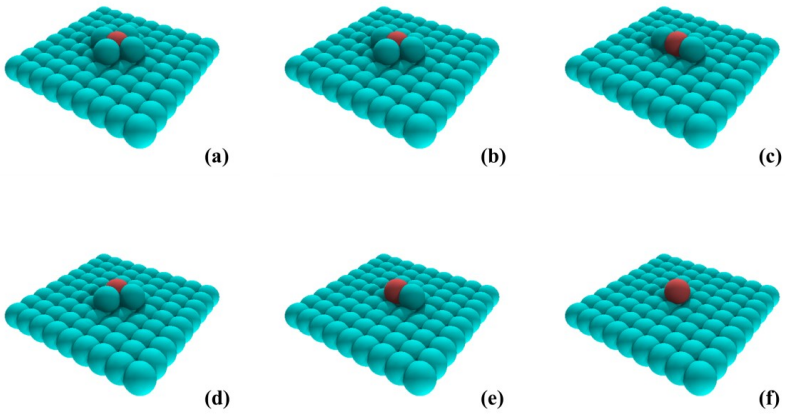

Figure 18 – 3–dimensional structures affecting etching rates. This is a visualisation of a representative (100) diamond surface in the kMC simulation program. The implementation of the program is discussed later in this chapter

Surface ad–species migration

Another process which can occur to the activated ad–species is that it can migrate to a neighbouring activated site. The migration of chemisorbed ad–species has been proposed by several researchers. [13,15,16] Unlike the migration of a physisorbed ad–species on epitaxially grown metals, the migration of a chemisorbed ad–species on a reconstructed diamond surface involves a relatively complicated reaction pathway. While not directly observed it has been suggested that this mechanism has a large influence on the surface morphology of the growing diamond. The reaction pathway has been studied by previous authors,[6,13,15,16] and in this model an Arrhenius equation (Equation 10) is used for the rate constant and the pre–exponential factor activation energy are taken from Richley et al.

$$k_{\text{migration}} = N_{\text{mig}} A_{\text{mig}} \exp(-E_{\text{a,mig}}/RT_{\text{s}}) \qquad (10)$$

The rate constant for surface migration is large, but the actual rate of migration is limited by the concentration of surface radical sites. In this model, an activated ad–species can only migrate to a neighbouring site if it is an activated surface site. For most cases, the limiting factor in the migration of a surface ad–

species is whether a neighbouring activated site is available to migrate to. This is due to the fact that surface radical migration (see two sections below) is as fast a process as ad–species migration. So even when a migration event occurs, the neighbouring active surface site left behind will more likely than not migrate away leaving the ad–species with nowhere to migrate.

Free species bonding to the lattice

If an activated surface species migrates or lands next to another species on the same level, it does not automatically bond. It has the ability to either bond with the lattice or migrate away if an active surface site is adjacent. Both of these occur with the rate constant $k_{migration}$.

β–scission

The β-scission reaction is the process (Figure 19)[17] that quickly removes two carbon chains of sp^2 hybridised carbon from the diamond surface. In this model the β-scission can occur when there are two blocks, one on top of the other, with no neigbours on either side and the top block is activated. This process occurs with a rate governed by the Eyring expression in Equation 12.

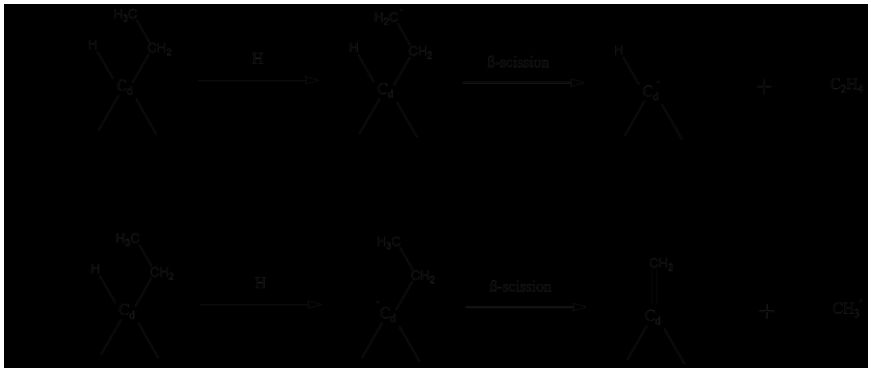

Figure 19-The β-Scission reaction removes sp^2 hybridised carbon from the surface.

$$k_\beta = N_\beta \frac{k_B T_s}{h} \exp(-1.8 \times 10^5 / R T_s) \qquad (12)$$

The Gibbs free energy of activation was estimated from unpublished electronic structure calculations of the reactions in Figure 19 done by Professor Jeremy Harvey.

Surface radical migration

There is one important kinetic process not discussed in our hypothetical simulation above that was occurring in the background but was not discussed. The migration of a radical surface site (Table 1h) is a very fast processes compared to others. The kinetic Monte Carlo method is inefficient when any one rate in the catalogue is disproportionately faster than any of the others. If surface radical migration is modelled explicitly then this process would dominate and the simulations would be too expensive to produce useful information concerning diamond growth.

In our model this problem is dealt with in a manner similar to the kinetic folding / equilibrium method used by other kMC models.[18,19] Only approximately 10% of the surface is covered with a radical site. The rate for surface radical migration is so fast compared to any other process that by the time another process does occurs the surface radical sites are essentially in a new thermal distribution. We can therefore 'fold' this process into the others so that it isn't explicitly in the model, but the necessary chemistry is preserved. This is achieved in the following manner. The surface radical migration process was turned off. However, after each process the state of the entire surface is changed such that the percentage of radical to non–radical sites remains the same, but their position on the grid is according to a random Gaussian distribution.

3.2. Computer program

The following section is about the practical implementation of the kMC model in a computer simulation written in Fortran 90. A copy of the program with all necessary input parameters is provided in the Appendix.

3.2.1. Lattice approximation

Any kMC model is going to have many approximations as a consequence of speed, efficiency, custom, and accuracy. An important step in developing a

surface growth model is the choice of whether to represent the lattice explicitly or use off-lattice models.[20] This model uses the lattice approximation. The diamond (100) surface is represented as an N×N grid where each lattice site represents a potential reaction site. All of the reactions listed in Table 2 are for the (100) surface. The 2x1:H reconstruction of the surface is not explicit in the lattice approximation, but implicitly accounted for via the reaction processes. While not as physically realistic as off lattice models it offers a reasonable compromise between computational expense and physical accuracy.

Another approximation used in these simulations is that that surface and the bulk diamond are both represented by a simple cubic geometry. This is naturally exactly the same as the unreconstructed (100) surface. The cubic structure is only naturally occurring in the bulk of the diamond. That is, if the diamond is sliced along the (100) face then a simple cubic structure is observed. However, once exposed to the atmosphere surface forms a 2x1:H reconstruction (Chapter 1). As mentioned above, this reconstruction is not explicit in this model. However, the reactions in a CVD atmosphere remove the terminal H atoms and the radical chemistry driving diamond growth reorganize the surface which effectively adds carbon to the reconstructed surface such that a new layer of (100) bulk is produced with a new surface. The simple cubic crystal structure only represents the one layer of the surface as the diamond cubic lattice consists of three repeating nonaligned cubic planes. This possibly has some implications in predicting the macroscopic properties of CVD grown diamond, but it is used in this study as an acceptable approximation. The implications and the limitations of this approximation are discussed more in the summary and further work chapter at the end of this thesis.

3.2.2. Boundary conditions

As this model involves the migration of species on a finite grid it was necessary to implement periodic boundary conditions. This was a relatively simple procedure that will be demonstrated by an $n \times n$ grid is shown in Figure 20. Looking at one square on the figure migration can only occur in four

directions ‘up’, ‘down’, ‘left’, and ‘right’ as viewed from above. If the simulation is at point (X_n, Y_n) on the grid and it were to migrate up the species in question would migrate to (X_n, Y_0), and if it were to migrate right it would end up on point (X_0, Y_n). If the simulation starts at point (X_0, Y_0) and migrate down the it will end up at (X_0, Y_n) and if it migrates left it will be at (X_n, Y_0).

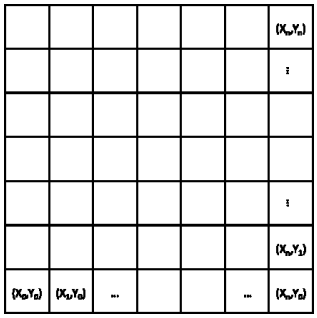

Figure 20-An n×n grid of squares to demonstrate periodic boundary conditions

3.2.3. Initial conditions

The rate constants in the kinetic model are determined by three main properties which are derived from other sources. These are the concentration of gas species above the surface, the energetics in the rate constant (normally the activation energy E_a and a pre–exponential factor A), and the temperature of the gas near the surface and that of the surface itself. These are the initial conditions in the kMC model that determine the resulting simulation of growth. There are two input files that can be changed to perform various experiments/simulations.

The file *input.txt* contains the important model parameters that are changed according to which CVD conditions are being simulated. $\mathbf{T_{ns}}$ is the temperature of the gas near the surface which affects the pre–exponential factors of some of the rate constants. This is usually hotter than the temperature of the substrate, $\boldsymbol{T_s}$. The concentrations of gases above the surface are taken from the data calculated from the Bristol-Moscow model discussed in the introduction. These are the concentrations of **H**, $\mathbf{H_2}$, $\mathbf{CH_3}$, $\mathbf{CH_2}$, **CH**, and **C**. Included with the concentration of each species are two parameters describing the hindrance of the molecule due

to steric, ***s***, and electronic effects, ***g***. These three parameters are used to estimate the adsorption rate of each species shown in Equations 7, 7a, and 7b x previously. Finally, there is the total time of the simulation and the **N×N** size of the surface to be simulated. There are other housekeeping and testing parameters which are not a part of the physical model, but useful none the less. A sample input.txt can be found in Appendix A.

The file *energy.txt* contains the pre–exponential factor, **A**, and the energy of activation, $\mathbf{E_a}$, for the rate constants used in the reactions listed in Table 2. These are not dependent on the type of CVD diamond growth conditions. They are included in a separate file for model validation and sensitivity testing. This topic will be addressed in the 2nd half of this chapter. As with input.txt, a sample file of energy.txt is provided in appendix A as well.

3.2.4. Output

In this section the output of the kMC program is discussed. Various features of this output will be presented in subsequent results chapters for individual simulations of different growth conditions. The overall form of these metrics is presented here as a reference to frame the presentation of subsequent results from simulations.

General dynamic output

There are three main output classes that can be monitored for the whole simulation time; growth rate, surface roughness, and the frequency that each process occurs. Each of these three categories gives an insight into the simulated diamond and can be used as a cross check to the program all without the need for the more costly post processing visualisation process. This means that many simulations can be run and bulk results from these experiments can be compiled together into a bigger picture.

While discussing the output of the program below, all of the results come from one simulation. A set of initial conditions was used similar to that found

experimentally in a microcrystalline diamond (MCD) growth environment. This type of diamond has an average crystallite size on the micrometres. The input parameters are given in Table 3 below:

Table 3–Parameter set for microcrystalline (MCD) diamond growth simulation

T_s	/K	1173
T_{ns}	/K	1267
[H]	/ cm^{-3}	1.85×10^{14}
[H_2]	/ cm^{-3}	1.52×10^{17}
[CH_3]	/ cm^{-3}	1.46×10^{13}
[CH_2]	/ cm^{-3}	3.66×10^{8}
[CH]	/ cm^{-3}	2.74×10^{8}
[C]	/ cm^{-3}	3.37×10^{9}
Grid size	/ $block^2$	25×25
Total time	/ s	150

Growth Rate

The measurement of the growth rate as a function of time over the course of the simulation is recorded throughout. It is calculated as a function of average height over the total simulation time (Equation 13) where the average height of the simulation surface, $\overline{h}$, is scaled by the separation distance between two layers of the (100) diamond surface, $C - C_{(100)} = 0.892$Å.

$$\frac{C-C_{(100)}\overline{h}}{t_{total}} \tag{13}$$

The inclusion of this measure gives the user a fast check that the simulation is statistically equilibrated in the sense that the value of the rates reaches a steady state average with little noise. The growth rate should be relatively constant throughout the simulation. There is a period of instability at the beginning before the kMC simulation has reached the characteristic time at which each process is in a steady state. This initial instability with subsequent stability of the growth rate can be seen in Figure 21 below. This shows that the growth rate reaches a steady state value rapidly as the simulation becomes statistically equilibrated.

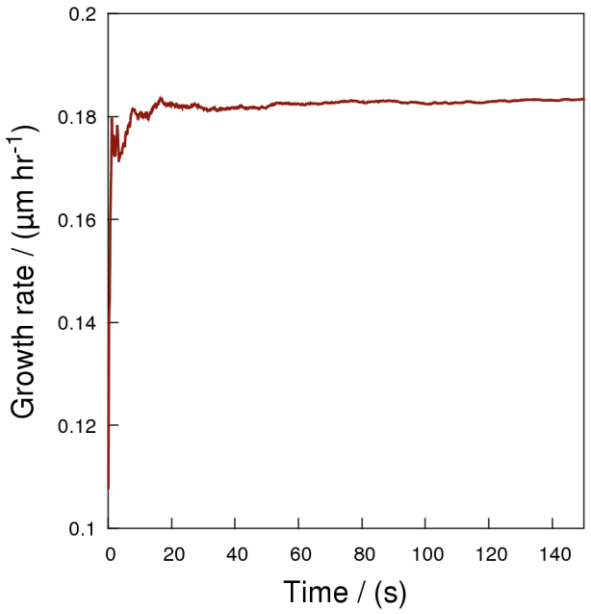

Figure 21–Surface growth verses simulation time for a 150s of a simulation of MCD diamond growth on a 25×25 grid.

This figure shows the growth rate changing rapidly in the beginning as the system 'equilibrates'. However it quickly reaches a certain value with a lessening amount of statistical noise after about 30s of simulation time. The noise is almost completely gone after 60s. The average growth rate taken from 40s on is 0.182729 µm h^{-1} with a standard deviation of 0.000424 µm h^{-1}. The small amount of standard deviation from the mean for 110s of simulation shows that the simulation is stable and can produce a value for the growth rate. This value will be used with other output parameters in subsequent chapters to test the model against the experimental results of others.

Surface roughness

The next experimental measurement that the kMC results can be compared with is surface roughness. The surface roughness is an average of the height profile usually taken by AFM measurement. This gives an approximate gauge of quality and type of surface morphology for the diamond measured. In these kMC simulations the root mean square deviation (Equation 14) is used as an

analogue for surface roughness and is equivalent to monolayer coverage. The closer this value is to zero the more likely it is that the surface has a smooth mono layer.

$$\sqrt{\frac{\sum_{i=1}^{n}(h_i-\bar{h})^2}{n}} \tag{14}$$

This roughness can be measured as a function of time, but it is customary and more informative to plot it as a function of the average surface height measured in layers as the simulation proceeds. An example from the standard calculation from this section is show in Figure 22. From this it is noticeable that the roughness stays below one over the course of the simulation. This shows that the simulated diamond is growing in a layer by layer fashion, i.e. the 'holes' in the previous layer are filled before another layer is nucleated. If it were perfect layer by layer growth the function would be sinusoidal from 0 to 1 at every integer height. The surface roughness measurement is used throughout this study as a first analysis of the surface morphology of different CVD growth regimes.

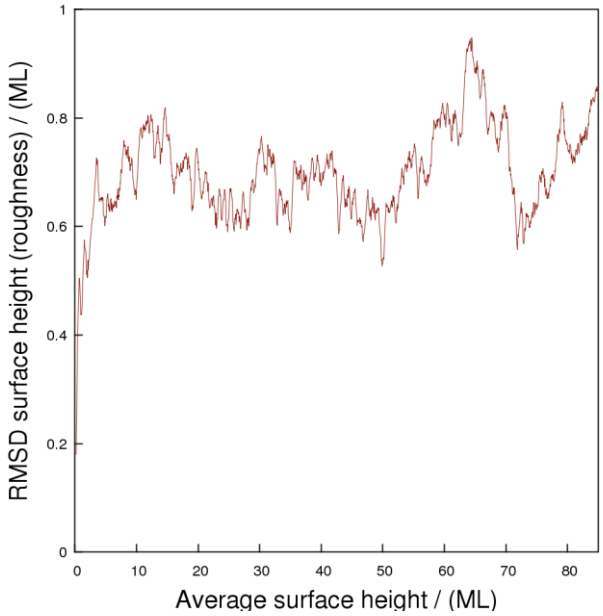

Figure 22–Surface roughness (RMSD of the surface height) as a function of the average surface height in ML (monolayers) for the standard conditions from Table 3.

Reaction rates

The last numerical output of the program to be discussed is the rate of each reaction (Table 2) during a simulation. At each Monte Carlo step a process is executed, and this is recorded as a frequency. This, with the Monte Carlo time step, can provide a way to calculate the rate of each overall reaction at each time step. These rates should essentially be in a steady state during the CVD process. This along with frequency counting can provide a 'reality' check when developing the code, such as adding a new reaction process. This facility is also useful in testing which processes are dominant / important and which are not for various simulated growth conditions. In Table 4 below, the average rates of reaction are listed for the same simulation used in the previous two sub sections.

Table 4– A list of the average rates for each process during a kMC simulation with MCD conditions for 150s. The rates are approximately in a steady state after the kMC simulation has thermalized, so an average of each taken after this time is the rate of each reaction for the simulation.

Reaction	Rate / s^{-1}
CH_3 adsorption	$3.90\times10^{2} \pm 7.4\times10^{-1}$
CH_3/CH_2 etching	$3.25\times10^{1} \pm 4.4\times10^{-1}$
Surface activation	$6.23\times10^{5} \pm 6.8\times10^{1}$
Surface deactivation	$6.23\times10^{5} \pm 6.8\times10^{1}$
Ad–species activation	$1.07\times10^{3} \pm 1.1\times10^{1}$
Ad–species deactivation	$7.72\times10^{2} \pm 1.0\times10^{1}$
Migration	$1.38\times10^{3} \pm 1.8\times10^{1}$
Beta–scission	$1.01\times10^{0} \pm 5.5\times10^{-2}$
Double activation	$1.04\times10^{2} \pm 1.7\times10^{0}$
Double deactivation	$1.00\times10^{2} \pm 1.8\times10^{0}$
Triple activation	$1.31\times10^{1} \pm 2.0\times10^{-1}$
Triple deactivation	$1.30\times10^{1} \pm 2.0\times10^{-1}$
CH_2 adsorption	$2.24\times10^{-2} \pm 5.7\times10^{-3}$
CH adsorption	$2.66\times10^{-2} \pm 7.5\times10^{-3}$
C adsorption	$5.41\times10^{-1} \pm 5.0\times10^{-2}$

It is obvious from Table 4 that surface activation and deactivation dominate the simulation of MCD diamond, as is generally true of all growth conditions, by two orders of magnitude relative to the next fastest process.

Visualisation

While many important measures were quantitatively taken from the simulation, it was helpful for qualitative understanding to visualise surface. The visualisation routine was a post processing python script that counted all of the surface restructuring kMC steps (adsorption, etching, migration, and beta-scission) and output an xyz trajectory of these steps. The open source visualisation software OVITO [21] was used to produce movies and render still pictures like the ones in Figure 23.

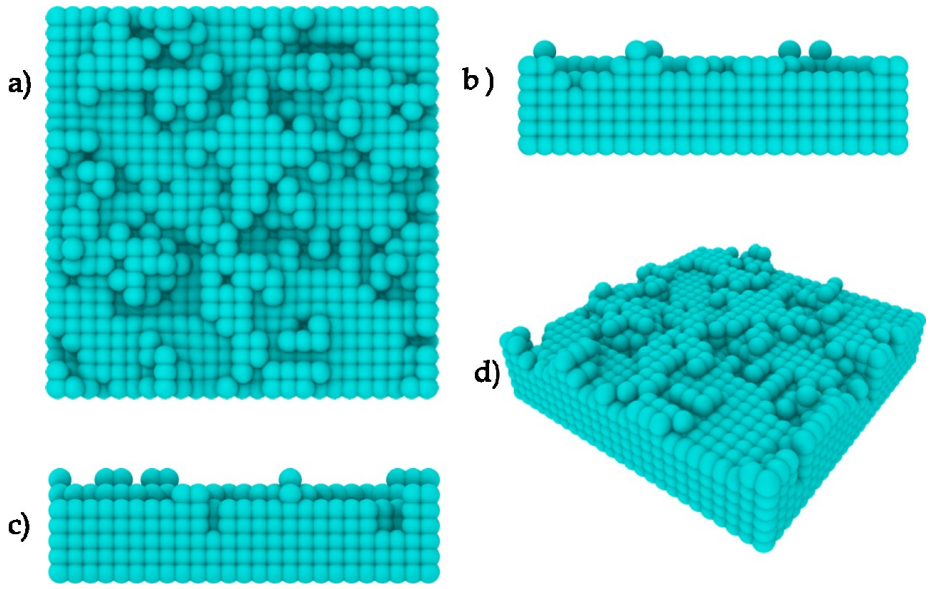

Figure 23–four views of a 25x25 MCD simulations, a) x–y plane b) x–z plane c) y–z plane d) 3–dimensional view

3.3. Sensitivity testing

In this section the testing of the kMC program for the model described above is discussed. This new program was tested in two ways. The first is also a direct comparison with the older 1–dimensional model developed previously,[1,2] and the second was a sensitivity test. The first test was necessary, as the implementation of the kMC algorithm was completely different new from the old. It was essential to start from the same place as the previously published work in order to have confidence in the new program. This would then allow for a greater confidence when adding new processes and species to the model.

After this, a detailed systematic sensitivity analysis of the input parameters for the kMC program was carried out. Unlike the previous program, the structure of the new program allowed this to be done in a computationally feasible time frame. The parameters for the rate constants and gas concentrations discussed in sections 3.1.2 and Chapter 1 were obtained from experiments and theoretical calculations each with its own set of uncertainties. These can then

compound in unforeseen ways when combined together in the kMC model. The purpose of this analysis was to judge the sensitivity of output for the kMC program to changes in the input parameters. This was then compared with the known uncertainties in the parameters in order to estimate the effect that these would have on the output of our simulations. This analysis also allowed us to study how the individual kinetic processes (Table 2) interact with each other in the dynamics of the diamond growth system. That is to say, we know how these individual processes behave in isolation but not when coupled with competing processes.

In the following set of calculations the initial parameters simulating both MCD and NCD (micro and nanocrystalline diamond) growth regime (Table 3 and Table 5) were used. Whilst MCD diamond growth represents the most well-known and one of the best possible CVD diamond growth conditions, it requires a significant amount of computational resources in our model. In this section a large number of statistically equilibrated calculations were run, each with one minor variation. This systematic exploration of the parameter space of the kMC model was computationally expensive. Simulations carried with the NCD growth conditions from Table 5 below are statistically equilibrated much quicker than MCD growth and the simulated chemistry is such that it still represents CVD diamond growth well. Therefore MCD and NCD growth conditions were used to explore the parameter space of the model more efficiently.

Table 5 - Input parameters for nanocrystilline diamond (NCD) growth conditions.

T_s	/K	1173
T_{ns}	/K	1267
[H]	/ cm^{-3}	1.52×10^{14}
[H_2]	/ cm^{-3}	1.51×10^{17}
[CH_3]	/ cm^{-3}	5.68×10^{13}
[CH_2]	/ cm^{-3}	8.12×10^{10}
[CH]	/ cm^{-3}	6.53×10^{8}
[C]	/ cm^{-3}	5.45×10^{9}

3.3.1. Surface size

The largest influence on CPU time for a simulation is the size of the $N \times N$ grid which represents the surface. The total simulation time increases with N by approximately $O(N^4)$(Table 6). The total number of Monte Carlo simulation steps will scale as N^2 for a given total simulated time. However, choosing which process to carry out at each simulation step will take longer as the surface grows. For an $N \times N$ surface the number of possible processes that could occur will scale approximately as N^2. Which process to carry out is determined at each simulation step, therefore a total scaling of $O(N^4)$ agrees with this justification. The extent to which the stability of the results, reaching a steady state, depends on the size of the surface grid is shown here. Growth conditions known to produce microcrystalline (MCD) diamond experimentally were used as the simulation time was shorter than single crystal diamond yet produced results which still provided an accurate model of growth. The initial conditions used for these tests are shown in Table 3 above.

Table 6 - Total wall time for each $N_i \times N_i$ grid simulation where $N_i = 5i$ for i = 1-10.

N	N×N	Total wall time / s
5	2	21
10	100	228
15	225	1012
20	400	2755
25	625	6642
30	900	14087
35	1225	25480
40	1600	42973
45	2025	67658
50	2500	103996

Ten simulations, each with a total simulated time of 50 s, were performed; the only change for each being the grid size, an $N_i \times N_i$ grid where $N_i = 5i$ for i = 1-10. It was expected that the quantities measured in the simulations would approach a converged value. The purpose of these tests was to give an insight into which size grid would be the most efficient for running other, longer,

experiments, that is, which grid size will give a reasonable accuracy whilst not being too computationally expensive.

As expected, the noise in the dynamic outputs was large at very small grid sizes. This noise decreases dramatically as the grid size is increased. As well as this, the measured properties (growth rate, surface roughness, and process rates) approach a steady state value much more quickly as the grid size increases. In Figure 24 below the dynamic output of growth rate over a 50 s simulations is shown for three simulations (for clarity in the picture) run with a 10×10, 25×25, and a 50×50 grid.

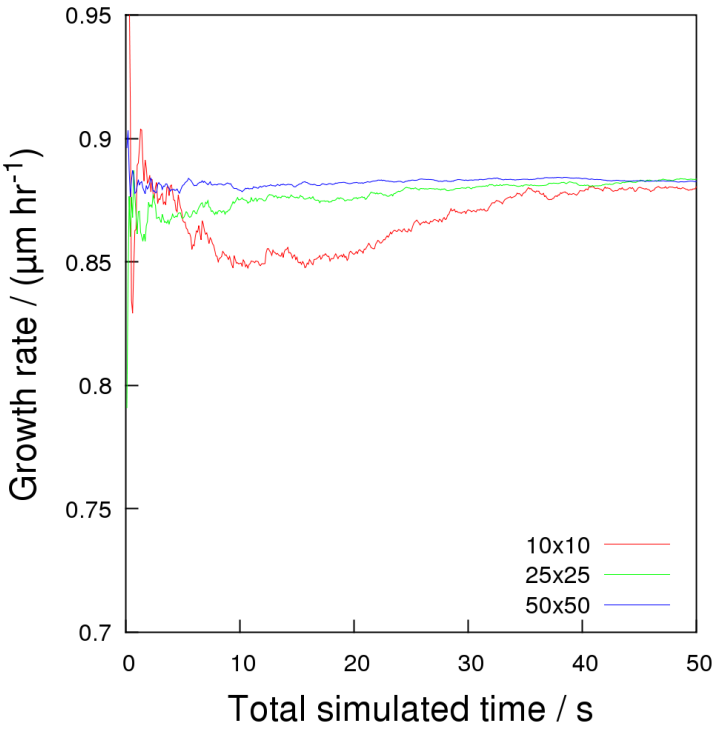

Figure 24-Growth rate verses total simulated time for simulations with a 10×10, 25×25, and 50×50 grid using MCD growth parameters

The results from the 10×10 grid simulation show that the growth rate does not reach a steady state value until around 40 s simulation time, and there are still small fluctuations in the value. The growth rates from the other two

simulations shown in the figure above approach a steady state much sooner and both become more stable as well. The results improve as the grid size increases.

The results of the RMSD surface roughness for the same three simulations are shown below in Figure 25. The surface roughness for MCD growth is expected to approach a steady state value. The statistical noise around this value will be much stronger than that in the growth rate due to the effects from local structure in single calculations such as mound sharpening and flattening around a long term average. The same patterns seen in Figure 24 are exhibited below in the surface roughness results. The 10×10 grid simulations show a large variation in roughness. A quasi-layer-by-layer pattern of growth can clearly be seen, but the value is too noisy to be trusted as the variation in the roughness after the simulation reaches a steady state is too large. The 25×25 grid shows fewer fluctuations than the smaller grid, but local structure effects can be seen around an average height of 40 ML and 120 ML. These local structure affect are averaged out as the grid becomes larger. The 50×50 grid simulation yields a much more continuous curve reaching a limiting value of approximately 1 ML.

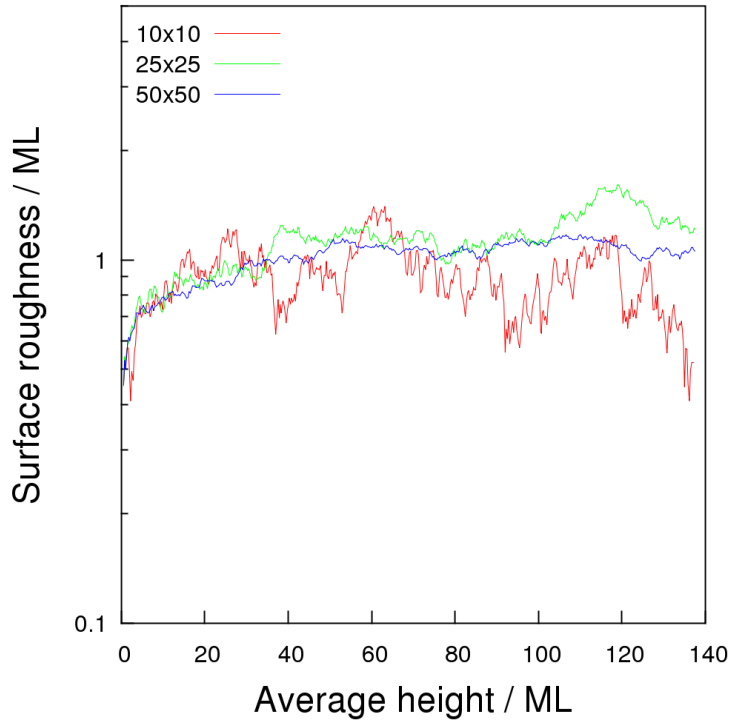

Figure 25-Surface roughness verses the averave simulated height of the surface for simulations with a 10×10, 25×25, and 50×50 grid using MCD growth parameters

While it is apparent from the results presented above that the 50×50 grid produced the most converged results, the simulation took approximately 28 hrs of wall time to complete (Table 6). This is not computationally too expensive by itself, but when exploring vast portions of the parameter space of the program (100s of simulations) this becomes costly. This is especially true when the simulations on a 25×25 produce adequate results with only a wall time of 1.8 hrs. Thus the 25x25 grid was chosen to produce quality results for the exploration of parameter space while doing so in a reasonable time frame.

3.3.2. Simulated time

After considering surface size, the next logical step was to look at the temporal convergence of the kMC program. The same gas parameters for MCD

(Table 3) growth were used in long simulation with a total simulated time of 150 s on a 25x25 grid.

Results for the growth rate versus simulated time for this simulation can be found below in Figure 26. There are two sets of data representing the growth rate on this figure. The continuous curve in green is simply the growth rate as a function of time from 0 to 150 s. The growth rate reaches a steady state value of 0.88 μm hr^{-1} by approximately 80 s. However, the measure reaches steady state (to one significant figure) before 10 s of simulated time. The second measure is an average of the second half of the growth rate function taken from the time where the point is shown on the graph. So, for example, the point at 80 s which is 0.8839±0.0012 μm hr^{-1} is an average of the growth rate from 40 s to 80 s. The reasoning behind taking the average of the later half is that the variation in the growth rate decreases as simulated time increases and averaging over the entire time period at each point chosen would include too much noise from early in the simulation. The temporal convergence is most obvious in this curve (the blue squares in Figure 26). The first average at 10 s is 0.871±0.002 μm hr^{-1} value. The average then approaches a converged value of 0.884 by 80 s with a decreasing standard deviation up to the final average taken at 150 s.

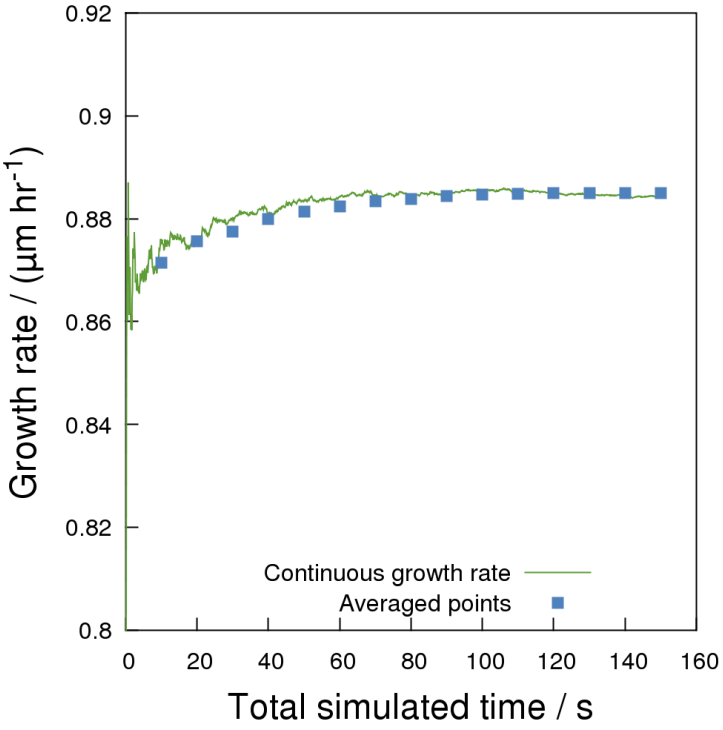

Figure 26–Growth rate as a function of time for a 150 s simulation with MCD growth conditions and a 25x25 grid.

The results for the surface roughness over the simulated time of 150 s are shown below in Figure 27. The curve is jagged and peaked, but it does tend to centre on an average value of 1.086 / ML which is similar to the larger grid sizes discussed in the previous section. These peaks are due to local structure affects that are averaged out on larger grid. They represent a multi-layered 'nucleation' site that offers more places to which a migrating or adsorbing carbon can add than on a smoother surface. These nucleation points are eventually smoothed out in this growth regime (MCD) resulting in a decrease in surface roughness, hence the troughs in Figure 27.

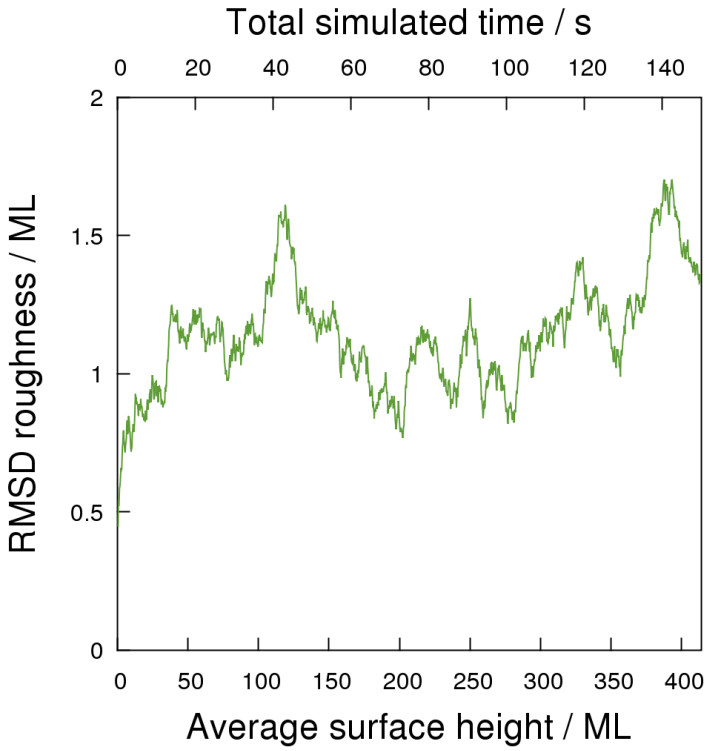

Figure 27- Root-mean-square devation (RMSD) surface roughness as a function of simulated time and average surface height for a 150 s simulation under MCD growth conditionsand a 25x25 grid.

For a simulation with a 25x25 grid the temporal convergence to a steady state as shown in the data presented above is relatively quick. A value of 0.861 μm hr^{-1} is found at a simulated time of 1.0 s, which is within 3% of the long-time average taken at 150 (0.885 μm hr^{-1}). However, at 1.0 s the fluctuations around the mean are 20 times as large as those at 50 s (0.0021 and 0.00043 μm hr^{-1} respectively). The temporal convergence of the surface roughness is harder to define. The roughness increases from 0 to 50 s and then starts to hover around and 1.2 ML. It then oscillates for the rest of the simulation as shown above. The roughness first approaches the final average value for the first time, then this would be at around 50 s simulated time. As can be seen from Figure 26, the growth rate is already well on its way to convergence. So it appears that it takes

longer for the surface roughness to reach a meaningful steady state value in the simulation than the growth rates.

3.3.3. Gas concentrations

The concentration of H, H_2, and CH_3 was varied between 1% and 199% of the standard concentrations for NCD growth conditions given in Table 2 Table 5 shown above. In this study it is assumed that the concentrations obtained for the accurate modelling of gas phase chemistry done previously by our group are accurate. However, the data taken as the concentrations near the surface are an extrapolation of a model, and therefore could be subject to unforeseen inaccuracies. Therefore it is important to know how these concentrations of gases at the surface affect the outcome of the kMC simulation. The sensitivity of output to these tests will enable us to gauge the validity of simulation output when compared with experimental data later. By having confidence in the accuracy of the input parameters we have a better assurance that our kinetic model is accurate if our simulation results reproduce experimental results

[H]

The concentration of H· above the surface during CVD diamond growth is important for many reasons. These were discussed in Chapter 1, so it is sufficient to say here that the excess energy from these radicals drive the majority of the chemistry involved in CVD diamond growth. It will be shown here that the sensitivity of the kMC model to changes in [H] is significant.

In Figure 28, the growth rates produced from the variation of the concentration of H above the surface from 1.52×10^{12} cm^{-3} to 3.02×10^{14} cm^{-3} (1% to 199% of the value of [H] given in Table 5. The growth rate increases quickly at first and then approaches a limiting value smoothly. This is due to the increase in active sites as [H] increases. More H· near the surface leads to more abstraction reactions of H bonded to surface species. This means that the ratio of active to non-active surface sites increases enabling a corresponding increase in carbon adsorption. However, this increase in growth rate begins to slow as the

concentration of active surface sites increases. This becomes the limiting factor in increasing growth rates.

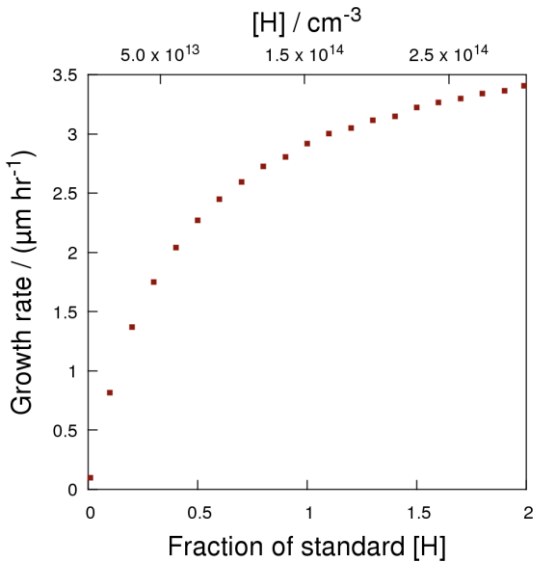

Figure 28–Growth rate over the varied fraction of the standard [H] in NCD growth conditions.

As the surface is covered with more ad-species these also become active more frequently as [H·] increases. As a larger proportion of active surface sites become available the chance of an active ad-species having an active surface site as a neighbour is greatly increased, thus increasing the likelihood of said species migrating. It was found that the rate of active ad-species migration increased linearly with increase in [H·]. This suggests that once the surface is saturated with active surface sites and ad-species the rate of migration continues to increase with [H·]. The increase in ad-species activation does not lead to a noticeable increase in the rate of etching. It only increases in line with the growth rate as the rate of migration is very large compare to that of etching.

The increase in the rate of migration coupled with no increase in etching could have an effect on the surface morphology of the simulated diamond. An average for each simulation of the last 80% of the RMSD surface roughness measure was taken. No systematic trend was seen in these values and it appears

that the [H] concentration does not greatly affect the surface morphology in our model. The average and one standard deviation of these subsequent 21 values was 2.385 ± 0.358 / ML

[H_2]

The concentration of H_2 above the surface is much higher than that of H•; approximately 10^3 times larger in standard NCD growth conditions as shown in Table 5 . Although it is much less reactive than H· a proportionally larger change in concentration should affect the outputs. The standard concentration for H_2 from Table 5 is 1.51×10^{17} cm^{-3}. As with the set of simulations for [H] above the concentration of this gas was varied from 1% to 199% of the standard concentrations; this was a range from 1.51×10^{15} cm^{-3} to 3.00×10^{17} cm^{-3}.

The results for the growth rate over this variation are shown below in Figure 29. Here an almost linear decrease is observed. Over the entire range the gas concentration variation the absolute magnitude of the change is growth rate was only 1.6 μm hr^{-1}. This is a smaller change in growth rates than for [H] over the same magnitude of gas variation.

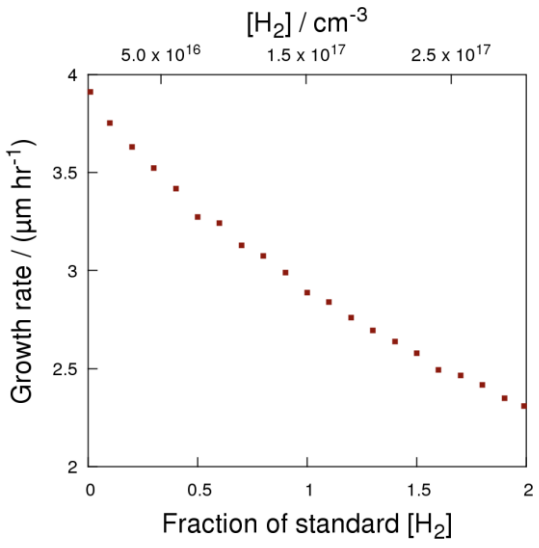

Figure 29-Growth rate over the varied fraction of the standard [H_2] in NCD growth conditions.

The decrease in growth rate is caused by an increase in the rate of the surface site deactivation reaction relative to surface activation. This occurs due to the dependence of $k_{deactivate}$ on $[H_2]$, while $k_{activate}$ lacks this dependency.

The surface roughness also shows a small variation unlike the results for [H·]. The average surface roughness with error bars of 1 standard deviation over the variation of H_2 is shown below in Figure 30. The measurement of surface roughness can sometimes be affected by local structure effects, so there are bound to be outliers in any set of simulations. However, it is clear from the figure below that there is a slight linear dependence in the surface roughness as $[H_2]$ increases. A change of approximately 1 ML of surface roughness is observed from the lower to higher concentrations. One ML is larger than one standard deviation of all the simulated measured values.

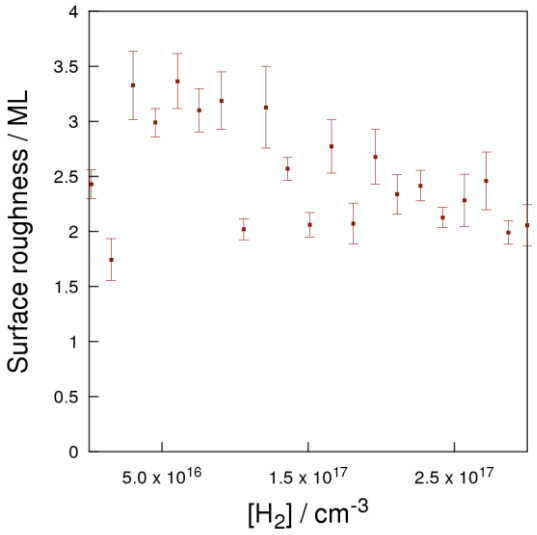

Figure 30-Average surface roughness over the varied fraction of the standard $[H_2]$ in NCD growth conditions.

The kMC program is likely not sensitive enough to changes in $[H_2]$ for any error in its estimation to affect the outcome. The above results do show that the program does model the microscopic physics as intended with regard to $k_{deactivate}$'s dependence on $[H_2]$.

[CH_3]

As shown previously in Chapter 1 the methyl radical is considered to be the most important molecular species in terms of carbon addition to the growing diamond.[17,22] Therefore the concentration of CH_3 above the growing diamond surface is a key parameter to determine in order to have an accurate model of diamond growth. Here, as for H_2 and H, we test the sensitivity of the kMC output to variations in [CH_3].

The results of this test for diamond growth rates can be seen in Figure 31 below. The first strikingly obvious feature of this plot is the direct linear dependence of the growth rate of the resulting diamond with the variation in [CH_3]. The magnitude of this change is also greater than with the same variations in the relative magnitudes of [H] and [H_2]. This result shows that [CH_3] is an important parameter to accurately model in order to obtain results comparable with experiment.

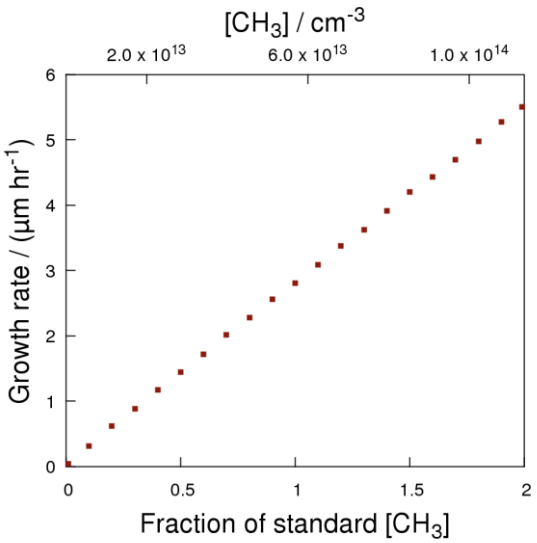

Figure 31-Growth rate over the varied fraction of the standard [CH_3] in NCD growth conditions.

The surface roughness is significantly affected by the concentration of CH_3 due to the considerably increased growth rates which occur without a

corresponding increase in surface migration. The added number of surface ad-species per unit time does increase the rate of migration as [CH_3] increases, but not fast enough to compensate for the increased re-nucleation of a new islands and layers. The results for surface roughness over the tested range of [CH_3] are shown below in Figure 32. The average RMSD of the surface height increases linearly from 1 to 100% fraction of the standard concentration. It then continues to increase, but with a less steep gradient. The results have the outliers typical of the local structure effects mentioned before. However, there is a clear correlation between [CH_3] and the surface morphology.

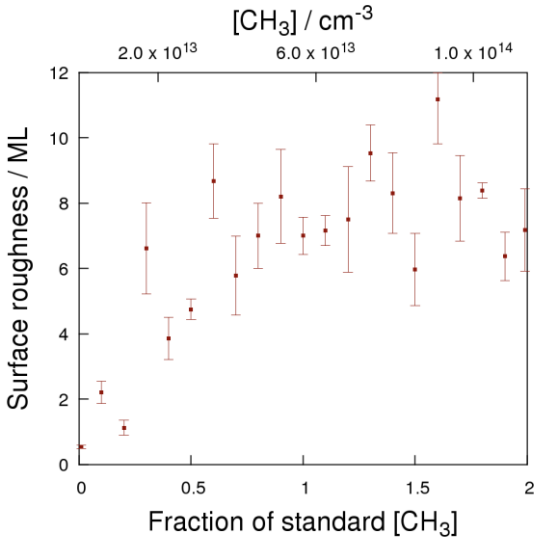

Figure 32-Average surface roughness over the varied fraction of the standard [H_2] in NCD growth conditions.

3.3.4. Substrate temperature

The substrate temperature (*Ts*) is one of the more important experimental parameters as it can be controlled and observed relatively easily. It governs the growth rate and morphology of the resultant diamond almost as much as the gas mixtures.[23–25] Experimentally the variation of the growth rate with Ts passes through a maximum. To date, only one other kMC model has shown a peak in growth rates versus substrate temperature.[26] This was for growth on the (111)

surface, which is no longer seen as a growth facet as important as the (100) surface. Previous models of CVD diamond growth did not predict this peak for growth on the (100) surface even though this is now thought to be the dominant growth facet. Neither did they show an increase in growth rate with temperature until the development of the Netto–Frenklach model.[13] However, there has been no theoretical explanation of this behaviour, only speculation. Our model reproduces this peak seen in Figure 33, which shows growth rate as a function of substrate temperature for several simulations and experiments. The data from experiment [23,24] shows a peak just above 900 °C and our model peaks just below 1000 °C.

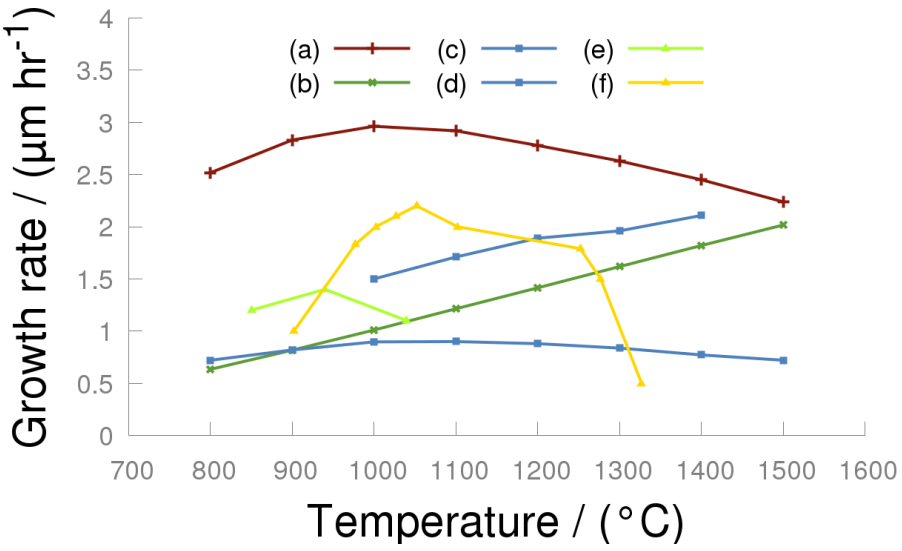

Figure 33– A comparison of CVD diamond growth over a range of substrate temperatures.

(a) Our model with NCD growth parameters
(b) Our model with MCD growth parameters
(c) Our model with Frenklach H rate constants
(d) Netto and Frenklach, Diamond Relat. Mater. 14, 1630 (2005)
(e) Kweon, Lee, and Kim, J. Appl. Phys. 69, 8329 (1991)
(f) Kondoh, Ohta, Mitomo, and Ohtsuka, Appl. Phys. Lett. 59, 488(1991).

The Netto–Frenklach model predicts a linear increase in growth rate at all substrate temperatures. There is no maximum. The kinetic processes and their associated rate constants that were included in the Netto–Frenklach model were

compared with our own current model to determine which processes were responsible for the difference. A difference in rate constants for the 'surface deactivation' processes was singled out. This process was modelled by Netto using only the reaction of an H· radical adsorption to the surface with a non–Arrhenius (no temperature dependence) rate. The addition of H from an H_2 abstraction reaction with a surface radical species and temperature dependence for both was not included in the Netto model but was in ours.

The rate constant for surface deactivation in our model was changed to equal the Frenklach model. Another series of simulations varying substrate temperature using the new rate constant were performed and the results were then compared (Figure 33). We reproduced the results by this simple change, thus suggesting that it is the missing H_2 reaction that we have included in our model and the temperature dependence that of the hydrogen reactions that help determine this peak in growth rate. As the temperature of the substrate increase, these reactions occur more frequently. At first this allows more adsorption to occur, but after *T*s approaches a certain point there is a decrease in the available number of active surface sites available for C_XH_Y adsorption.

3.3.5. Gas temperature

The gas temperature near the surface, T_{ns}, affects the mean collision frequency of gas phase species with the surface. This effect was modelled in our kinetic rate constant equations by including a linear dependence on T_{ns} in the pre-exponential factor.

In microwave CVD reactors, the temperature at the centre of the gas T_{gas} is measured reasonably accurately in experiments by laser spectroscopy equating T_{gas} with the average rotational temperature of the gas.[27] The temperature decreases the further away the gas is from the centre. A computational continuum model of gas flow and thermal diffusion of a MW CVD reactor was created as part of a collaboration between the diamond group in Bristol and Y.A.

Mankelevich at Moscow State University.[28] The gas temperature near the surface was taken from this model which was discussed previously in Chapter 1.

As the value for T_{ns} in Table 5 is 1267 K a set of simulations was run with T_{ns} between 267 and 2267 K (±1000 K) at 100 K intervals. The results for the growth rate and surface roughness are shown in Figure 34 below. The base conditions for these simulations were the NCD parameters from Table 5 with a 25×25 grid and a total simulated time of 150s for each. As T_{ns} increases the flux of CH_X (Equation 7) species increases, as well as the reactions that govern the rate of activation and deactivation (Equations 2, 5, and 6). The absolute magnitude of change in the growth rate over the 2000 K variation is approximately 3 μm hr^{-1}; the top graph in the figure below shows this increase as a function of T_{ns}. The increase is slightly non-linear. This is probably due to the fact that equation 3 is not dependent on T_{ns}. While the flux of carbon increases linearly with temperature, the ratio of activated surfaces sites does not. This is merely an artefact of how we chose to represent $k_{a\text{-}i}$, $k_{a\text{-}ii}$, $k_{b\text{-}i}$, and $k_{b\text{-}ii}$ which does not affect the outcome too much.

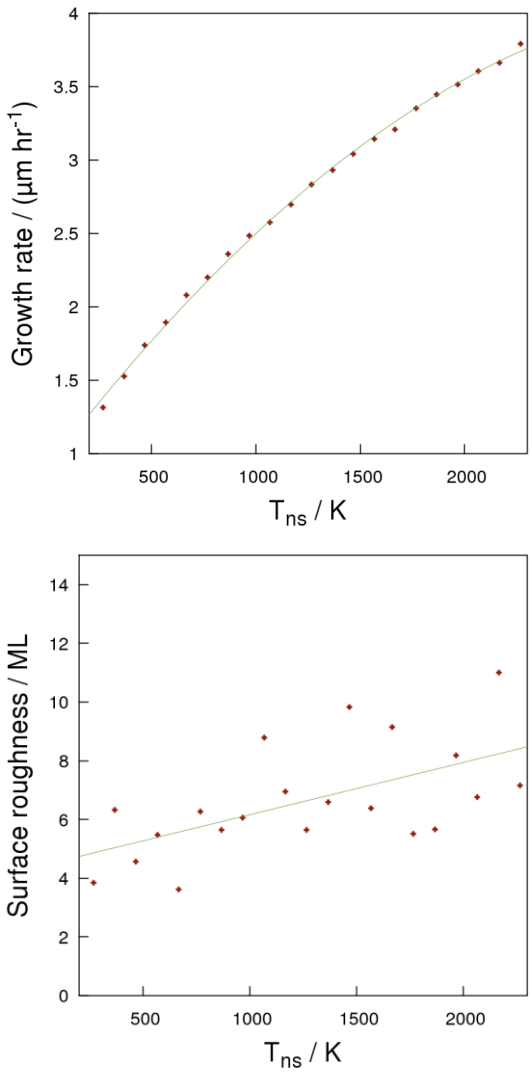

Figure 34-Variation of T_{ns} over 2000 K from 267 K to 2267. The top plot shows the growth rate (in µm hr^{-1}) and the second shows surface roughness (in monolayers) both as a function of T_{ns}.

The bottom graph in Figure 34 shows the difference in the average surface roughness over the variation of T_{ns}. Here the surface morphology shows a patterned dependence on the varied parameter, unlike some of the tests above where the growth rate varied and the surface morphology showed no change within the statistical limits of the measurement. It can be seen from the error bars

in the data points and the fitted line that there is a distinct linear dependence between average surface roughness and T_{ns}. While the data is noisy the surface roughness does appear to have a positive correlation with an increase in T_{ns}.

3.3.6. Reaction rate constants

$k_{activate}$

The rate constant for the activation of inactive surface sites and ad species is governed by Equation (1) shown in section 3.1.2. This rate is mainly determined by the concentration of radical H· in the gas phase and the rate at which it is adsorbed to the surface, k_{a-i} (Equation (2)). The sensitivity of the kMC model to the accuracy of the [H·] was reported in section 3.3.3 as its variation affects more than one process in the model. Here we test the sensitivity of output to the activation energy in the rate constant k_{a-i}, which was determined experimentally, as it only affects the rate of activation (surface and ad-species - $k_{activate}$). This is then combined with the gas concentration data to develop a coherent picture of how the two affect the rate of activation in the kMC program.

In order to test the sensitivity of the program to the error in the activation energy obtained for reaction k_{a-i} this energy was varied by ±10 kcal mol^{-1}. Twenty–one simulations where carried out with identical input parameters, the ones shown in Table 5. Each simulation differed in the energy of activation ΔE_n by 1 kcal mol^{-1} such that $\Delta E_n = \Delta E_0 + \delta\Delta E$, where $\delta\Delta E$ is an integer value between –10 and 10 kcal mol^{-1}.

The results for both growth rates and surface roughness as a function of activation energies are shown as a function of $k_{activate}$ in Figure 35 below. The values of growth rate are represented by the red squares (with an interpolating line) and vary from 0.1 to 25.6 μm hr^{-1}. The growth rates increase rapidly as the rate of $k_{activate}$ increases, but the rate of change in the growth rate levels off as activation exponentially increases. This is due to the fact that more surface sites are available as "dangling bonds" to which a gas phase molecule can adsorb.

Therefore more fundamental carbon growth steps can occur on the surface relative to other processes.

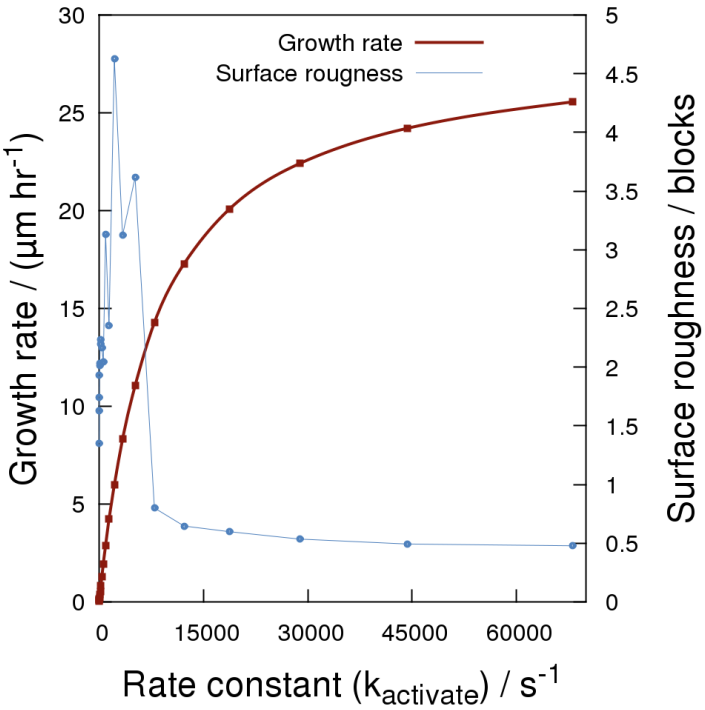

Figure 35-Growth rate and surface roughness as a function of the per site rate constant $k_{activate}$ for the data from the variation of the activation energies of k_{a-i}.

The surface roughness is shown by the blue circles in Figure 35 above. The surface roughness initially increases dramatically with an in increase in $k_{activate}$, but, it then precipitously falls to 0.8 / ML at $k_{activate}$ = 7955 s^{-1}. The surface roughness then steadily levels off to a value of 0.47 / ML which represents a very smooth surface where seen in monolayer growth regimes. This occurs due to the change in importance of other processes as the rate of $k_{activate}$ varies.

As the rate of surface activation increases, the ratio of active to non-active surface sites increases. This leads to more carbon deposition and in this model a corresponding increase in etching as well. This increase in deposition and etching initially occurs at a faster rate than ad-species migration, accounting for the sharp increase in surface roughness at larger $k_{activate}$. However the increase in the rate of

activation and etching levels off as the surface ratio of active/non-active surface sites approaches one. After this the increase in $k_{activate}$ affects the activation of ad species more, and this leads to an exponential increase in the rate of surface ad-species migration.

The growth rate, surface roughness, and per site rate $k_{activate}$ for standard conditions (k_{a-i} with activation energy of 3430 K) are 3.135 μm hr^{-1}, 0.559 / ML, and 929 s^{-1}. The rate constant for reaction a-i (Table 2), as discussed above, was taken from an experimental study of H· reactions on the diamond surface[11]. The experimental value for E_a obtained in this study for the H abstraction reaction was 6680±470 kcal mol^{-1}. This is why the variation amount, $\delta\Delta E_a$, was chosen to be 1 kcal as this is more than twice the experimental error. Our sensitivity analysis of the kMC program to a variation in this value of E_a shows that the results do not change much for this small variation. For simulations with $\delta\Delta E_a$ = ± 1 kcal mol^{-1}, the growth rate is 1.5 times that of the smaller activation energy. This is encouraging for our kMC model as it is not sensitive to the activation energy of reaction a-i within the bounds of the experimental error from which it was obtained.

$k_{deactivate}$

The rate constant for deactivation of surface and ad-species is governed by Equation 4. In theory, it is dependent on both [H·] and [H_2]. However, the rate constant associated with the reverse H abstraction reaction (Equation 5, k_{b-ii}) is so small as to make its contribution to $k_{deactivate}$ negligible. In practice, the rate constant for the deactivation process is dominated by reaction b-i (Table 2) and the [H_2] and k_{b-i} are the more important parameters to test the sensitivity of $k_{deactivate}$. Since the sensitivity to variations in [H_2] was discussed in 3.3.3 above only the test relating to k_{b-i} is examined in this section.

The rate constant k_{b-i} was varied here in the same manner as k_{a-i} was for $k_{activate}$ above. The results for both growth rate and surface roughness presented as a function of the per-site rate constant for $k_{deactivate}$ are shown below in Figure 36.

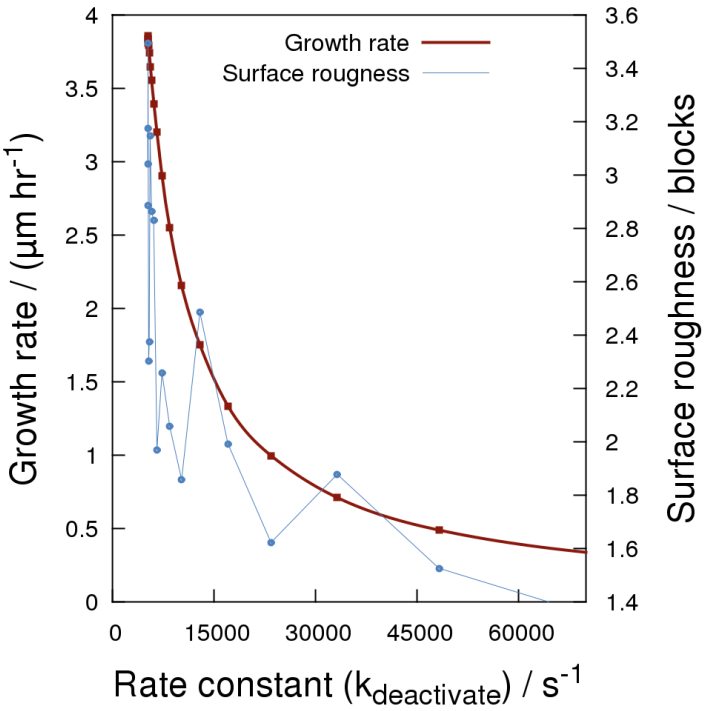

Figure 36-Growth rate and surface roughness as a function of the per site rate constant $k_{deactivate}$ for the data from the variation of the activation energies of $k_{b\text{-}i}$.

The absolute rate of surface site deactivation, $\boldsymbol{r}_{deactivate}$, increases as the activation energy, E_a, of rate constant $k_{b\text{-}i}$ decreases. This increase in $\boldsymbol{r}_{deactivate}$ relative to the absolute rate of surface site activation, $\boldsymbol{r}_{activate}$, leads to fewer 'dangling bonds' on the surface. This means there are fewer sites for carbon containing species to adsorb to on the surface, thus leading to a slower rate of growth as shown in the figure above.

Surface roughness as a function of the rate constant also decreases. This justifies the extension of the model into 3 dimensions as it can be attributed to increased surface migration, which is modelled more accurately in the 3d model. Migration increases proportionally to the rate of CH_3 adsorption but still remains relatively high. There are fewer CH_3 adsorbates landing on the surface, and those

that do have fewer activated surface sites next to them, but migration still occurs relatively frequently when compared with the addition of another growth species. One of the main features of Figure 36 is that slower growth rates produce smoother diamond films. This is an effect that has been observed during experimental growth. [12]

$k_{migration}$

The activation energy in the Arrhenius equation (Equation 10) modelling CH_2 migration on the surface was varied like the previous two energies. The energy was varied in steps of 1 kcal mol^{-1} from the energy used in the standard growth model +/– 10 kcal mol^{-1}. This achieved a range of per site rates for migration between $2.38^{x}10^{6}$ s^{-1} to $1.05^{x}10^{10}$ s^{-1}, which represents a wide range of possible migration rates. Table 2 below shows a list of average migration rates during a simulation with the corresponding input.

Table 7-Results from a series of a number of simulations in which the activation energy of the migration rate constant was varied (column 1). The resulting per site rate determined from the rate constant and the averave overll rate of migration are given.

Energy /J	Rate per site / s^{-1}	Average migration rate / s^{-1}	Standard Dev. / s^{-1}
86560	$8.57\times\times10^{9}$	4006.78	507.505
90744	$5.58\times\times10^{9}$	3785.17	467.525
94928	$3.63\times\times10^{9}$	3717.09	505.638
99112	$2.36\times\times10^{9}$	3917.82	576.773
103296	$1.54\times\times10^{9}$	3707.22	600.366
107480	$1.00\times\times10^{9}$	3925.27	488.732
111664	$6.53\times\times10^{8}$	3618.89	593.086
115848	$4.25\times\times10^{8}$	3738.8	477.734
120032	$2.77\times\times10^{8}$	4058.13	770.65
124216	$1.80\times\times10^{8}$	3976.11	570.305
128400	$1.17\times\times10^{8}$	3744.65	552.279
132584	$7.64\times\times10^{7}$	3930.99	670.972
136768	$4.98\times\times10^{7}$	3767.64	789.378
140952	$3.24\times\times10^{7}$	3768.12	564.994
145136	$2.11\times\times10^{7}$	3784.37	711.979
149320	$1.37\times\times10^{7}$	3766.26	529.955
153504	$8.94\times\times10^{6}$	3704.36	632.606
157688	$5.82\times\times10^{6}$	3806.79	577.247

161872	$3.79\times\times10^{6}$	3714.66	541.146
166056	$2.47\times\times10^{6}$	3702.65	623.239
170240	$1.61\times\times10^{6}$	3621.28	705.388

One interesting detail that emerges from this result is that the actual rate of migration for CH_2 surface species does not depend on the per site rate constant. The rate is being limited by another process, most likely the distribution of activated surface ad–species adjacent to an active surface site. The rate at which this occurs is obviously much slower than the actual migration. This effectively means that if these two species are neighbours then the CH_2 surface ad species will migrate.

Another important result of this test is that neither the growth rate, nor surface roughness showed any correlation with the activation energy for the per site rate constant of migration. It can be seen in Figure 37 below, that the surface roughness approached a limiting roughness typical of MCD simulations. The 21 simulations with varied activation energies did not statistically deviate from this roughness limit. The growth rate for these simulations had an average of 0.883 ± 0.002 μm hr^{-1}. This clearly shows that the kMC model is not sensitive to the activation energy of surface CH_2 migration. Although migration is an important feature of the model, the overall rate of CH2 migration is not sensitive to any errors in activation energy as the availability of an activated site to migrate to determine the overall rate.

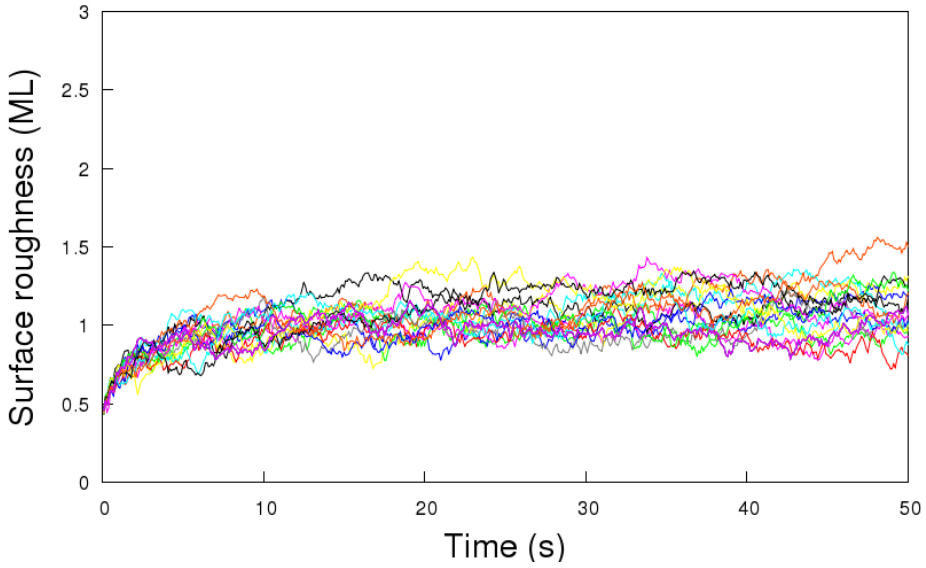

Figure 37-Surface roughness as a function of simulated time for multiple simulations with different values of E_a for the migration rate constant.

k_{etch}

Finally, the sensitivity of the original etching model described by Equation 8 was tested. In this model, the rate constant for etching is a fraction of the rate constant for CH_3 adsorption. Eleven simulations were run using the NCD gas parameters from Table 5 with a 25×25 grid for a total simulated time of 25 s each. The only difference was in the fractional multiplier, *f* from Equation 8. This was varied from 0 to 1 in increments of 0.1.

The only process that was significantly affected by this change was the rate of etching. A strong linear correlation was observed between the rate of etching and the fractional constant *f*, which is obvious. While the rate of CH_3 adsorption did not change, the increased rate of etching led to a linear decrease in growth rates albeit small with a magnitude change of approximately 1 μm hr^{-1}. A linear fit of the growth rate vs percentage of CH_3 adsorption rate gave a rate of change for growth rate as -0.0114 μm hr^{-1} / percent.

3.4. Conclusions

A new 3-dimensional kinetic Monte Carlo (kMC) model of chemical vapour diamond (CVD) growth was introduced. This model is based on extensive theoretical work done previously at the Bristol University diamond group and Moscow state university. A detailed description of the kinetic model of surface reactions involved in CVD diamond was given. This is the kinetic model used as the rate catalogue for the kMC program developed during the course of this work.

The parameter space of the model was systematically explored to determine its sensitivity of output to the input parameters gathered from experiments and theoretical calculations. Each simulation was performed with a sufficiently large surface and long simulation time to be considered statistically equilibrated (sections 3.3.1 and 3.3.2). It was found that the growth rates and surface roughness are most sensitive to the concentration of CH_3 as this affects the rate of adsorption. This is the one rate that determines the general output more than any of the others. Variations in the other gas concentration [H] and [H_2] did not affect the output as dramatically.

The temperature of the substrate is a measure that can easily be compared directly with experiment. It has been found that the growth rate of CVD diamond increases with temperature but then decreases after a point. Other kMC models of diamond growth have been unable to reproduce this peak, but this model has. These results were compared with other computations [13,29] and experimental data. [23]

The variation in the rate constants $k_{activate}$, $k_{deactivate}$, $k_{migration}$, and k_{etch} has been analysed. It was found that the model reproduces smoother surfaces at slower growth rates which have also been observed experimentally. [12] The absolute rate of CH_2 migration is not greatly affected by change in the per-site rate constant, which means that accurate information about the energetics of the

process is not that important as this process is regulated by the number of available surface sites available for migration.

3.5. References

(1) May, P. W.; Harvey, J. N.; Allan, N. L.; Richley, J. C.; Mankelevich, Y. A. Simulations of Chemical Vapor Deposition Diamond Film Growth Using a Kinetic Monte Carlo Model and Two-Dimensional Models of Microwave Plasma and Hot Filament Chemical Vapor Deposition Reactors. *J. Appl. Phys.* **2010**, *108*, 114909.

(2) May, P. W.; Harvey, J. N.; Allan, N. L.; Richley, J. C.; Mankelevich, Y. A. Simulations of Chemical Vapor Deposition Diamond Film Growth Using a Kinetic Monte Carlo Model. *J. Appl. Phys.* **2010**, *108*, 014905.

(3) May, P. W.; Allan, N. L.; Ashfold, M. N. R.; Richley, J. C.; Mankelevich, Y. A. Simplified Monte Carlo Simulations of Chemical Vapour Deposition Diamond Growth. *J. Phys. Condens. Matter* **2009**, *21*, 364203.

(4) May, P. W.; Mankelevich, Y. A. Experiment and Modeling of the Deposition of Ultrananocrystalline Diamond Films Using Hot Filament Chemical Vapor Deposition and Ar/CH4/H2 Gas Mixtures: A Generalized Mechanism for Ultrananocrystalline Diamond Growth. *J. Appl. Phys.* **2006**, *100*, 024301.

(5) May, P. W.; Ashfold, M. N. R.; Mankelevich, Y. A. Microcrystalline, Nanocrystalline, and Ultrananocrystalline Diamond Chemical Vapor Deposition: Experiment and Modeling of the Factors Controlling Growth Rate, Nucleation, and Crystal Size. *J. Appl. Phys.* **2007**, *101*, 053115.

(6) Cheesman, A.; Harvey, J. N.; Ashfold, M. N. R. Studies of Carbon Incorporation on the Diamond {100} Surface during Chemical Vapor Deposition Using Density Functional Theory. *J. Phys. Chem. A* **2008**, *112*, 11436–11448.

(7) Richley, J. C.; Harvey, J. N.; Ashfold, M. N. R. On the Role of Carbon Radical Insertion Reactions in the Growth of Diamond by Chemical Vapor Deposition Methods. *J. Phys. Chem. A* **2009**, *113*, 11416–11422.

(8) Voter, A. F. INTRODUCTION TO THE KINETIC MONTE CARLO METHOD. In *Radiation Effects in Solids*; Sickafus, K. E.; Kotomin, E. A.; Uberuaga, B. P., Eds.; NATO Science Series; Springer Netherlands, 2007; pp. 1–23.

(9) Amar, J. G. The Monte Carlo Method in Science and Engineering. *Comput. Sci. Eng.* **2006**, *8*, 9–19.

(10) Cantrell, R. A.; Clancy, P. A New Kinetic Monte Carlo Algorithm for Heteroepitactical Growth: Case Study of C-60 Growth on Pentacene. *J. Chem. Theory Comput.* **2012**, *8*, 1048–1057.

(11) Krasnoperov, L. N.; Kalinovski, I. J.; Chu, H. N.; Gutman, D. Heterogeneous Reactions of Hydrogen Atoms and Methyl Radicals with a Diamond Surface in the 300-1133 K Temperature Range. *J. Phys. Chem.* **1993**, *97*, 11787–11796.

(12) Battaile, C. C.; Srolovitz, D. J.; Oleinik, I. I.; Pettifor, D. G.; Sutton, A. P.; Harris, S. J.; Butler, J. E. Etching Effects during the Chemical Vapor Deposition of (100) Diamond. *J. Chem. Phys.* **1999**, *111*, 4291–4299.

(13) Netto, A.; Frenklach, M. Kinetic Monte Carlo Simulations of CVD Diamond growth—Interlay among Growth, Etching, and Migration. *Diam. Relat. Mater.* **2005**, *14*, 1630–1646.
(14) Richley, J. Fundamental Studies of Diamond Chemical Vapour Deposition: Plasma Diagnostics and Computer Modelling. PhD, University of Bristol, 2011.
(15) Frenklach, M.; Skokov, S. Surface Migration in Diamond Growth. *J. Phys. Chem. B* **1997**, *101*, 3025–3036.
(16) Richley, J. C.; Harvey, J. N.; Ashfold, M. N. R. CH2 Group Migration between H-Terminated 2 X 1 Reconstructed {100} and {111} Surfaces of Diamond. *J. Phys. Chem. C* **2012**, *116*, 7810–7816.
(17) Goodwin, D. G.; Butler, J. E. Chapter 11. In *Handbook of industrial Diamond and Diamond Films*; Prelas, M. A.; Popovici, A.; Bigelow, L. K., Eds.; Marcel Dekker Inc., 1998; pp. 527–581.
(18) Chatterjee, A.; Voter, A. F. Accurate Acceleration of Kinetic Monte Carlo Simulations through the Modification of Rate Constants. *J. Chem. Phys.* **2010**, *132*, 194101.
(19) Voter, A. F.; Montalenti, F.; Germann, T. C. Extending the Time Scale in Atomistic Simulation of Materials. *Annu. Rev. Mater. Res.* **2002**, *32*, 321–346.
(20) Landau, D. P.; Binder, K. *A Guide to Monte Carlo Simulations in Statistical Physics*; Cambridge University Press, 2009.
(21) Stukowski, A. Visualization and Analysis of Atomistic Simulation Data with OVITO–the Open Visualization Tool. *Model. Simul. Mater. Sci. Eng.* **2010**, *18*, 015012.
(22) Butler, J. E.; Woodin, R. L.; Brown, L. M.; Fallon, P. Thin Film Diamond Growth Mechanisms [and Comment]. *Philos. Trans. R. Soc. Lond. Ser. Phys. Eng. Sci.* **1993**, *342*, 209–224.
(23) Kweon, D.-W.; Lee, J.-Y.; Kim, D. The Growth Kinetics of Diamond Films Deposited by Hot-filament Chemical Vapor Deposition. *J. Appl. Phys.* **1991**, *69*, 8329–8335.
(24) Kondoh, E.; Ohta, T.; Mitomo, T.; Ohtsuka, K. Determination of Activation Energies for Diamond Growth by an Advanced Hot Filament Chemical Vapor Deposition Method. *Appl. Phys. Lett.* **1991**, *59*, 488–490.
(25) Fang, P. H. Temperature Dependence of Growth Rate of Diamond. *Appl. Phys. Lett.* **1995**, *66*, 2739–2741.
(26) Grujicic, M.; Lai, S. G. Multi-Length Scale Modeling of CVD of Diamond Part II A Combined Atomic-Scale/grain-Scale Analysis. *J. Mater. Sci.* **2000**, *35*, 5371–5381.
(27) Ma, J.; Richley, J. C.; Ashfold, M. N. R.; Mankelevich, Y. A. Probing the Plasma Chemistry in a Microwave Reactor Used for Diamond Chemical Vapor Deposition by Cavity Ring down Spectroscopy. *J. Appl. Phys.* **2008**, *104*, 103305.
(28) Mankelevich, Y. A.; Ashfold, M. N. R.; Ma, J. Plasma-Chemical Processes in Microwave Plasma-Enhanced Chemical Vapor Deposition Reactors Operating with C/H/Ar Gas Mixtures. *J. Appl. Phys.* **2008**, *104*, 113304.
(29) Battaile, C. C.; Srolovitz, D. J. Kinetic Monte Carlo Simulation of Chemical Vapor Deposition. *Annu. Rev. Mater. Res.* **2002**, *32*, 297–319.

Chapter 4

Surface morphology studies

4.1. Introduction

In this Chapter the surface morphology of the diamond 'grown' using the 3-dimensional kinetic Monte Carlo (kMC) model is investigated. It was shown in Chapter 3 that the geometric configuration of molecules around a reacting site in the model will affect the rate of that reaction in different ways compared to the 2-dimensional model. This difference is most evident in the resulting surface structures formed by these reactions (e.g. different size and qualities of polycrystalline diamond films).

There are three surface restructuring processes in the model that will affect the surface morphology most: CH_3 etching, CH_3 adsorption, and migration. Changes to how the etching and adsorption of CH_3 are modelled from previous studies are examined, and the effects these changes have on the resultant surface are discussed. Although the way migration is modelled was not changed from the previous model, its effect on surface structure was systematically tested by comparing results from growth with migration turned off with results from normal growth.

4.1.1. Surface structure metric

In the work presented thus far, the only metric of surface structure presented has been the standard deviation of the surface height, which has been investigated as a function of time. While this is a customary measure of surface roughness used in surface sciences, by itself it lacks the detail necessary to differentiate between different surfaces with a similar standard deviation. A

simple but instructive example is shown below showing how the surface roughness measure is unable to distinguish between peaks and troughs on a surface. Figure 38b is a pyramid, and Figure 38b is an exact inversion of this pyramid. Both of these structures have a surface roughness measurement of 2.469 ML.

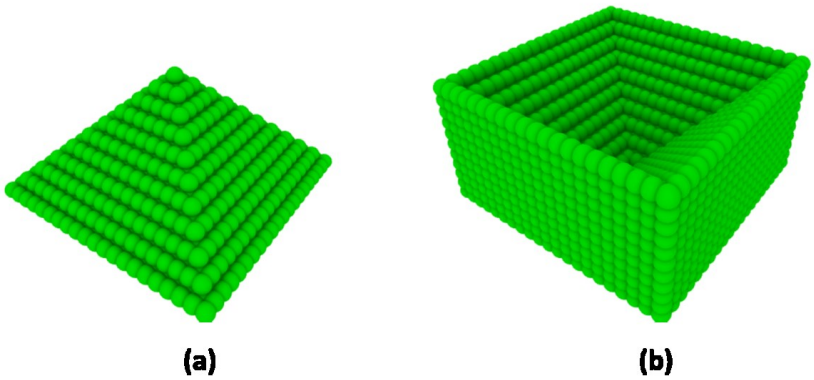

Figure 38-A pyramid in figure (a) and an exact inversion of this pyramid in figure (b)

There is clearly a significant difference between the two structures shown in the above figure even though they both have the exact same value for the roughness parameter discussed in Chapter 3. Clearly another numerical value to quantify this difference is required. In surface engineering the statistical distribution of the surface heights is analysed to determine the type of surface being probed.[1,2] The median (R_M), arithmetic mean (R_a), standard deviation (R_{SD}) are used to determine the roughness of the surface (R_{SD}), which has already been discussed, the averaged surface height (R_a), and R_M is used to determine whether the mean is normally distributed. Two more statistical moments are also used; the skewness (R_{sk}) is third standardised moment, which measures how the data is 'skewed' around the mean, and kurtosis (R_{ku}) which measures the 'peakedness' of the distribution is the fourth standard moment. In Figure 38 above, the pyramid has a positive R_{sk} value while the inverted pyramid has a negative R_{sk} value. A diagram of how these are related to a 2-dimensional profile is shown below in a figure taken from surface study of optics.[3] Figure 39a shows two

surface profiles whose surface height distributions have positive and negative skewness respectively. The surface with an $R_{sk} > 0$ has more peaks than troughs, where the opposite is true for surfaces with an $R_{sk} < 0$. For the kurtosis of a distribution (Figure 39b), a peaked distribution $R_{ku} > 0$ the surface is more spiked whereas if $R_{ku} < 0$ (i.e. a flatter distribution) then the surface will have broader peaks that are more plateau-like.

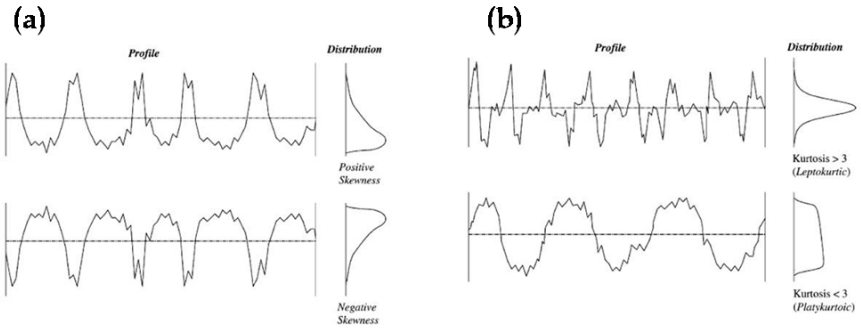

Figure 39–Illustration of how the shape of a surface height distribution is affected by the surface structure [3] (a) skewness (R_{sk}) shows whether the surface has more peaks or pits and (b) the kurtosis demonstrates the smoothness or sharpness of the surface peaks. Reproduced from [3].

The distribution of surface heights and their statistical moments are used in the work below to better quantify the types of surfaces produced from the various surface structuring process models.

4.1.2. Critical nucleus

The mechanism by which the nucleation of a new layer occurs in chemical vapour deposition (CVD) diamond growth has been discussed in the literature.[4,5] In the work published previously by our group for the 2-dimensional model [5–9] the critical nucleus was assumed to be a 2 'block' dimer. This was the smallest number of 'blocks' (carbon containing species) that could nucleate a new layer of growth. However this was never explicitly proven by monitoring the growth behaviour in detail, and activated surface blocks were allowed to etch. It has been suggested that the critical nucleus could be as large as four on the (111) surface.[4]

A method to determine the smallest configuration in the new 3-dimensional kMC model which constituted a new layer of growth was developed. A post processing program was created that monitored the following properties after each surface restructuring event (adsorption, etching, and migration): monomer creation, monomer growth, monomer loss, dimer growth, dimer loss. A monomer creation event occurs after a CH_X (block) lands on the surface or migrates to a position on the surface where there are no neighbouring sites where the surface level is greater than or equal to the surface site in question. A monomer growth event occurs when a monomer migrates next to another block or existing terrace of n-block size, or if a block lands adjacent creating a dimer or completing an n-block row or terrace. A dimer growth is the same but with an initial 2-block unit. A monomer loss is when one block with no nearest neighbours migrates or is etched away. A dimer loss is in the same vein as a monomer loss, but with an initial 2-block set with no other nearest neighbours.

Keeping track of dimer growth events, including all of the possible events such as 2-mer to 9-mer, or dimer to n-mer became computationally expensive and complex; the expense and complexity increased considerably when monitoring trimer growth and loss. It was therefore decided that it would be sufficient to only proceed up to dimer growth and loss as this study could be more narrowly concerned with whether or not the dimer was the critical nucleus. If the critical nucleus was found to be larger than a 2-block configuration then a modified method for evaluating the critical nucleus would be devised.

4.2. Etching

In Chapter 3 the three different models (Equations 3.8 – 3.11) that have been used to simulate the etching of carbon from the diamond surface under CVD conditions are described. This effect has been observed experimentally [10], but the mechanism by which this occurs is still debated in the literature [5,11–13]. In this section the results from a series of simulations using each model separately are discussed.

4.2.1. Computational detail

Simulations were conducted for each etching model defined in Chapter 3 using the reactor conditions from five different growth regimes taken from gas phase reactor modelling. [14] These growth parameters can be found below in Table 8; they include the concentration of gases involved in the growth process, the temperature of the growing substrate and the gas layer near the substrate, as well as the steric parameters for the growth species (Chapter 3). Each individual simulation was carried out on a 50×50 grid and run for a sufficient time to be statistically equilibrated.

Table 8 - Gas and temperature conditions for CVD diamond growth modelling single crystal (SCD), microcrystalline (MCD), nanocrystilline (NCD), and ultra-nanocrystilline (UNCD) diamond (both from hot filament (HF) and microwave (MW) type reactors). (s and g are steric parameters for the growth species described in Chapter 3).

	SCD	MCD	NCD	UNCD(HF)	UNCD(MW)
[H·] / cm^{-3}	3.38×10^{16}	1.85×10^{14}	1.52×10^{14}	3.00×10^{13}	4.31×10^{14}
[H_2] / cm^{-3}	9.33×10^{17}	1.52×10^{17}	1.51×10^{17}	1.83×10^{17}	2.06×10^{16}
[CH_3·] / cm^{-3}	3.24×10^{15}	1.46×10^{13}	5.68×10^{13}	3.82×10^{13}	5.60×10^{11}
s	0.50	0.50	0.50	0.50	0.50
g	0.15	0.15	0.15	0.15	0.15
[CH_2·] / cm^{-3}	1.02×10^{12}	3.66×10^{10}	8.12×10^{10}	1.55×10^{10}	2.31×10^{9}
s	0.60	0.60	0.60	0.60	0.60
g	0.20	0.20	0.20	0.20	0.20
[CH·] / cm^{-3}	1.60×10^{13}	2.74×10^{8}	6.53×10^{8}	5.28×10^{7}	7.05×10^{8}
s	0.70	0.70	0.70	0.70	0.70
g	0.25	0.25	0.25	0.25	0.25
[C·] / cm^{-3}	1.41×10^{12}	3.37×10^{9}	5.45×10^{9}	1.05×10^{7}	$1.47E\times10^{11}$
s	1.00	1.00	1.00	1.00	1.00
g	0.30	0.30	0.30	0.30	0.30
T_s / K	973	1173	1173	1173	873
T_{ns} / K	1736	1267	1267	1145	1263

In order to directly compare the results from all three models it was necessary for each model to have similar rate constants for the initial configuration where an activated adatom had no next nearest neighbour (NN=0). The original model for CH_3 etching,[9] governed by Equation 3.8, was merely the

function of a linear scaling parameter, *f*, in order to get k_{etch} to equal a fraction of k_{CHxadd} , as it has been observed in experiment that the two are related.[10,15] The original rate k_{etch} was set equal to the Eyring etching model k_{eyring} (Equation 1) and this expression was then solved for *f* (Equation 2).

$$k_{etch} = f k_{CH_x add} = \frac{k_B T_s}{h} exp\left(\frac{-\Delta G^{\ddagger}_{etch}}{RT_s}\right) \quad (1)$$

$$f = \left(\frac{k_B T_s}{h} exp\left(\frac{-\Delta G^{\ddagger}_{etch}}{RT_s}\right)\right) \frac{1}{k_{CH_x add}} \quad (2)$$

Each rate constant for CH_3 adsorption is different for the five growth regimes shown in Table 8 due to the different concentrations of CH_3 above the surface in each model CVD reactor. Therefore, in the original model for etching the value of k_{etch} will be different for each growth system if the value of *f* is constant. However, the Eyring model of etching is dependent on the temperature of the growing substrate, T_s, not gas concentration for determining the rate constant for etching. In the five reactor models, there are only three different values for T_s. In the growth models for MCD, NCD, and ultra nanocrystalline diamond grown in a hot filament reactor UNCD(HF) T_s = 1173 K while for single crystalline diamond (SCD) and ultra nanocrystalline diamond grown in a microwave plasma reactor UNCD(MW) T_s = 976 K and 873 K respectively. Thus there are only three different values of k_{eyring} for the five simulated conditions. Equation 2 was solved for all of the values of k_{eyring} and k_{CH3add}, and the solutions for *f* and the resultant value of k_{etch} for that *f* when back substituted into Equation 1 are found below in Table 9.

Table 9-Calculating the ***f*** *parameter for the original model of etching by comparing* $\boldsymbol{k_{etch}}$ *and* $\boldsymbol{k_{eyring}}$ *for each of the growth conditions from Table 1.*

	SCD	MCD	NCD	UNCD(HF)	UNCD(MW)
$\boldsymbol{k_{CH3add}}$	6095.34	23.46	91.29	58.36	0.90
$\boldsymbol{k_{etch}}$	2.81	527.73	527.73	527.73	0.08
$\boldsymbol{k_{eyring}}$	2.81	527.73	527.73	527.73	0.08
f	0.00046	22.49	5.78	9.04	0.095

4.2.2. Results

Comparison of etching models

A number of results from the set of simulations described above are shown in Figure 40; different measures are compared across etching model types and arranged according to growth conditions. Frames (a), (b), and (c) deal with the CH_3 adsorption rate, the average etching rate, and the ratio of the two respectively. Only the etching model differs between these calculations, but clearly the overall rate of CH_3 adsorption (Figure 1a) as well as overall rate of etching (Figure 1b) is affected by this difference. Most of the simulated growth regimes follow the same pattern across the different etching models. For example, both CH_3 adsorption and etching rates increase dramatically from the original model to the linear model, and then decrease slightly with the exponential model. This is due to an increased etching rate creating more adsorption sites and the exponential model having a slightly slower rate of etching as the value of $\boldsymbol{k_{etch}}$ for NN=1,2,3,4 is less than the equivalent value of $\boldsymbol{k_{etch}}$ for the linear model of etching.

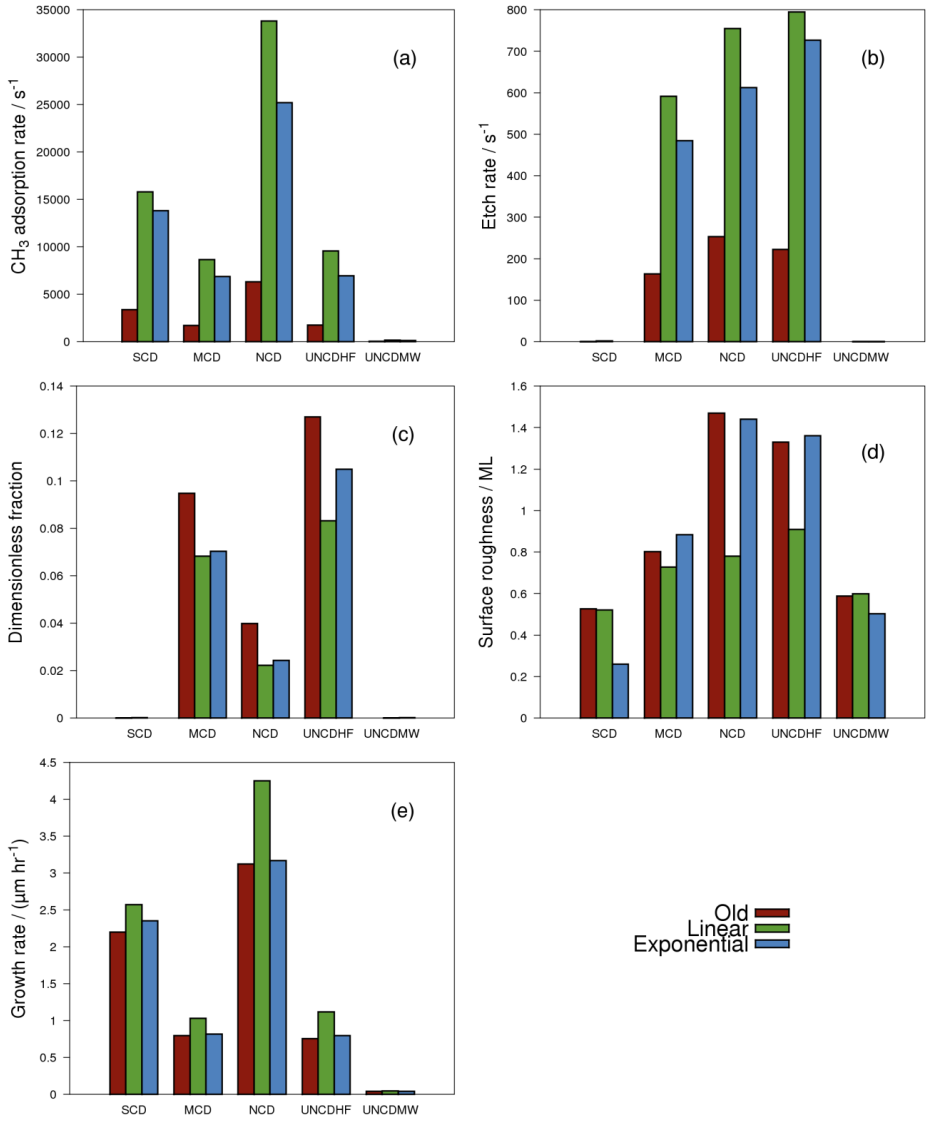

Figure 40-Results from the simulation of SCD, MCD, NCD, and UNCD growth for all three etching models described above and in Chapter 3. The results in plot (a) are the average rate of CH_3 adsorption ($\mathbf{r}_{CH3add}$) for each simulation, plot (b) is the average etching rate ($\mathbf{r}_{etch}$), (c) is the ratio of the two $\mathbf{r}_{etch}/\mathbf{r}_{CH3add,}$ (d) is the average surface roughness for each simulation and (e) is the corresponding total growth rate.

Surface height probability distributions

Surface roughness, in frame (d) of Figure 40, is the only measure of morphology given in that figure. This is an average of the final two-thirds of the surface roughness versus time plot which is the standard deviation of the height profile (Chapter 3). This measure by itself is a blunt tool with which to quantify detailed differences in surface morphology. The surface roughness, or the standard deviation of the surface height profile, describes the absolute deviation of the height over the whole surface. A surface with deep pits can have a surface roughness measure similar to another surface with sharp peaks. Therefore it will be necessary here to use other statistical measures based on the surface height distribution, which were discussed in section 4.1. Namely, R_M – median, R_a – arithmetic mean, R_{SD} – standard deviation, R_{sk} - skewness, and R_{ku} – kurtosis.

Each of these measurements is a description of a unique characteristic of a probability distribution; in this context, a distribution of surface height. In Figure 41 the normalised probability distributions of the simulated surfaces from the SCD, MCD, NCD, UNCD(HF), and UNCD(MW) growth conditions described above are presented. The results from these simulations for the five reactor conditions are directly compared between each model of etching; the original model, the Eyring model with linear dependence on the number of nearest neighbours, and the Eyring model with exponential dependence on the number of nearest neighbours. The statistical measures describing each of these distributions are presented in section 4.1.1.

There are two distinct features of Figure 4 that are immediately noticeable. The first is that the surface height distributions for SCD simulations in all models of etching appear to be similar, while the distributions for the other growth models have different distributions for different etching models. This is due to the lack of any substantial etching in any of the SCD growth regimes. Although this is also the case for the UNCD(MW) regime, but the distribution are not the same shape. The other feature that stands out is that the linear Eyring model of etching produces a distinct distribution of surface heights for all of the other growth regimes, while many of the distributions from the original model are

similar in appearance to the distributions produced for the exponential Eyring model of etching.

This distinction between the linear model and the other two etching models can be further investigated by comparing some the statistical measures of each distribution (Table 3) with the others of the same growth regime. Except for the mean and median values, which were chosen to be the same across a growth regime, the statistics confirm our visual deduction that the linear etching model produces a quantifiably different surface morphology from the original and exponential models.

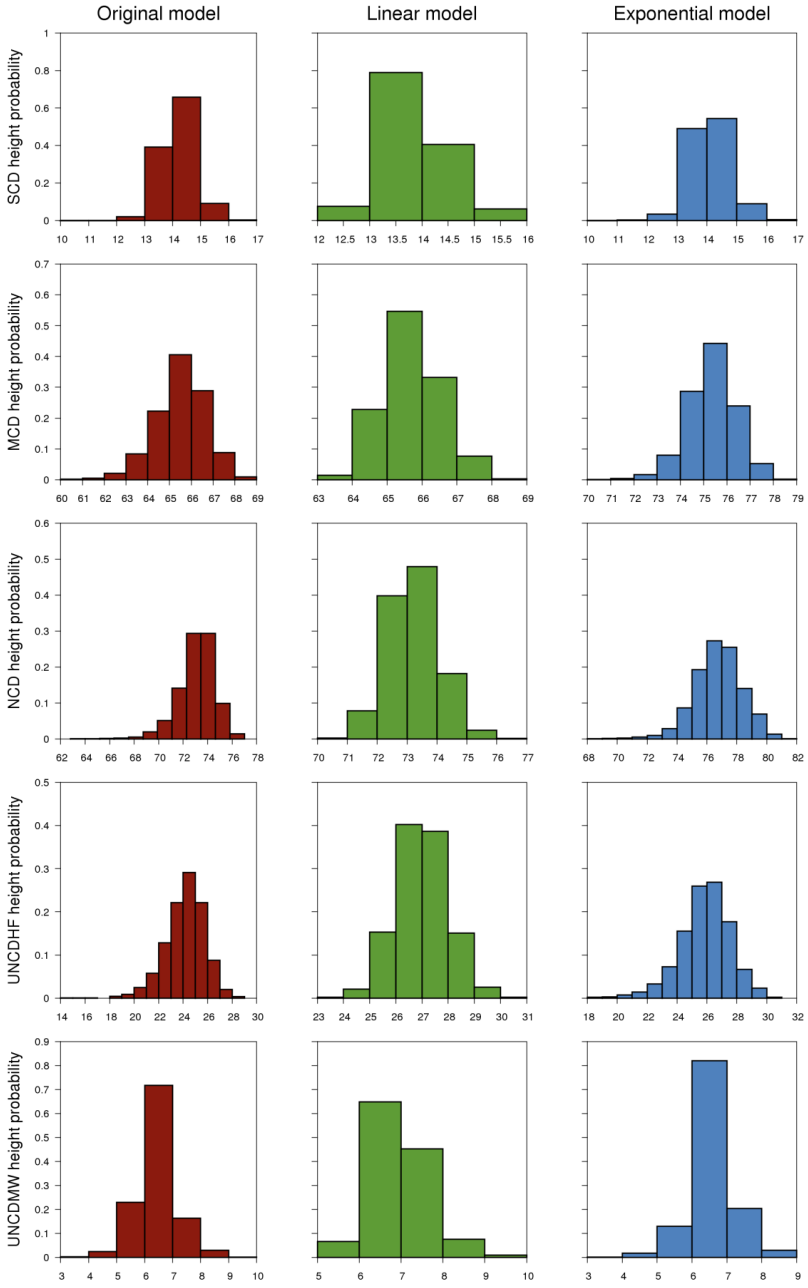

Figure 41-Normalised probability distributions of the final surface height for the set of results discussed above and in Figure 40. The red, green, and blue distributions are of the results from the original etching model, the Eyring model with a linear NN dependency, and the Eyring model with an exponential dependency on the NN.

There are two distinct features of Figure 41 that are immediately noticeable. The first is that the surface height distributions for SCD simulations in all models of etching appear to be similar, while those produced from the other growth models have different distributions for different etching models. This is due to the lack of any substantial etching in any of the SCD growth regimes. Although this is also the case for the UNCD(MW) regime, but the distribution are not the same shape. The second feature is that the linear Eyring model of etching produces a distinct distribution of surface heights for all of the other growth regimes. While many of the distributions from the original model are similar in appearance to those produced for the exponential Eyring model of etching.

This distinction between the linear model and the other two etching models can be further investigated by comparing statistical measures of each distribution (Table 10) with the others of the same growth regime. Except for the mean and median values, which were chosen to be the same across a growth regime, the statistics confirm our visual deduction that the linear etching model produces a quantifiably different surface morphology from the original and exponential models.

Table 10-Statistical measures related to the distributions shown in Figure 41.

		Original Model	**Linear model**	**Exponential model**
SCD	R_M	15	14	15
	R_a	14.7080	14.3392	14.5984
	R_{SD}	0.6489	0.6562	0.7068
	R_{Sk}	-0.0929	0.4887	0.0912
	R_{ku}	0.5163	0.2359	0.5265
MCD	R_M	66	66	76
	R_a	66.0124	66.1972	75.8512
	R_{SD}	1.1830	0.8671	1.0678
	R_{Sk}	-0.4023	0.1716	-0.3381
	R_{ku}	0.5274	-0.1601	0.6122
NCD	R_M	73	74	77
	R_a	73.2024	73.7188	77.2400
	R_{SD}	1.2918	0.8970	1.6285
	R_{Sk}	-0.9067	0.1659	-0.4181
	R_{ku}	2.6010	0.0428	0.9796
UNCD(HF)	R_M	25	27	26
	R_a	24.6584	27.5000	26.3688
	R_{SD}	1.6329	1.0344	1.7158
	R_{Sk}	-0.6775	0.0488	-0.5803
	R_{ku}	1.6380	0.1029	1.0779
UNCD(MW)	R_M	7	7	7
	R_a	6.9504	7.4516	7.0820
	R_{SD}	0.7337	0.7186	0.6555
	R_{Sk}	0.0654	0.5254	0.1099
	R_{ku}	1.3407	0.5159	1.8925

In the results presented in Table 10, including the SCD simulations, the kurtosis is similar in both the original and the exponential models, but less similar for the linear model. This reflects having larger flat plateaus. An example of this can be seen in a visualisation of the surfaces for the NCD growth simulations (Figure 42-Figure 44). Both Figure 42 and Figure 44 have pronounced hillocks and valleys. However, Figure 43 (linear etching model) shows large continuous plateaus. This is possibly due to the fact that the ratio of etching to CH_3 adsorption is lowest with the linear etching model for MCD, NCD, and UNCD(HF) growth simulations (Figure 40 (c)). These are also the growth

regimes that show the linear etching model with the lowest average surface roughness values (Figure 40 (d)).

Surface visualisation

It is useful to visualise the surfaces that produced the probability distributions shown in Figure 40 with the subsequent statistics from Table 10 to understand how these compare with the actual modelled surface. However, to produce an image from each surface reported above would be unnecessary. It is sufficient to look at one set of images from a selected growth regime across all three etching models and generalise how the statistics of the height distribution are related to an image of the surface. The images that follow are an in-plane view of the growing surface. So if the growing (100) surface is the z-coordinate then these images represent the xy-plane. The grayscale used is to give perspective. Black is the colour of the deepest point and white of the highest point on the surface.

The surfaces of the NCD simulations were chosen for visualisation, as their statistics are varied and the growth has a significant proportion of etching. The first snapshot (Figure 42) is of a surface with an average height of 73.2 ML and was simulated using the original model of etching. The surface has small hillocks with deeper small wells at various places on the surface; this is described by the negative R_{sk} value. The relatively high positive kurtosis value means that the distribution of surface heights is more peaked with a light tail. This means that the surface hillocks are more plateau like, and combined with the negative skewness this means that there are deep pits distributed amongst flat hillocks.

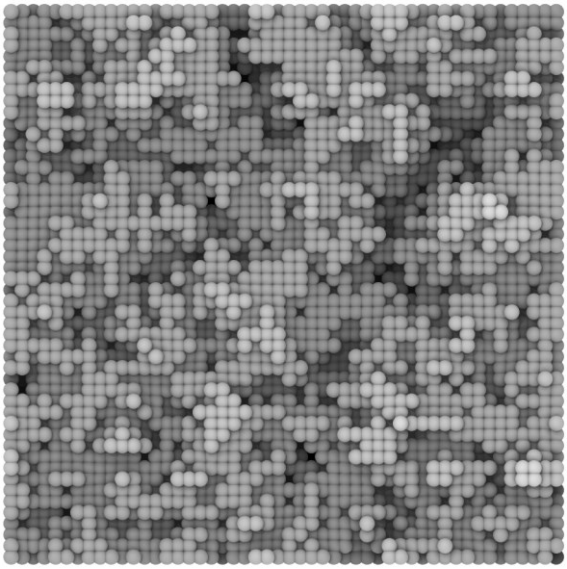

Figure 42-Snapshot of the simulated surface of a CVD diamond grown under NCD conditions with a 50×50 grid using the original model for etching.

The second snapshot (Figure 43) shows the surface used to calculate the height distribution for the NCD surface with the linear model of etching. The average surface height is 73.7 ML, similar to that of Figure 42. This is a good example of a low R_{ku} value of which the larger flat terraces are indicative. Also, having a relatively non-skewed distribution implies that there are no discernible pits or peaks in the surface. This is backed up by the instantaneous surface roughness measure, $R_{SD,}$ which is the smallest of those obtained with the three models of etching for NCD growth. The corresponding surface is in fact approximately half as rough as that obtained with the exponential model and two-thirds as rough as the one generated by the original model.

Figure 44 shows a surface with an R_a value of 77.2 ML, again a similar average height of the other two surfaces. This surface was simulated with the exponential model of NN dependence for etching. There are a greater number of smaller terraces i.e. more nucleation sites that are not merging into larger terraces due to migration before a new nucleation site on the next layer has a chance to

form. Qualitatively Figure 45 looks much like Figure 43, the surface grown with the original model.

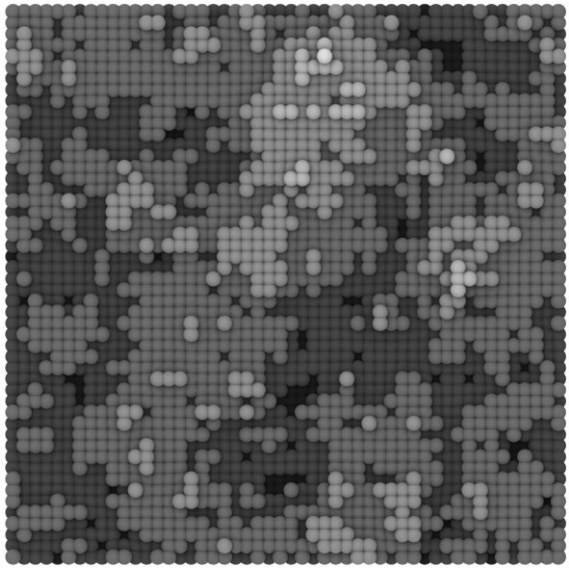

Figure 43-Snapshot of the simulated surface of a CVD diamond grown under NCD conditions with a 50×50 grid using the Eyring model for etching with a linear dependence on next nearest neighbour.

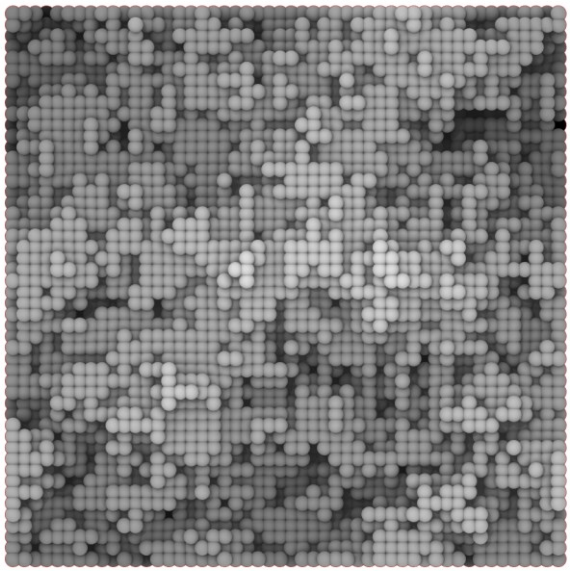

Figure 44-snapshot of the simulated surface of a CVD diamond grown under NCD conditions with a 50×50 grid using the Eyring model for etching with an exponential dependence on next nearest neighbour.

Quantitatively the surface roughness and skewness are similar. That means they are both rougher (R_{SD}) than the surface from the linear model and have more pits (R_{sk}) than mounds. However the value of R_{ku} for the exponential model means that the peaks are sharper than on the surface from the original model.

Critical nucleus

Another aspect of surface morphology that was measured, as discussed in Section 4.1.2, is the critical nucleus of a new layer which was described at the beginning of this chapter. The first pertinent piece of information to point out is the fact that the critical nucleus for all growth regimes in all models of etching is the two block dimer. This was the same number of blocks that was assumed to be the smallest number of immobile and unetchable blocks on the surface that led to a new layer in the 2-dimensional model.

Table 11-Fraction of monomer creation, growth, loss, dimer growth, and loss out of a total possible number of surface restructuring events for the five growth conditions listed in Table 8. The values for the original model (OM), linear model (LM), and exponential model (EM) are directly compared for each growth regime.

		Monomer creation	**Monomer Growth**	**Monomer Loss**	**Dimer growth**	**Dimer Loss**
SCD	OM	0.88538	0.00189	0.88390	0.00218	0.00045
	LM	0.87497	0.00194	0.87340	0.00241	0.00042
	EM	0.88411	0.00203	0.88253	0.00258	0.00048
MCD	OM	0.71001	0.00895	0.70205	0.01019	0.00224
	LM	0.71727	0.00946	0.70870	0.00991	0.00248
	EM	0.70944	0.00915	0.70145	0.00979	0.00241
NCD	OM	0.56703	0.01747	0.54978	0.01806	0.00368
	LM	0.58492	0.01869	0.56550	0.01786	0.00406
	EM	0.55466	0.01694	0.53763	0.01732	0.00344
UNCD(HF)	OM	0.46302	0.02985	0.42772	0.03024	0.00277
	LM	0.44951	0.03134	0.40878	0.02855	0.00350
	EM	0.48126	0.03183	0.44397	0.03247	0.00327
UNCD(MW)	OM	0.85622	0.00321	0.85347	0.00381	0.00057
	LM	0.82775	0.00322	0.82481	0.00410	0.00042
	EM	0.83420	0.00304	0.83147	0.00428	0.00040

While the critical nucleus was the same for all growth regimes in all etching models this does not mean there is nothing to say about these results in general. The fraction of monomer creation appears to be loosely related to the average crystal size observed experimentally for each simulated reactor type. For SCD growth the fraction of monomer creation is 0.88 on average; this is the largest of all growth types. Moving on to polycrystalline growth, the fraction of monomer creation for the MCD simulation is an average of approximately 0.71. This trend continues as the crystal size decreases (NCD and UNCD), and the fraction of total events that are monomer creations decreases as well. This can be attributed to polycrystalline growth regimes having more unique islands and thus having a greater chance of any single event involving a configuration greater than a single monomer. This is true with the exception of the results for (MW)UNCD growth, which more closely resemble SCD growth in all of the measures taken in this work.

4.3. CH_3 adsorption

In this section the effect of nearest neighbour geometry on the surface morphology of the CVD diamond surface is discussed. In Chapter 3 the rate constant for CH_3 adsorption was introduced and the possible influence of local geometry on the adsorbing site was postulated. In most of the work using the kMC model in this thesis there is no nearest neighbour (NN) dependence. However, here this dependence is investigated and compared with a control growth without NN dependence on CH_3 adsorption.

4.3.1. Computational detail

All of the results presented thus far have used a model for CH3 adsorption where its rate is not dependent on the configuration of the geometry surrounding the site. This model, described in Chapter 3, is governed by Equation 3.7. This approximation was more acceptable in the previous 2-dimensional model, however, as in 3-dimensions the effect of local structure will be more pronounced. The model was changed to have a simple inverse linear dependence of the adsorption rate constant on the number of nearest neighbour surrounding the site to which the CH_3 molecule is adsorbing. The amended expression for the rate constant for CH_3 adsorption is shown by Equation 3 below.

$$k_{\mathrm{CH}_x\mathrm{add}} = \frac{s_{\mathrm{CH}_x} g_{\mathrm{CH}_x} [\mathrm{CH}_x] \overline{v}}{4N_S(N_N+1)} \tag{3}$$

Simulations from each growth regime (Table 8) were completed using this new model of adsorption. Each simulation used a 50×50 grid and was executed until statistical equilibration (i.e. steady state rates) was achieved. The final surface of each simulation was analysed as in the previous section with a statistical distribution of the surface height and a visualisation of the final surface.

4.3.2. Results

Surface height probability distributions

Figure 45 shows each surface height probability distributions for all simulations of each reactor type done with the new CH_3 adsorption rate constant (Equation 3.7a) using the exponential model of etching. These are compared with the results from the exponential model of etching without the change in CH_3 adsorption. The juxtaposition of the two sets of results very clearly shows that a drastic change has occurred due to the addition of NN dependency in the CH_3 adsorption rate constant. However, the SCD and (MW) UNCD results show much less change than any of the other reactor types.

The rest of the results (MCD, NCD, and (HF) UNCD) for the NN dependency have distributions with similar shapes. These distributions are all positively skewed; the MCD and NCD results have a long fat tail (i.e. $R_{ku} < 0$) and the (HF) UNCD are more normally distributed. The statistics for all of these distributions and the base distributions are given below in Table 12.

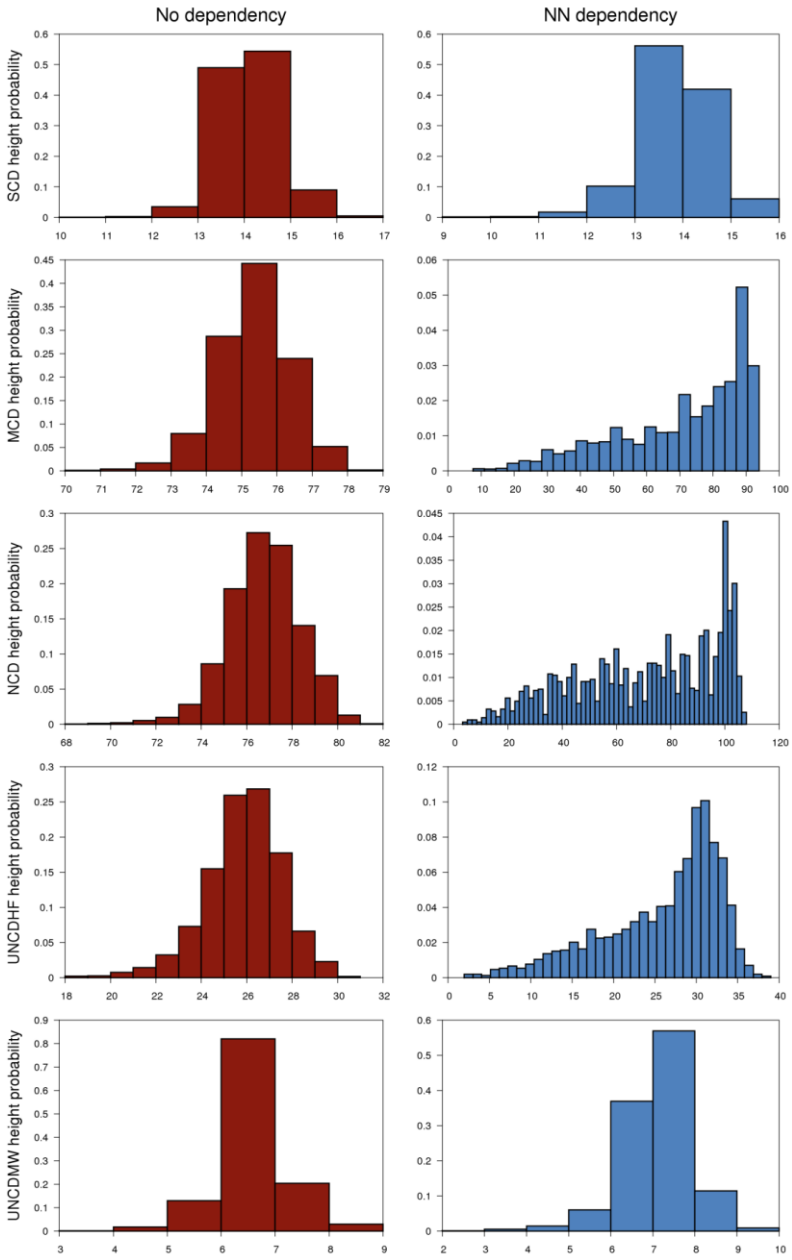

Figure 45-Comparison of the normalised probability distributions of the surface height profiles for the five growth regimes listed in Table 8. The red distributions were produced using a CH_3 adsorption rate constant with no dependency on local structure. The blue set of distributions was produced using the rate constant for CH_3 adsorption with an inversely proportional dependency on the number of nearest neighbours at the adsorbing site.

Table 12-Statistical measures related to the distributions in Figure 45

		No dependency	**NN dependency**
SCD	R_M	15	14
	R_a	14.5984	14.3340
	R_{SD}	0.7068	0.8055
	R_{Sk}	0.0912	-0.5109
	R_{ku}	0.5265	1.6707
MCD	R_M	76	77
	R_a	75.8512	71.6420
	R_{SD}	1.0678	18.8738
	R_{Sk}	-0.3381	-0.8848
	R_{ku}	0.6122	-0.2173
NCD	R_M	77	76
	R_a	77.2400	71.3448
	R_{SD}	1.6285	25.8740
	R_{Sk}	-0.4181	-0.4437
	R_{ku}	0.9796	-0.9538
UNCD(HF)	R_M	26	28
	R_a	26.3688	26.1872
	R_{SD}	1.7158	6.7155
	R_{Sk}	-0.5803	-0.9621
	R_{ku}	1.0779	0.2084
UNCD(MW)	R_M	7	8
	R_a	7.0820	7.6280
	R_{SD}	0.6555	0.8556
	R_{Sk}	0.1099	-0.6981
	R_{ku}	1.8925	2.1793

Surface visualisation

Snapshots of an MCD surface from both the NN dependent (test) adsorption model and one without NN dependency (control) are shown in Figure 47 and Figure 46 respectively. These two snapshots show a distinct difference in surface structure. The surface grown using the control model shows a smaller overall height difference than the other surface, thus leading to a significantly smaller surface roughness. Although the peaks and plateaus are

shorter in the control model they are sharper as evidenced by the positive kurtosis.

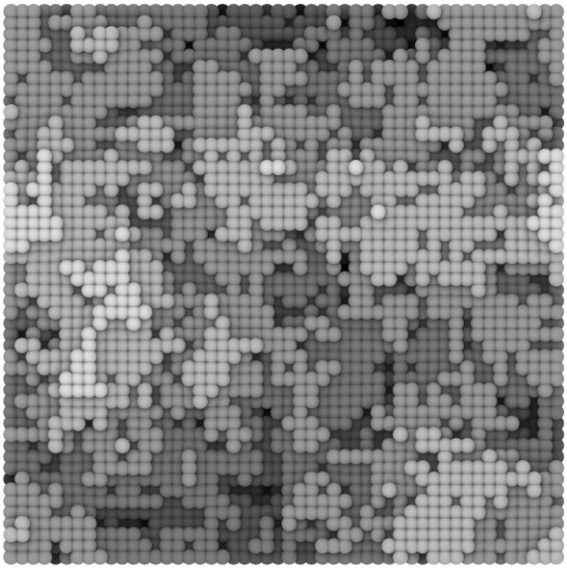

Figure 46-Snapshot of the simulated surface of a CVD diamond grown under MCD conditions with a 50×50 grid using a rate constant for CH_3 adsorption (Equation 3.7) with no dependency on the local structure of the adsorbing site.

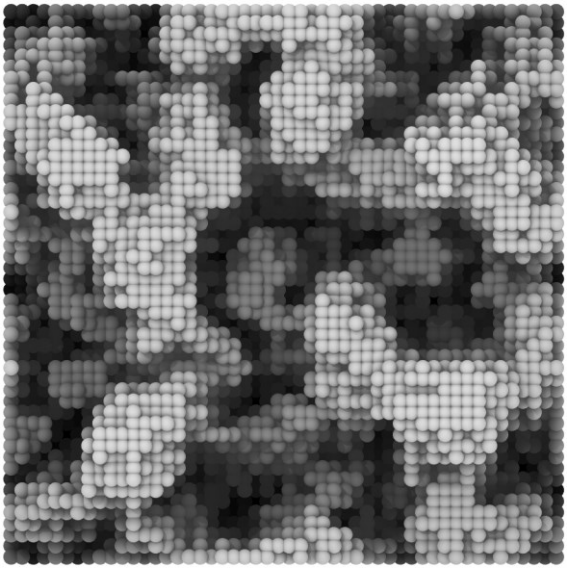

Figure 47-A snapshot of the simulated surface of a CVD diamond grown under MCD conditions with a 50×50 grid, the rate constant for CH_3 adsorption had an inversely proportional relationship with the number of nearest neighbours (Equation 3.7a).

The test model (Figure 47) shows some interesting features not seen in any of the previous models with changes to surface structuring processes. There are well-defined facets, or ridges of plateaus with troughs separating them (the negative R_{ku} value is indicative of this). The surface morphology is similar to polycrystalline diamond grown experimentally and measured by atomic force microscopy (AFM).[16] However a larger KMC unit cell, with a longer simulation time, might be necessary to make a more definite comparison.

These facets are reminiscent of the 'caulliflower' type growth observed in UNCD growth conditions.[17] A visualisation was made of the surface generated using the test model under (HF) UNCD conditions. This snapshot is presented belown in Figure 48 and the small regular facets are clearly visible. If the inter atom distance between two carbon atoms on the (100) surface is taken as 3.57 Å then these facets could represent crystal sizes of approximately 2 nm. This is about half the size of some of the smaller UNCD crystals observed experimentally.[18]

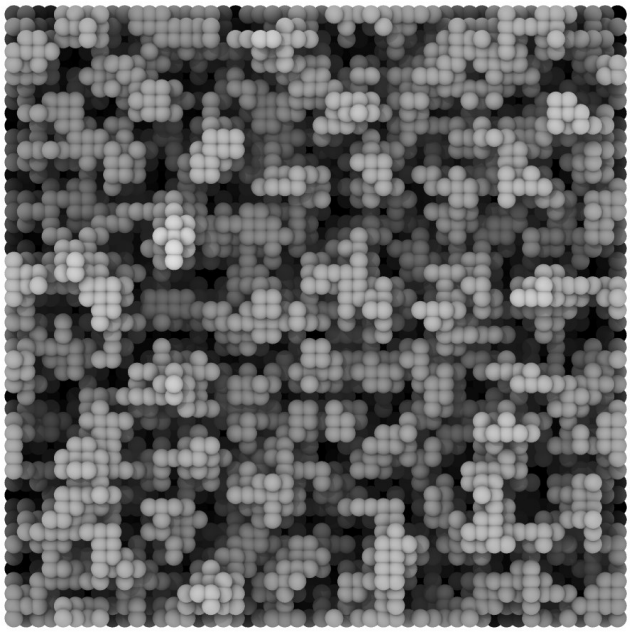

Figure 48-Snapshot of the simulated surface of a CVD diamond grown under (HF) UNCD conditions with a 50×50 grid, using the newer rate constant for CH_3 adsorption from Equation 3.7a.

Critical nucleus

The critical nucleus data for the modified adsorption model is presented in Table 13. It can be seen in these data that the fraction of monomer creation is always higher for the test case (Add), as well as for monomer loss. The fraction of monomer growth however is always less, which makes sense in light of the previous information about monomer loss. The fraction of dimer growth is lower for the test case in all regimes. The critical nucleus still appears to be the dimer, as the fraction of dimer growth is always larger than the fraction of dimer loss. However, there seems to be no apparent pattern in the fraction of dimer loss between the test and base case.

Table 13-Fraction of monomer creation, growth, loss, dimer growth, and loss out of a total possible number of surface restructuring events for the five growth conditions listed in Table 8. The values for the exponential model of etching (Base) and the changed NN dependent adsorption rate constant (Add) are directly compared for each growth regime.

		Monomer creation	**Monomer Growth**	**Monomer Loss**	**Dimer growth**	**Dimer Loss**
SCD	Add	0.93342	0.00064	0.93289	0.00083	0.00012
	Base	0.88411	0.00203	0.88253	0.00258	0.00048
MCD	Add	0.79889	0.00637	0.79382	0.00555	0.00273
	Base	0.70944	0.00915	0.70145	0.00979	0.00241
NCD	Add	0.61965	0.01261	0.60758	0.01221	0.00363
	Base	0.55466	0.01694	0.53763	0.01732	0.00344
UNCD(HF)	Add	0.56343	0.02526	0.53480	0.02725	0.00297
	Base	0.48126	0.03183	0.44397	0.03247	0.00327
UNCD(MW)	Add	0.89806	0.00159	0.89679	0.00151	0.00033
	Base	0.83420	0.00304	0.83147	0.00428	0.00040

4.4. Migration

The model for the migration of an ad-species on the surface has not been changed, but its effect on surface morphology in the Bristol model has not been systematically explored previously. This is discussed in the following section.

4.4.1. Computational detail

It was shown in Chapter 3 that the spatial convergence of the kMC model was good at a 25×25 grid size. In the calculations presented above a 50×50 grid was used for additional spatial accuracy, as surface morphology measurements are more dependent on this. However, for computational efficiency, the calculations that follow were performed on a 25×25 sized grid. This is sufficient for the spatial accuracy required. All of the simulated reactor types from Table 8 were used below. The base/control simulations were the kMC model with the Eyring model of etching with exponential dependence on nearest neighbours. The test simulations in this experiment were the same but with the migration process switched off. The result of these simulations is presented and compared in the next Section.

4.4.2. Results

Surface height distributions

The surface height distributions from the simulations described above are presented in Figure 49. The differences between the base and test simulations are most striking in the cases of SCD and (MW) UNCD growth. This due to these growth regimes being dominated by migration processes. In the SCD example the roughness measure jumps from R_{SD} = 0.71 ML in the control simulation to more than four times that at R_{SD} = 3.93 ML in the test simulation with migration switched off. The roughness value increases for all of the other growth types but not by as great a factor. In fact there is relatively little change in the MCD and (HF) UNCD examples, even though migration does occur with a high frequency in these regimes. This could suggest that etching plays a more significant role of determining the surface structure. In addition, the R_{ku} value for these two simulations indicates that the surfaces, whilst not roughening significantly, do transform from having sharper peaks to more rounded plateaus.

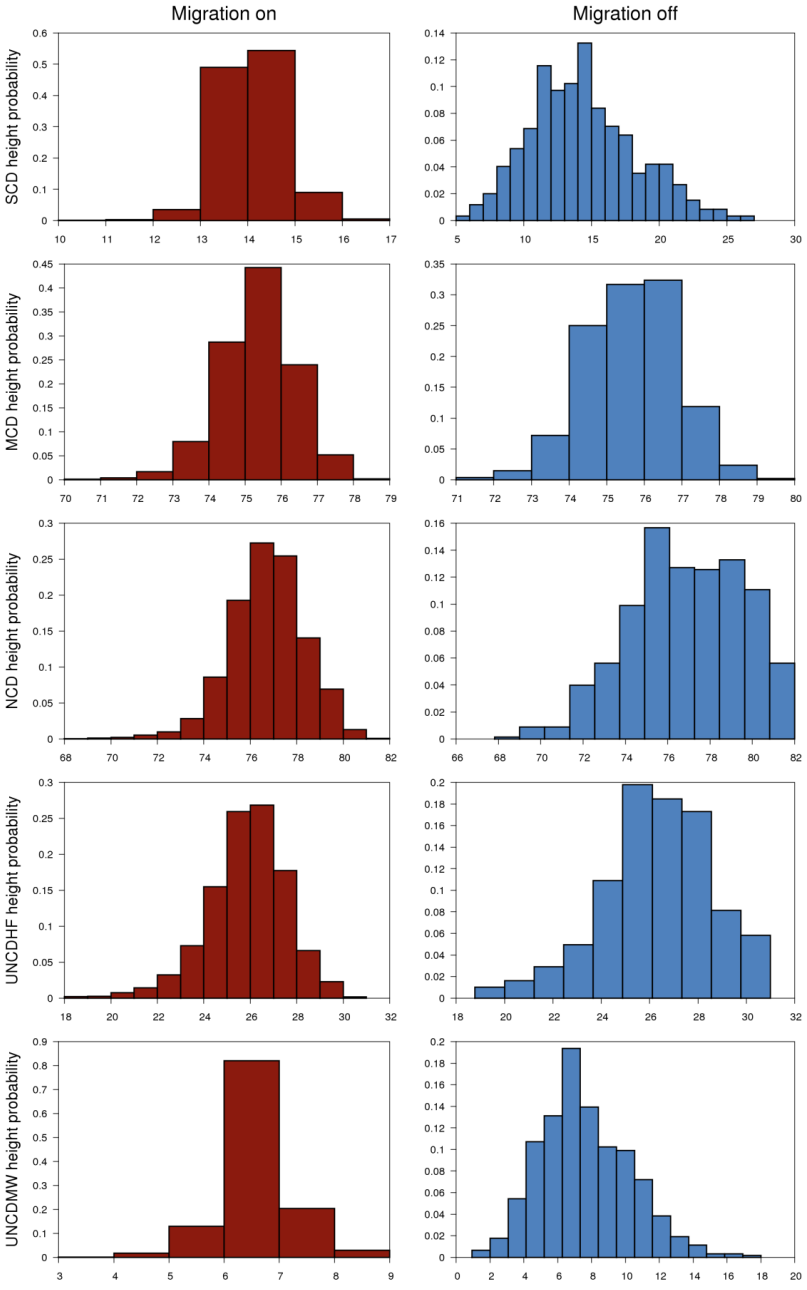

Figure 49-Comparison of the normalised probability distributions of the surface height profiles for the five growth regimes listed in Table 8. The red distributions were base conditions while the blue results have the migration process turned off.

Table 14-Statistical measures related to the distributions in Figure 49.

		Migration on	**Migration off**
SCD	R_M	15	15
	R_a	14.5984	14.8752
	R_{SD}	0.7068	3.9270
	R_{Sk}	0.0912	0.4332
	R_{ku}	0.5265	-0.0928
MCD	R_M	76	76
	R_a	75.8512	76.1664
	R_{SD}	1.0678	1.2411
	R_{Sk}	-0.3381	-0.1368
	R_{ku}	0.6122	-0.0109
NCD	R_M	77	77
	R_a	77.24	77.1856
	R_{SD}	1.6285	2.3236
	R_{Sk}	-0.4181	-0.2506
	R_{ku}	0.9796	-0.3342
UNCD(HF)	R_M	26	27
	R_a	26.3688	26.6608
	R_{SD}	1.7158	1.9075
	R_{Sk}	-0.5803	-0.4476
	R_{ku}	1.0779	0.3972
UNCD(MW)	R_M	7	7
	R_a	7.082	7.7760
	R_{SD}	0.6555	2.5180
	R_{Sk}	0.1099	0.4712
	R_{ku}	1.8925	0.2261

Surface visualisation

The two Figures presented below illustrate the dramatic effect that surface migration of activated ad-species has on the surface morphology of the resultant simulated diamond. Single crystal (SCD) growth was chosen as this is the regime most affected by migration. Figure 50 is the control surface and illustrates smooth terraces growing layer by layer; growth indicative of single crystal, i.e. a new layer does not generally nucleate before the previous layer is ~75% covered.

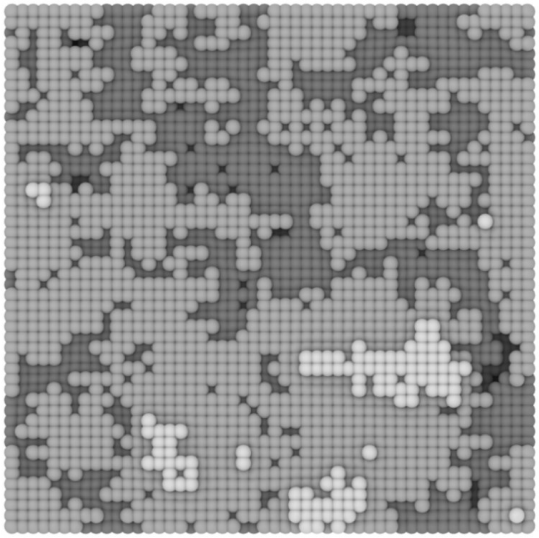

Figure 50-Snapshot of the simulated surface of a CVD diamond grown under SCD conditions with a 50×50 grid, using the new standard model with exponential etching.

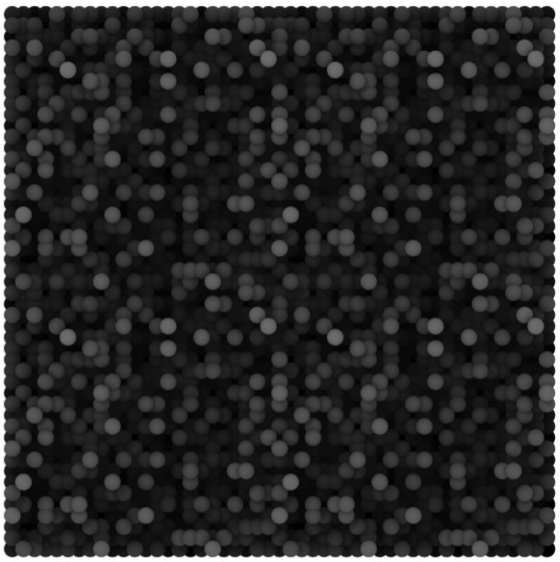

Figure 51-Snapshot of the simulated surface of a CVD diamond grown under SCD conditions with a 25×25 grid (four 25x25 images are shown in this image to make comparison with Figure 50 more straightforward), using the new standard model with exponential etching with ad-species migration turned off.

While Figure 51 was simulated using a 25×25 grid, all of the kMC simulations have periodic boundary conditions. So this Figure is shown containing four replicas of the underlying 25x25 system, to allow one to more easily compare it with the control Figure, which shows a 50x50 grid. Figure 51 shows near stochastic growth, the greyscale illustrating the height of the snapshot looks like a slightly correlated random distribution. The contrast between these two figures plainly shows the importance of surface ad-species migration to SCD growth; it completely changes the morphology of the surface when it is turned off.

Critical nucleus

The results of the critical nucleus analysis of the migration simulations presented in section 4.4.2 are presented in Table 8 below. These results are the first time that the critical nucleus has been smaller than 2 blocks. In the SCD and UNCD (MW) growth systems the fraction of monomer growth is larger than the fraction of monomer loss, meaning that the critical nucleus for both of these regimes is the monomer, 1 block.

Table 15-Fraction of monomer creation, growth, loss, dimer growth, and loss out of a total possible number of surface restructuring events for the five growth conditions listed in Table 8. The values for the exponential model of etching (On) and same model with the migration process deactivated (Off) are directly compared for each growth regime.

		Monomer creation	**Monomer Growth**	**Monomer Loss**	**Dimer growth**	**Dimer Loss**
SCD	On	0.88411	0.00203	0.88253	0.00258	0.00048
	Off	0.2364	0.1361	0.0099	0.0769	0.0004
MCD	On	0.70944	0.00915	0.70145	0.00979	0.00241
	Off	0.7711	0.0990	0.6575	0.0542	0.0442
NCD	On	0.55466	0.01694	0.53763	0.01732	0.00344
	Off	0.4181	0.0921	0.3143	0.0564	0.0263
UNCD(HF)	On	0.48126	0.03183	0.44397	0.03247	0.00327
	Off	0.5038	0.1039	0.3988	0.0603	0.0346
UNCD(MW)	On	0.83420	0.00304	0.83147	0.00428	0.00040
	Off	0.2529	0.1352	0.0108	0.0790	0.0006

It was shown in previous sections that the surface structure of both of these systems depends heavily on surface ad-species migration, so the results here are consistent. For the rest of the growth regimes (MCD, NCD, and UNCD (HF)) the dimer is still the critical nucleus.

4.5. Conclusions

In this chapter the surface morphology of results obtained from the kMC model has been investigated. Three sets of tests for three different surface restructuring processes were implemented in this work. The model of etching a CH_3/CH_2 (bridge) from the surface was the first test. The Eyring model of etching with an exponential dependence on the next nearest neighbours was thus adopted as a part of the standard kMC model. The next test was to take the new standard model and compare it with a model that included an inversely proportional dependence of the next nearest neighbour on the rate constant for CH_3 adsorption. Finally, for completeness, the effect that the migration of surface ad-species had on the morphology of the diamond was tested by comparing simulations from the new standard kMC model with simulations in which the only difference was that the migration process was turned off.

From the results presented in section 4.2, an argument can be made for the etching process causing a general surface roughening. The linear model produces a smoother less peaked surface than the other etching model for growth regimes where etching plays a significant role (MCD, NCD, and UNCD (HF)). This roughening effect, or lack thereof, can also be seen in SCD and UNCD (MW) where etching either has a very minor role or none at all in the case of the exponential model. For these two growth systems the surface roughness clearly decreases when there is little or no etching activity (Figure 40 (d) and Table 9). Evidence contributing to the hypothesis that etching enhances the smoothing of MCD, NCD, and UNCD (HF) growth can be found in Section 4.4.2. With migration turned off, the surface does not get significantly rougher. This means that migration is not a factor in the overall surface structure of the simulated

diamond, leaving only etching as the most important surface restructuring process in this case.

The critical nucleus, the smallest configuration that can nucleate a new layer, was found to be the 2-block dimer in all cases except for SCD and UNCD (MW) growth when migration was turned off; in this case it was the monomer. This is the same size structure that was assumed to be the critical nucleus in the 2-dimensional model. It is possible that the critical nucleus would be larger if there was a more accurate model for **surface species** (not ad-species) etching. Presently an activated surface site can etch at 0.02 % the rate of ad-species etching. The rate constant for surface species etching was changed to equal that of ad-species etching and produced no change to the critical nucleus of two test cases (not reported above). This gives greater confidence in the 2-block result.

4.6. References

(1) Greenwood, J. A.; Williamson, J. B. P. Contact of Nominally Flat Surfaces. *Proc. R. Soc. Lond. Ser. Math. Phys. Sci.* **1966**, *295*, 300–319.

(2) Tayebi, N.; Polycarpou, A. A. Modeling the Effect of Skewness and Kurtosis on the Static Friction Coefficient of Rough Surfaces. *Tribol. Int.* **2004**, *37*, 491–505.

(3) Jesus, M.; Yebra-Pimentel, E. Hydrogel Contact Lenses Surface Roughness and Bacterial Adhesion. In *Ocular Diseases*; Adio, A., Ed.; InTech, 2012.

(4) Butler, J. E.; Oleynik, I. A Mechanism for Crystal Twinning in the Growth of Diamond by Chemical Vapour Deposition. *Philos. Trans. R. Soc. Math. Phys. Eng. Sci.* **2008**, *366*, 295–311.

(5) May, P. W.; Allan, N. L.; Ashfold, M. N. R.; Richley, J. C.; Mankelevich, Y. A. Simplified Monte Carlo Simulations of Chemical Vapour Deposition Diamond Growth. *J. Phys. Condens. Matter* **2009**, *21*, 364203.

(6) May, P. W.; Harvey, J. N.; Allan, N. L.; Richley, J. C.; Mankelevich, Y. A. Simulations of CVD Diamond Film Growth Using a Simplified Monte Carlo Model. In *Symposium J – Diamond Electronics and Bioelectronics-Fundamentals to Applications III*; MRS Online Proceedings Library; 2009; Vol. 1203.

(7) May, P. W.; Allan, N. L.; Ashfold, M. N. R.; Richley, J. C.; Mankelevich, Y. A. Simulations of Polycrystalline CVD Diamond Film Growth Using a Simplified Monte Carlo Model. *Diam. Relat. Mater.* **2010**, *19*, 389–396.

(8) May, P. W.; Harvey, J. N.; Allan, N. L.; Richley, J. C.; Mankelevich, Y. A. Simulations of Chemical Vapor Deposition Diamond Film Growth Using a Kinetic Monte Carlo Model. *J. Appl. Phys.* **2010**, *108*, 014905.

(9) May, P. W.; Harvey, J. N.; Allan, N. L.; Richley, J. C.; Mankelevich, Y. A. Simulations of Chemical Vapor Deposition Diamond Film Growth Using a Kinetic Monte Carlo Model and Two-Dimensional Models of Microwave Plasma and Hot Filament Chemical Vapor Deposition Reactors. *J. Appl. Phys.* **2010**, *108*, 114909.

(10) Rawles, R. E.; Komarov, S. F.; Gat, R.; Morris, W. G.; Hudson, J. B.; D'Evelyn, M. P. Mechanism of Surface Smoothing of Diamond by a Hydrogen Plasma. *Diam. Relat. Mater.* **1997**, *6*, 791–795.

(11) Stallcup, R. E.; Perez, J. M. Scanning Tunneling Microscopy Studies of Temperature-Dependent Etching of Diamond (100) by Atomic Hydrogen. *Phys. Rev. Lett.* **2001**, *86*, 3368–3371.

(12) Netto, A.; Frenklach, M. Kinetic Monte Carlo Simulations of CVD Diamond growth—Interlay among Growth, Etching, and Migration. *Diam. Relat. Mater.* **2005**, *14*, 1630–1646.

(13) Skokov, S.; Weiner, B.; Frenklach, M. Elementary Reaction Mechanism for Growth of Diamond (100) Surfaces from Methyl Radicals. *J. Phys. Chem.* **1994**, *98*, 7073–7082.

(14) May, P. W.; Mankelevich, Y. A. From Ultrananocrystalline Diamond to Single Crystal Diamond Growth in Hot Filament and Microwave Plasma-

Enhanced CVD Reactors: A Unified Model for Growth Rates and Grain Sizes. *J. Phys. Chem. C* **2008**, *112*, 12432–12441.
(15) May, P. W. Personal Communication.
(16) Shen, B.; Sun, F. Effect of Surface Morphology on the Frictional Behaviour of Hot Filament Chemical Vapour Deposition Diamond Films. *Proc. Inst. Mech. Eng. Part J J. Eng. Tribol.* **2009**, *223*, 1049–1058.
(17) May, P. W.; Mankelevich, Y. A. Experiment and Modeling of the Deposition of Ultrananocrystalline Diamond Films Using Hot Filament Chemical Vapor Deposition and Ar/CH4/H2 Gas Mixtures: A Generalized Mechanism for Ultrananocrystalline Diamond Growth. *J. Appl. Phys.* **2006**, *100*, 024301.
(18) Wang, C.-S.; Tong, G.-H.; Chen, H.-C.; Shih, W.-C.; Lin, I.-N. Effect of N2 Addition in Ar Plasma on the Development of Microstructure of Ultra-Nanocrystalline Diamond Films. *Diam. Relat. Mater.* **2010**, *19*, 147–152.

Chapter 5

Studies of methyl desorption from an H-terminated (2x1):{100} diamond surface

In this chapter computational studies of desorption of a pendant methyl (CH_3) from the {100} surface of CVD diamond are presented. The work in this chapter has been modified from a manuscript in preparation containing work carried out by the candidate together with collaborators. At appropriate points in the chapter below, work carried out by others is clearly identified. Some of this work has been published in Phil. Trans. Royal Society A. [1]

5.1. Introduction

The growth of chemical vapour deposition (CVD) diamond is a competition between two complex sets of processes, the adsorption and incorporation of carbon into the growing lattice, and the removal of carbon on the surface back to the gas phase[2–5]. The mechanism by which an sp^3 hybridised carbon bonded to the growing surface is lost to the gas phase medium above it is not fully understood. It has been shown[6] that the etching of carbon species from the growing CVD diamond surface occurs in atmospheres of atomic $H^{\cdot}$. For example, it has been found that under CVD conditions using an H_2 microwave plasma with CH4 present produces SCD diamond growth. However, when the CH4 process gas is removed from the reaction with the SCD diamond in-situ, the etching of carbon is observed[3].

The most obvious mechanism for etching is the spontaneous thermal dissociation of the C_d-CH_3 bond. This has been suggested as a possible route to carbon loss from the growing surface, but recent computational studies suggest that the energy barrier of the reaction is too high to explain the experimentally observed rates. [7] Another proposed route to methyl loss would require a consideration of the non-equilibrium dynamics at the growing surface, which with the constant supply of excess energy is inherently out of equilibrium although in a steady state. The putative mechanism, shown in Figure 52, involves a 'dangling' surface radical CH_2 to which an H atom combines. This exothermic reaction produces an energetically 'hot', with an excess amount of energy in the range of approximately 100 kcal mol^{-1}, CH_3 on the surface (C_d-CH_3*). Within this hotspot it is possible for this excess energy to break the C_d-CH_3* bond (Reaction R1a) before it has a chance to be dissipated through the bulk diamond. This mechanism has not been seriously considered previously due to diamond's high thermal conductivity. However, it is the purpose of this study to look at the behaviour of these nascent 'hotspots' on time scales long before thermal equilibrium can occur.

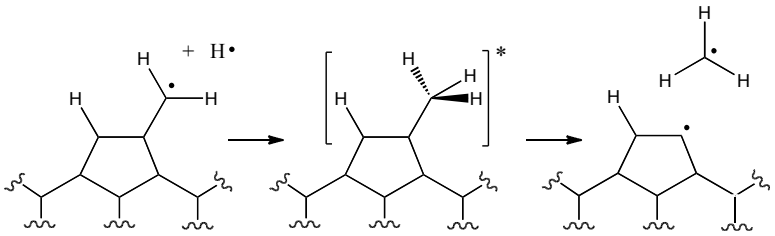

Figure 52-Reaction scheme showing non-equilibrium dissociation of a CH_3 from the diamond surface due to the excess energy gained from the CH_2· + H· reaction breaking the C_d-CH_3 bond before it can dissipate through the diamond bulk.

The aim of the work presented in this chapter is to look at both the non-equilibrium dissociation of the CH_3 group from the surface and the thermodynamics of the Cd-CH_3 bond using an empirical valence bond (EVB) potential energy surface fitted to CASPT2 and CCSD(T) electronic structure theory.

$$C_d\text{-}CH3^* \longrightarrow C_d\cdot + CH_3(g)\cdot \qquad \text{(R1a)}$$

C_d-CH3* $\rightarrow C_d$-CH3 (R1b)

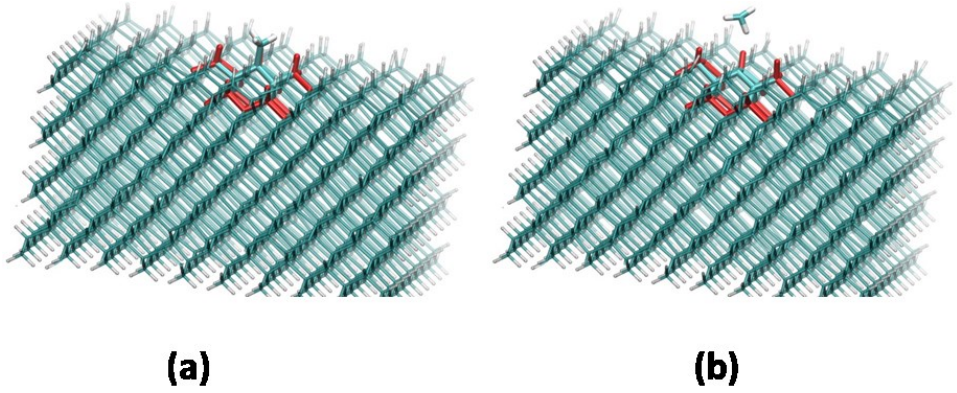

Figure 53-Molecular model used for all MD simulations, comprising 2090 atoms ($C_{1498}H_{592}$)

5.2. Methods

The general theory of molecular mechanics (MM), molecular dynamics (MD), and quantum mechanics (QM) was introduced in Chapter 2. All of the molecular mechanics calculations reported in this chapter were performed in a locally modified version of the CHARMM (Chemistry at HARvard Macromolecular Mechanics) software.[8] All density functional theory results reported here were obtained using the Gaussian 09 suite of programs[9] and the post-SCF and multireference calculations were done with the MOLPRO suite of software[10,11].

In this section the more specific theory of the method used to create a reactive potential energy surface (PES) for molecular dynamics simulations is discussed. An analytic potential is fitted to accurate electronic structure data. The electronic structure calculations described here have been performed by Professor Jeremey Harvey. They are reported here due to the integral part they play in fitting an analytical reactive PES. Therefore, the basic theory for these calculations will only be discussed only briefly.

5.2.1. Analytical reactive potential energy surface

Molecular mechanics typically approximate the potential energy arising from covalent bonding of atoms as a harmonic spring (Chapter 2). In this framework, there is no way to treat the breaking of covalent bonds on the potential surface in this harmonic approximation. There are methods that can create a reactive potential energy surface (PES) using force fields and electronic structure methods on the fly with *ab initio* molecular dynamics methods[12]. These methods take advantage of the computational efficiency of force field molecular mechanics but use *ab initio* electronic structure methods when it becomes necessary to treat the electron more accurately, e.g. during a chemical reaction. While being at the cutting edge of computational chemistry these methods are still computationally extremely expensive when long simulation periods are involved.

This study has used the empirical valence bond (EVB) method[13–15] to produce an analytical reactive PES. EVB is a subset of other analytical methods available to create reactive potentials, a review of these can be found in textbooks[12] or in the literature[15,16]. The EVB method can create an approximate *adiabatic* surface from two or more different *diabatic* potential energy surfaces. This is described more explicitly in a generalisation of this approach by Truhlar et al as the Multiconfigurations molecular mechanics (MCMM) algorithm[17]. In the MCMM method, the analytical surface is fitted to accurate electronic structure data from a reaction scan (for example). The approach used in this work is similar to that used by Chang and Miller[18] and is described briefly below.

The coordinate dependent Hamiltonian is represented by an n × n matrix (Equation 1) where each of the diagonal elements, $V_n(\mathbf{q})$, corresponds to the molecular mechanics energy that would be obtained for a particular bonding pattern of atoms (e.g. reactant- or product-like) at the structure considered. The parameters ε_i are offset values required to introduce the correct relative energy for equilibrium structures of the different molecular mechanics forcefields.

$$\mathbf{H}(\mathbf{q}) = \begin{bmatrix} V_1(\mathbf{q}) + \epsilon_1 & \dots & H_{1n}(\mathbf{q}) \\ \vdots & \ddots & \vdots \\ H_{n1}(\mathbf{q}) & \dots & V_n(\mathbf{q}) + \epsilon_n \end{bmatrix} \quad (1)$$

The off diagonal elements, $H_{ij}(\mathbf{q})$, are the fitting functions and are in the form of a Gaussian function. The overall EVB energy is obtained as the lowest energy eigenvalue of the pseudo-Hamiltonian matrix. As solving (Equation 1) explicitly for a 2×2 matrix is part of results section 5.3.2 the discussion of a general solution is forgone in this section. For a general solution see Glowacki, Orr-Ewing, and Harvey above.

5.2.2. Boxed molecular dynamics

A recently developed method for accelerating rare events in molecular dynamics simulations[19,20] was used to calculate the free energy profile for spontaneous thermal desorption of CH_3 from the 2x1 {100} surface of diamond at temperatures found in a CVD reactor. This method is a generalised version of accelerated molecular dynamics called boxed molecular dynamics (BXD). In this method, a reaction coordinate ρ is divided into multiple boxes to which the molecular dynamics simulation is constrained. The relationship between the normalised probability distribution of the reaction coordinate and the Gibbs free energy of a system is described by Equation 2. A schematic diagram of the BXD procedure for a model reaction coordinate is shown in fig. 4. In this model system a trajectory is shown in box *m*. The MD system progresses as normal except for the monitoring of the atoms associated with the reaction coordinate. If at time *t*+*dt* any of these atoms exceed the constraint, then the simulation is reverted to time *t*. At this point only the atoms affecting the constrained coordinate are subjected to a velocity inversion procedure during which all conserved quantities of the equations of motion are preserved.

$$p(\rho) = \frac{\exp(-\frac{G(\rho)}{kT})}{\int \exp(-\frac{G(\rho)}{kT}) d\rho} \quad (2)$$

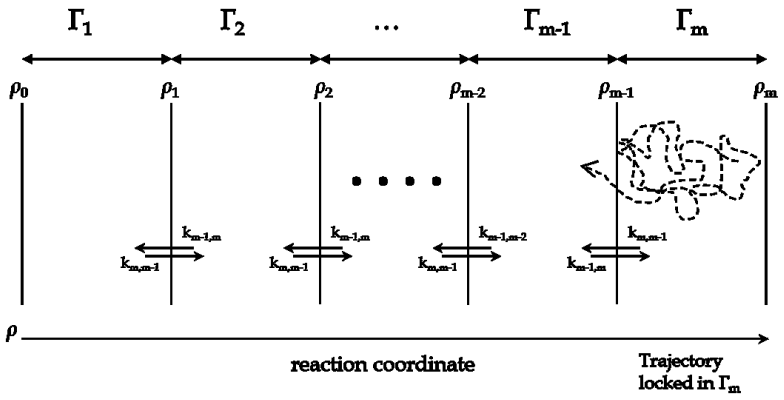

Figure 54- Diagram of a BXD procedure for a simplified example reaction coordinate divided into m boxes. In this picture the trajectory exits box m after two inversions at the ρ_{m-1} boundary. Rate constants $k_{a,b}$ are determined by the number of inversions at each boundary. (Schematic diagram adapted from references)[19,20]

In Figure 4 above the example trajectory is allowed to pass from box m to box *m-1* after two velocity inversions against constraint ρ_{m-1}. This is similar for a real case; the reaction coordinate is constrained in a box for a certain simulation time until an arbitrary number of velocity inversions have occurred. However, unlike the toy example above, the simulation must reside in a particular constrained box until many velocity inversions occur. This is to ensure that the phase space of the reaction coordinate in question is statistically well sampled. Counting the number of inversion events with respect to the total residence time in each box allows a set of transition rate coefficients, $k_{a,b}$, to be determined.

Generalising from box m (Figure 54) bounded by ρ_m and ρ_{m-1}, the transition rate coefficient from box m to $m-1$ is defined by Equation 2 where $h_{m,m-1}$ is the number of velocity inversions on boundary ρ_{m-1} and t_m is the lifetime of the trajectory in box m.

$$k_{m,m-1} = \frac{h_{m,m-1}}{t_m} \tag{3}$$

Going to the next box, *m-1*, we can calculate the transition rate coefficient from box *m-1* back to box *m* or to box *m-2* in the same manner (Equations 4 and 5).

$$k_{m-1,m} = \frac{h_{m-1,m}}{t_{m-1}} \tag{4}$$

$$k_{m-1,m-2} = \frac{h_{m-1,m-2}}{t_{m-1}} \tag{5}$$

The equilibrium constant describing the equilibrium relative populations in two boxes *n* and *n-1* can be defined as Equation 5 as long as temperature is defined.

$$K_{n-1,n} = \frac{k_{n-1,n}}{k_{n,n-1}} = \exp\left(-\frac{\Delta \mathrm{G}_{n-1,n}}{k_B T}\right) \tag{6}$$

Thus the free energy of each discrete box is described and can be found by rearranging Equation 5 against some arbitrary reference value. And this free energy, the discrete probability of residing in box *n* is given by Equation 6.

$$p_n = \frac{1}{\sum_n \exp\left(-\frac{\Delta G_n}{kT}\right)} \exp\left(-\frac{\Delta G_n}{kT}\right) \tag{7}$$

A detailed derivation of the boxed molecular dynamics method can be found in the papers cited above and their supplementary information.

5.3. Results

5.3.1. Electronic structure calculations

An important component of the study featured in this chapter is the calculation of an accurate potential energy curve for the bond dissociation reaction (R1a). The following ab-initio calculations were performed by Professor Jeremy Harvey. They are described here as they are an integral part of the

calculations reported in the rest of this chapter. The problem of producing the potential energy curve of reaction R1a is addressed by using a hierarchy of methods and models beginning with our most simplified model of the related dissociation of CH_3 from neopentane (R2). A visualisation of the product and reactant for this reaction is shown in Figure 55.

$$H_3C\text{-}C(CH_3)_3 \longrightarrow H_3C^{\cdot} + C(CH_3)_3^{\cdot} \qquad \text{(R2)}$$

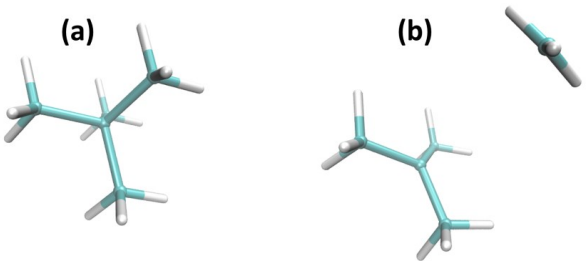

Figure 55-Molecular model of reaction R2, (a) shows the reactant neopentane and (b) shows the products, methyl + t-butyl

The experimental values for the enthalpy of formation at 298 K for neopentane and the products of reaction R2 were obtained from the NIST web book[21]. The enthalpy of formation for neopentane, methyl, and t-butyl are -40.14±015, 34.821, and 11±0.7 kcal mol^{-1}. These give an enthalpy for bond dissociation of 86.0±0.8 kcal mol^{-1}. DFT calculations at the B3LYP/6-311G(d) level of theory, and ideal gas rigid rotor harmonic oscillator statistical mechanics, predict a bond dissociation energy at 0 K which is 1.77 kcal mol^{-1} less than the dissociation enthalpy at 298 K. Thus the experimental value of the bond dissociation energy at 0 K is taken to be 84.2 kcal mol^{-1}. Bond energies were calculated with a number of methods at different levels of theory; these values (as well as for the $(H_3C)_3CCH_2$-H bond) are shown in Table 16 below. The best value for the C-C bond dissociation energy was calculated at the CCSD(T)-F12 level of theory, this was 85.4 kcal mol^{-1} and in good agreement with the experimental value.

Table 16-Calculated neopentane C-C(and C-H) bond dissociation energy, BDE, (kcal mol^{-1})

	Relaxed geometries [a]		Rigid geometries [b]	Relaxed [a]
	[c] BDE_0(C–C)	[d] BDE(C–C)	[c] BDE(C–C)	[d] BDE(C–H)
B3LYP/6-311g*	84.5	76.1	102.4	98.0
B3LYP-D3/6-311G*	88.4	80.1	N/A	98.7
MP2-F12/aug-cc-pVTZ [f]	99.0	90.6	116.7	100.5
CCSD-F12/aug-cc-pVTZ [f]	90.7	82.4	108.0	99.6
CCSD(T)-F12/aug-cc-pVTZ [f]	93.7	85.4	110.7	100.5
CASSCF/cc-pVTZ	75.7 [e]	67.3 [e]	91.0 [e]	N/A
CASPT2/cc-pVTZ	90.3 [e]	82.0 [e]	108.1 [e]	N/A

[a] Energies obtained using the indicated method at the structures optimized with B3LYP. [b] Energies obtained using the indicated method, and with fragment structures corresponding to those predicted with B3LYP for the neopentane minimum using CASPT2 rigid scan geometries at fragment separtation of 10 Å. [c] Energies do not include zero point energy corrections. [d] Energies include B3LYP/6-311g* zero-point energy corrections of -8.3 kcal mol^{-1}. [e] Dissociation limiting energies calculated for the supermolecule with $r_{c\text{-}c}$ = 10 Å. [f] The normal cc-pVTZ basis set was used on hydrogen.

A set of scans along the C-C dissociation coordinate (Figure 56) were also calculated as well as the single point energy calculations shown above. The use of multireference methods was required for an accurate treatment of the wavefunction along the reaction coordinate as neopentane dissociation results in a singlet diradical at long separations. Our approach was to carry out both CASSCF(2,2)/cc-pVTZ and CASPT2(2,2)/cc-pVTZ energy calculations in which the 2 electron, 2 orbital active space was chosen to correspond to the singly occupied p orbital localized on each carbon during dissociation. Figure 56a shows CASPT2 and CASSCF results obtained at structures derived from relaxed B3LYP/6-311G(d) scans along the C–C reaction coordinate constrained to a C3v symmetry, and Table 1 shows the CASSCF and CASPT2 results at infinite separations (taken at rCC = 10 Å), using the B3LYP optimized geometries. Note that the B3LYP calculations involved careful testing for a broken-symmetry unrestricted solution at each bond length, with the closed-shell solution found to be more stable until rCC = 2.4 Å. The expectation value for the S^2 operator for the Kohn-Sham orbitals then increases rapidly from 0.19 at rCC = 2.6 Å to 0.92 at rCC = 3.4 Å. It should also be noted that the CASSCF and CASPT2 curves show no barrier to dissociation in excess of the endothermicity.

Encouragingly, the zero point-corrected CASPT2 bond dissociation energy of 82.0 kcal mol^{-1} is in excellent agreement with both experiment and the

CCSD(T)-F12 bond dissociation energy. Figure 1b is the same as Figure 56a, with the only difference being that the results shown have been obtained using rigid C3V CASSCF and CASPT2 scans along the C–C dissociation coordinate of neopentane, where the starting structure was the optimized B3LYP structure for neopentane. At large separations, the energies shown in Fig 1b are larger than those shown in Fig 1a, as the forming methyl and t-butyl radicals are now not allowed to relax to their optimum structure. For example, the CASPT2 rigid scan bond dissociation energy (taken as the potential energy for rCC = 10 Å) is 108.1 kcal mol-1, which is 17.8 kcal mol^{-1} larger than the energy obtained using B3LYP optimized geometries (i.e., a relaxed scan). Table 1 shows that the BDEs computed without fragment relaxation are all ca. 18 kcal mol–1 greater than the relaxed bond energies.

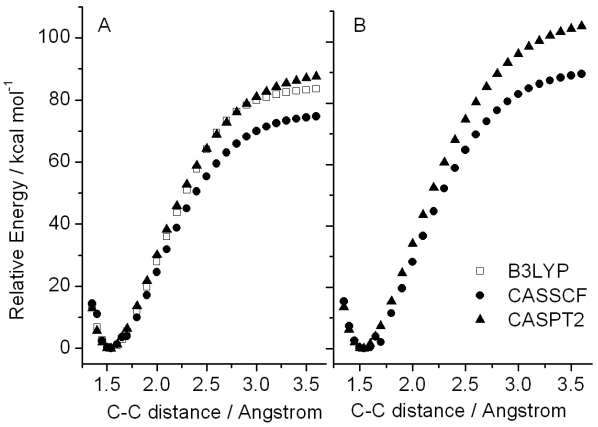

Figure 56-Electronic structure scans along the neopentane CH_3 dissociation reaction coordinate.

As discussed below, the neopentane dissociation data in Table 1 and Figure 1 were used to fit an analytical potential energy surface model to accurately represent (R2a); however, in order to understand whether the total system size had an impact on the calculated CC dissociation energy, we performed additional calculations using a series of incrementally larger diamond proxy models, the sequence of which is shown in Figure 57. C–CH_3 and H_2C–H bond

dissociation energies were calculated for each of these, using the B3LYP-D3 level of theory, and these are shown in Table 2.

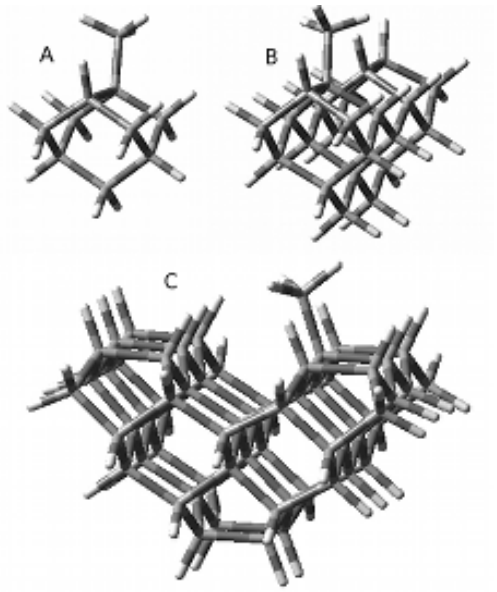

Figure 57-progressively larger cluster models used to in the DFT calculations presented in the table below.

Table 17: Bond dissociation energies, BDE, (kcal mol^{-1}) obtained for the diamond proxy models shown in Figure 57, at the B3LYP/6-311G(d) and B3LYP-D3/6-311G(d) levels of theory, at the B3LYP/6-31G(d) optimized structures, and including B3LYP/6-31G(d) zero-point energy correction

	B3LYP		B3LYP-D3	
	BDE(C–C)	BDE(C–H)	BDE(C–C)	BDE(C–H)
Model A	87.1	96.4	90.8	97.1
Model B	77.1	90.5	82.4	91.1
Model C	73.6	90.8	81.3	91.8

As can be seen in Table 16, the smaller model A leads to an overestimate of the C–CH_3 and –CH_2–H bond dissociation energies at the diamond [100] surface, due to the lack of steric hindrance from the environment. Models B and especially C should be close to the surface limit in this respect, and the calculated B3LYP-D3 bond energies appear to be reasonably well converged with respect to system size. Note that the B3LYP bond energies are smaller, especially for BDE(C–C), due to the neglect of the attractive dispersive interactions between the

methyl radical and the surface. The same effect can be seen for the C–C bond energy in neopentane in Table 16. It can also be seen there that the B3LYP-D3 bond energy is smaller than experiment and than the CCSD(T)-F12 values, which agree well. Assuming that a similar underestimate occurs at the diamond [100] surface, the best estimates of the surface BDE(C–C) and BDE(C–H), based on the model C B3LYP-D3 value, and the difference between the B3LYP-D3 and CCSD(T)-F12 values for neopentane, are respectively of 86.6 and 93.6 kcal/mol.

5.3.2. Fitting the EVB potential

As the intent of this study was to investigate the non-equilibrium kinetic behaviour of the reaction in Figure 52, it was necessary to probe the dynamics of this reaction. Studying reactions on the diamond surface with a realistic model would be computationally intractable using ab-initio methods such as direct dynamics. Hybrid methods such as combined quantum mechanical and molecular mechanical (QM/MM) approaches can be used for optimizations and energy calculations[7,22–25] but are likewise computationally too demanding for carrying out dynamical studies. We have chosen to use an empirical valence bond (EVB) approach similar to the method developed by Warshel and Weiss.[13] The method was implemented in a locally modified version of the CHARMM molecular dynamics software,[8] and is described in detail elsewhere.[15]

The potential was obtained in an analytical form which was fitted to a modified version of the CASPT2 electronic structure theory results described above. The CASPT2 method returns a relative energy at large C-C distance that is slightly smaller than the best estimate of the bond energy, as shown in Table 16. Also, the CASPT2 energies along the dissociation curve cannot readily be corrected for zero-point energy. Accordingly, the CASPT2 energies (relative to that obtained at the neopentane minimum) computed for a set of n C–C distances r_i were scaled by a factor $f = D_0(\text{CCSD(T)})/D_e(\text{CASPT2})$, where D_0(CCSD(T)) is 85.4 kcal mol^{-1}, the zero-point energy-corrected bond energy computed using CCSD(T)-F12, and D_e(CASPT2) is 90.3 kcal mol^{-1}, the bond energy calculated

using CASPT2 without zero-point correction. This yields a set of relative energies $\Delta E_{\text{ab initio}}(r_i)$, which is shown below in Table 18.

Table 18-CCSD(T) corrected CASPT2 scan energies for the C – C bond in $H_3C-C(CH_3)_3$

$r_{c\text{-}c}$	Energy / kcal mol^{-1}
1.4	5.36
1.5	0.16
1.6	1.27
1.7	6.01
1.8	12.82
1.9	20.52
2.0	28.42
2.1	36.09
2.2	43.26
2.3	49.78
2.4	55.60
2.5	60.72
2.6	65.06
2.7	68.74
2.8	71.82
2.9	74.37
3.0	76.46
3.1	78.15
3.2	79.52
3.3	80.62
3.4	81.50
3.5	82.22
3.6	82.79

The analytical form of the potential energy for a given set of nuclear coordinates was obtained as the lowest eigenvalue λ_0 of a pseudo-Hamiltonian matrix (equation (2)). The diagonal elements of this matrix are obtained from the

Merck molecular mechanics force field (MMFF94)[26] $V(\mathbf{q})$ using appropriate bonding terms for the bound and unbound states.

$$H(\mathbf{q}) = \begin{bmatrix} V_1(\mathbf{q}) + \varepsilon_1 & H_{12}(\mathbf{q}) \\ H_{12}(\mathbf{q}) & V_2(\mathbf{q}) + \varepsilon_2 \end{bmatrix} \tag{8}$$

The diagonal elements $V_j(\mathbf{q})$ are molecular mechanics energies obtained at a given structure using the product and reactant connectivities and forcefields. The role of the energy offsets ε_j (which do not depend on $\mathbf{q}$) is to correctly describe the electronic energy difference between reactant and product states. In the case that the respective coupling elements, $H_{12}(\mathbf{q}=\text{P})$ and $H_{12}(\mathbf{q}=\text{R})$, are close to zero near the product and reactant geometries, then the reaction energy is $(V_2(\mathbf{q}=\text{P}) + \varepsilon_2) - (V_1(\mathbf{q}=\text{R}) + \varepsilon_1)$. Off diagonal elements $\mathbf{H}_{12}(\mathbf{q})$ are represented by a linear combination of N Gaussian functions of the C–C atom-atom distance r for the breaking bond, of the form

$$H_{12}(r) = \sum_{k=1}^{N} A_k \exp\left(-\frac{1}{2}((r - B_k)/C_k)^2 \right) \tag{9}$$

where A_k, B_k, and C_k are the respective amplitude, center, and width parameters for a particular Gaussian function. In the present case, the potential was fit to the electronic structure data mentioned earlier using a combination of two Gaussian functions for the off-diagonal term (i.e. N = 2 in eq. (9)). The fit was chosen to minimize the least squares metric of equation 10:

$$\chi^2(A_k, B_k, C_k; 1 \le k \le N) = \sum_i \left[\lambda_0(r_i) - (\Delta E_{abinitio}(r_i)) \right]^2 \tag{10}$$

In this expression, $\lambda_0(r_i)$ is the optimized value of the lowest eigenvalue of the matrix of eq. (1), with the C–C distance r constrained to the appropriate value r_i, but with all other structural parameters optimized. The value of the offset ε_1 was chosen such that $V_1 + \varepsilon_1$ is equal to zero at the minimum of the potential energy curve. The offset ε_1 was chosen such that $V_2 + \varepsilon_2$ is equal to the ab initio dissociation energy at large r.

Table 19-Optimized parameters for the Gaussian functions making up H 12 in Eq. (3)

Gaussian	A (amplitude)	B (center)	C (width)
1	38.35	2.32	0.27
2	133.34	2.95	0.44

The best fit parameters for each Gaussian are shown in Table 19 above. All of the functions involved in the fitting procedure are shown in Figure 58. The value of $H_{12}(\mathbf{q})$ is close to zero at 1.54 Å and beyond 4.5 Å so that the potential is described by $V_1(\mathbf{q})$ and $V_2(\mathbf{q})$ in the reactant and product regions.

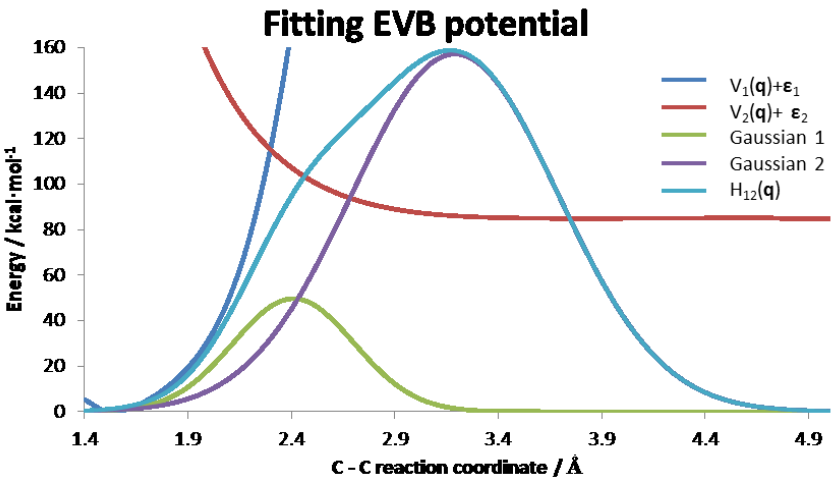

Figure 58-MMFF94 energies for the reactant ($V_1(q)$-bonded state) and product ($V_2(q)$-dissociated state) geometries with the off diagonal Gaussian functions with the parameters from Table 19.

A plot of the fitted λ_0 and $\Delta E_{\text{ab initio}}$ (Table 18) as a function of $r_{c\text{-}c}$ is shown in Figure 59a. The values of λ_0 are obtained by performing a relaxed MM scan using the EVB potential described by the parameters in Table 19 and the text above at the same values of $r_{c\text{-}c}$ as there are points of data in $\Delta E_{\text{ab initio}}$.

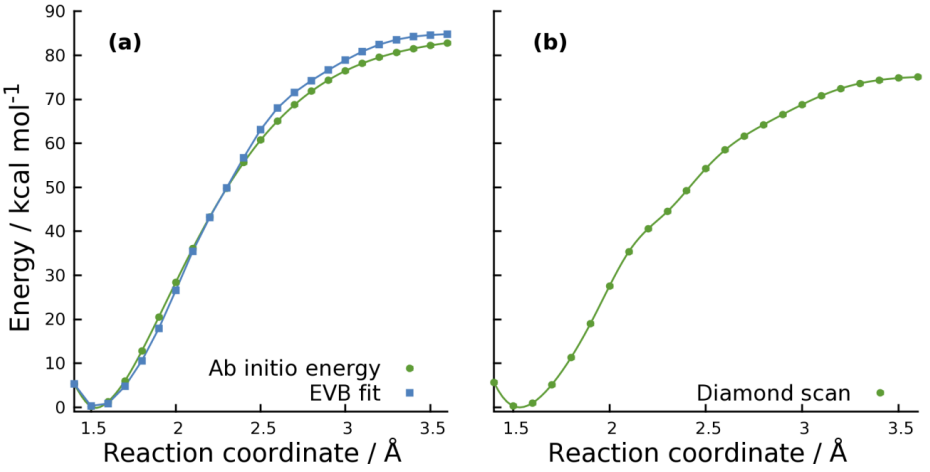

Figure 59- Final EVB fit for neopentane compared with the CASPT2 scaled CCSD(T) scan data (a) alongside a relaxed EVB scan of methyl dissociation for the diamond surface using a modified set of EVB parameters obtained from the fit with neopentane (b)

Due to the difficulty of calculating *ab initio* values for the potential energy curve for CH_3 dissociation from a large diamond surface (Figure 53), the EVB potential for the diamond model was generated directly from that fitted to *ab initio* data in the case of neopentane as shown in Figure 59a. The H_{12} function was used completely unmodified. The offset parameters ε_1 and ε_2 were chosen, as with neopentane, so that $V_1 + \varepsilon_1$ is equal to zero and $V_2 + \varepsilon_2$ equal the dissociation energy of diamond at large r. A relaxed EVB scan of the C-C reaction coordinate for the diamond model is shown in Figure 59b. This potential has an asymptotic value of λ_0 for large r of ca. 75.4 kcal mol^{-1}, somewhat smaller than the *ab initio* calculations in Table 17. A relaxed scan of a methyl dissociation from the diamond surface using the EVB potential just discussed is shown in Figure 59b.

Comment [JNH1]: Defined how? We had two approaches here: In one, we kept eps1- eps2 the same as for neopentane. That was the original and main one – but the words highlighted here do not describe that option well. The other option was chosen to reproduce the 'best' diamond surface BDE. I believe you were planning not to "go there" in your thesis (which is fine).

Comment [JNH2]: Needs to be deleted I think?

5.3.3. Non-equilibrium dynamics

The following MD simulations were performed to investigate the non-equilibrium behaviour of the reaction shown in Figure 52. The presence of a locally 'hot' methyl surface species as a result of this reaction needed to be accurately represented in order to capture correct dynamics of the system. In order to do this, a certain amount of kinetic energy was added to an H atom on the methyl in the direction of the H-C bond before the beginning of each NVE trajectory. This energy would then either propagate through the lattice equalising with the average temperature very rapidly due to the thermal properties of the diamond lattice, or the kinetic energy would break the C_d-CH_3 bond before the excess energy had time to dissipate. The former is the more thermodynamically expected result.

180,000 NVE trajectories were run to determine the fraction of prompt CH_3 dissociation versus non-reactive thermalisation events. In order to get this many unique trajectories at a thermally equilibrated temperature a long NVT trajectory was run for 1.2 μs with a time step of 1 fs. A Langevin thermostat was used to maintain a temperature of 1300 K, with a friction coefficient of 10 s^{-1} and a heat bath of 1300 K. This is the temperature at which Carbon etching is observed experimentally under CVD growth conditions. A snapshot of geometries and velocities was taken at every 10 ps in the NVT simulation. These were used as initial conditions for the NVE trajectories, with the added kinetic 'kick' referred to above. The 10ps spacing is sufficient to prevent the starting point of each NVE trajectories from being correlated with the previous and following ones. Each of these simulations was then run for a total time of 10 ps with a 1 fs time step.

The kinetic 'kick' added to the simulations initial conditions was varied to assess the sensitivity of the model. The 180,000 NVE trajectories were divided evenly between 100, 120, and 140 kcal mol^{-1} 'kicks'. The fraction of prompt dissociation of CH_3 from the surface versus non-reactive events is shown in Table 20 below. As expected, the proportion of CH_3 prompt dissociation increases with the initial kinetic energy in the local hotspot at the beginning of the simulation.

However, the model does not appear to be highly sensitive to this increase. Therefore any error in the estimated energy of the C-H bond (Table 17) formation in scheme 1 should not unduly affect the estimation of the rate of CH_3 loss.

Table 20 – The fraction of prompt CH3 dissociation from the surface at three different levels of initial kinetic energy in an H atom in the surface methyl. A Poisson distribution of rare events (N) was assumed and the error is proportional to √N.

Energy /kcal mol^{-1}	Fraction prompt CH3 dissociation
100	0.018 ± 0.006%
120	0.065 ± 0.010%
140	0.090 ± 0.016%

It can clearly be inferred from table 1 that prompt dissociation is an extremely rare event and that most of the trajectories were non-reactive with the CH_3 remaining bonded to the surface. Figure 60 shows the C_d-CH_3 bond separation over the course of one such simulation. It demonstrates that this value fluctuates around an equilibrium bond length of 1.564 Å remaining bonded to the surface for the entire length of the 10 ps simulation. This is a relatively long length of time and is much greater than the time that it takes for the excess initial energy to diffuse into the bulk lattice.

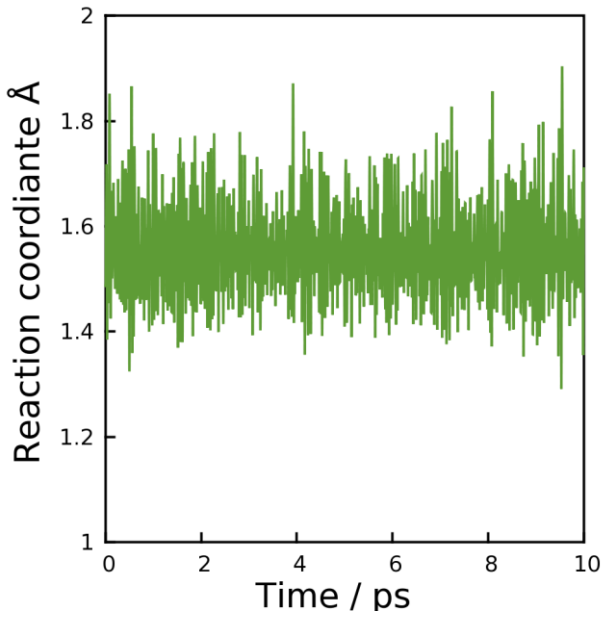

Comment [JNH3]: There's a typo in "coordinate" on the y axis of this figure.

Figure 60- Typical non-reactive trajectory. The majority of simulations produced no dissociation event. The extra energy from the locally 'hot' methyl is dissipated through the diamond lattice without breaking the C_d-CH_3 bond.

The time it takes for this excess initial energy to diffuse into the bulk diamond is shown below in Figure 61. This figure shows the kinetic energy in the C-H bond which has been 'kicked' as a function of time. This illustrates the rate at which energy diffuses from the locally hot region to the bulk. Most of the energy has left the region of the C-H bond by approximately 0.25ps and by 1ps this region is in thermal equilibrium with the rest of the bulk diamond.

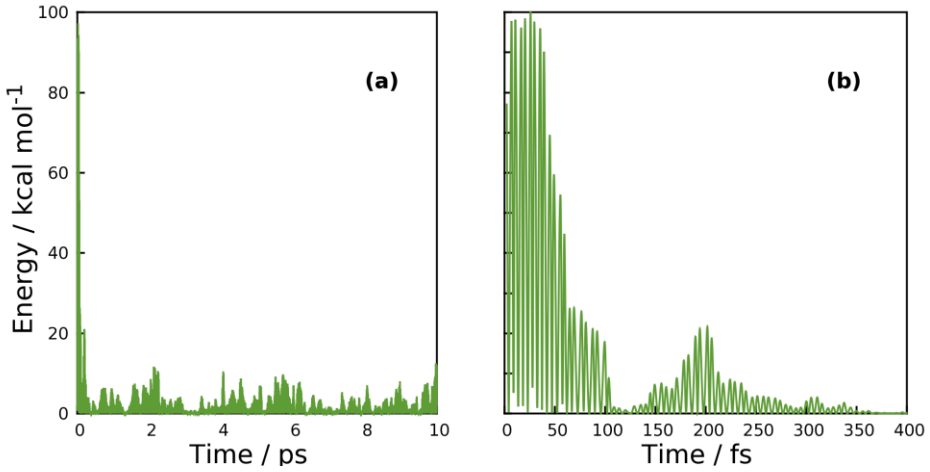

Figure 61 – Excess kinetic energy in the locally hot region of the 'kicked' C-H bond quickly dissipates to the bulk. (a) and (b) are the same trajectory on different time scales. At 1300 K 3 kcal mol-1 of kinetic energy would be expected and this is what is seen after the excess energy has dissipated in (b).

For those trajectories that did produce a dissociation event, this process occurred rapidly. Figure 62 shows a reactive trajectory with a prompt breaking of the C_d-CH_3 bond at approximately 250 fs into the simulations. When this is compared with the time evolution of the kinetic energy in the C-H bond (Figure 61 above) it can be seen that the breaking of the C_d-CH_3 bond occurs as the extra kinetic energy is just leaving the C-H bond and diffusing from the surface methyl to the diamond. All of the prompt dissociations occurred on the same time scale (~250 fs), which is 40 times quicker than the total time of the non-reactive trajectory in Figure 60. In the reactive case shown in Figure 62 the diffusion of energy did not carry on dissipating though the bulk of the diamond, but it was sufficient to break the bond holding the CH_3 to the surface before thermal equilibrium had been reached.

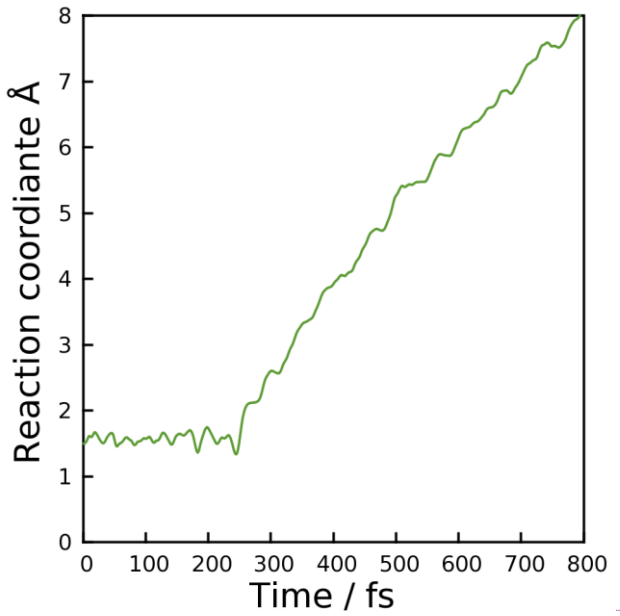

Comment [JNH4]: Coordinate has a typo in this Figure.

Figure 62 - Plot of the C_d-CH_3 reaction coordinate for a reactive NVE trajectory. The methyl breaks away from the surface at approximately 0.25ps. This is well before the energy can dissipate through the lattice.

The rate of CH_3 loss from the 2x1:{100} surface can be determined from the calculations discussed above. First we must estimate the rate of reaction for the $H^*(g)$ addition step in scheme 1 (R1):

$$C_d - CH_2{}^* + H^*(g) \rightarrow C_d - CH_3 \qquad (R2)$$

In average CVD conditions for MCD growth, the rate of adatom deactivation in the kMC model is approximately 9000 s^{-1}. At the highest estimate for non-equilibrium dissociation, the percent prompt dissociation was 0.1%. This would give a CH_3 loss rate for MCD diamond growth conditions as 9 s^{-1}. While this is not insignificant it is relatively slow.

5.3.4. Box molecular dynamics

Boxed molecular dynamics simulations were used in order to obtain the thermal potential of mean force (and thus the free energy profile[19]) of the dissociation reaction coordinate of CH_3 from the surface. By calculating the free

energy profile of this reaction for many temperatures it will then be possible to estimate a temperature-dependent free energy of activation. Using this and transition state theory the kinetic rate of thermal desorption can be determined. In the following section, a detailed description of the BXD procedure at 700K is given. In this work free energy profiles at 700K, 800K, 900K, 1000K, 1100K, 1200K, and 1300K are calculated. This is the temperature range of interest in the CVD diamond growth process. The procedure for doing this is practically the same at all of these temperatures. Therefore, the detailed method is only shown for one here.

In this work the reaction coordinate of C_d-CH_3 bond is divided into 13 boxes with varying size. It was not necessary to change the box number or sizes for any of the different temperatures to achieve convergence; this can sometimes be the case with this method. The box boundaries were on the following points on the reaction coordinate: 1.4 Å, 1.5 Å, 1.6 Å, 1.7 Å, 1.8 Å, 1.9 Å, 2.0 Å, 2.2 Å, 2.4 Å, 2.6 Å, 2.8 Å, 3.0 Å, 3.3 Å, and 4.0 Å. From this list it can be seen that the boxes are not evenly spaced. The boxes must be more tightly constrained in the middle section of the reaction coordinate as the gradient of the PMF is steeper along that portion.

The BXD simulation procedure was applied using a series of NVT trajectories for each temperature. As the technical details of this process are exactly the same except for a change in temperature only the full BXD procedure for 700 K is discussed in this section as any more would be redundant. One NVT trajectory was run for each box as the length of the total simulation required to achieve a highly accurate sampling of all of the phase space was long. Each box was run with a time step of 0.25 fs for a total time of 187.5 ps, using a Langevin thermostat with a friction coefficient of 25 s^{-1} and a heat bath of 700 K. The only difference in each of these trajectories is the size and position of the constrained coordinate for the BXD procedure in CHARMM (box boundaries previous paragraph). This meant that each box could be run in parallel dramatically cutting down on the real time computational cost. The reaction coordinate was

constrained by implementing the velocity inversion routine described in section 1.2.2.

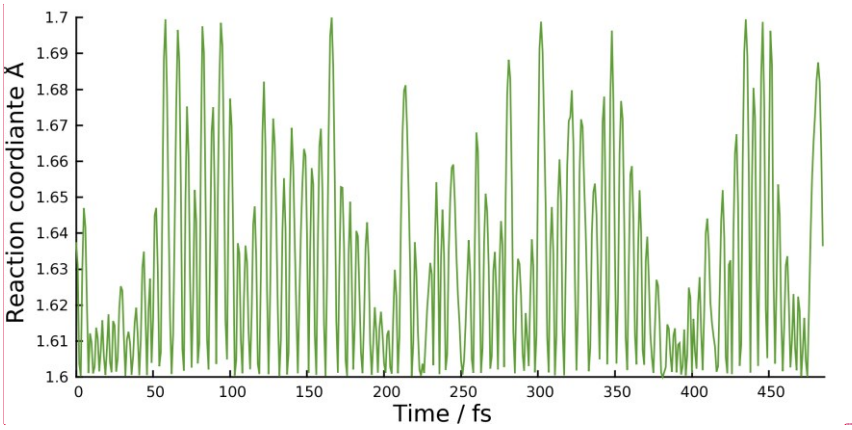

Comment [JNH5]: No I think it is fine. But once again 'coordinate' has a typo.

Comment [J6]: Need better pic here

Figure 63-Close up of a BXD box where the C_d-CH_3 coordinate is constrained between 1.6 and 1.7 Å; necessary elements of a successful BXD run are a small enough time step to ensure accurate dynamics but more importantly the box size must be such that a boundary crossing occurs frequently enough to produce good statistics.

An output of the C_d-CH_3 distance is printed every 10 time-steps and saved for each box. If the coordinate reaches a boundary then the time step and boundary is recoded in this file as well. After the individual box trajectories are completed, they are stitched together to form one long file of the C_d-CH_3 coordinate over time with the frequency of velocity inversion events (Figure 64). This data is then used to calculate the PMF/free energy profile along the reaction coordinate.

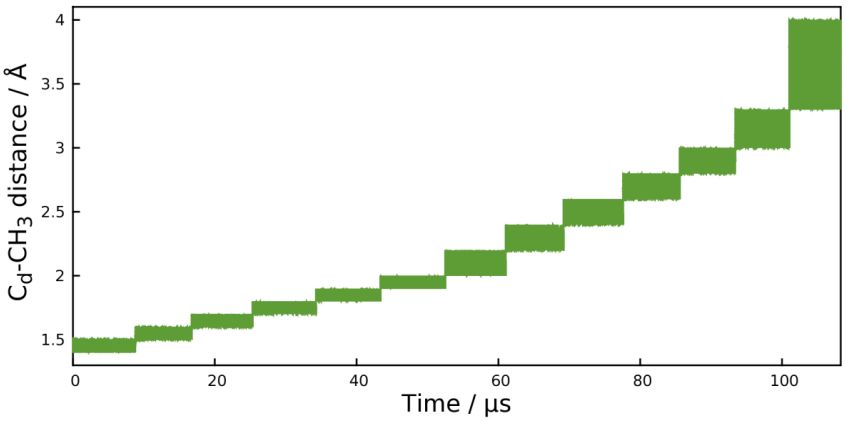

Figure 64-This figure shows the total BXD simulation for 700 K. Each box was run in parallel, as 109 µs is a relatively long simulation, and stitched together for post processing to calculate the PMF.

A trajectory similar to the one described above was simulated for each temperature in question. The residence time in each box and the forward and reverse transition rate coefficient for each box was calculated from these trajectories. Using this data and Equation 6 in section 5.2.2, ΔG_n for each box between 1.4Å and 4.0Å was calculated at each temperature. The free energy curves generated from these calculations are shown in the figure below.

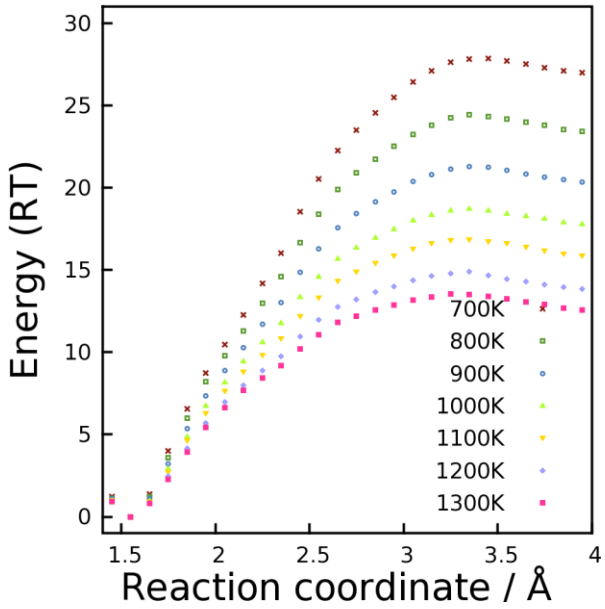

Figure 65- BXD results: free energy curves (in RT units) for simulations at 700, 800, 900, 1000, 1100, 1200, and 1300 K

These results clearly illustrate a decrease in the free energy of dissociation as is expected. There is a barrier to dissociation visible in each curve as the energy decreases after a maximum to an asymptotic value. This is due to an entropic gain for the methyl just after the breaking of the C—C bond.

From these free energy profiles it was a simple matter to calculate the rate constant to dissociation. The energy at the equilibrium geometry is normalised to zero for each temperature in Figure 65 so the Gibbs free energy of activation is the barrier height. The rate constant for desorption was then calculated using transition state theory and the Eyring equation (Equation 2.5). The temperature of the simulation, the free energy barrier, and the calculated rate constant are all listed in Table 21 below.

Table 21- Gibbs free energy of activation determined from the results presented in Figure 65 above and the resulting rate constant for each temperature determined by the Eyring equation (Equation X.x)

Temperature / K	Gibbs free energy / RT	Rate constant / s^{-1}
700	27.84	11.84
800	24.42	413.89
900	21.28	10751.34
1000	18.72	154880.50
1100	16.86	1095698
1200	14.88	8605722
1300	13.55	35157806

The rate constant for each temperature was then plotted on an Eyring plot to determine the apparent enthalpy of activation, $\Delta H^{\ddagger}$, for the reaction as calculated by the BXD simulations. This plot is shown below in Figure 66. Using Equation 11 (the linear Eyring equation) the fit gives the enthalpy of activation, $\Delta H^{\ddagger}$, and the entropy of activation, $\Delta S^{\ddagger}$, for the thermal dissociation of methyl.

$$\ln\frac{k}{T} = \frac{-\Delta H^{\ddagger}}{R}\cdot\frac{1}{T} + \ln\frac{k_B}{h} + \frac{\Delta S^{\ddagger}}{R} \tag{10}$$

$\Delta H^{\ddagger}$ = 182 kJ mol^{-1}

$\Delta S^{\ddagger}$ = 26.7 J mol^{-1}

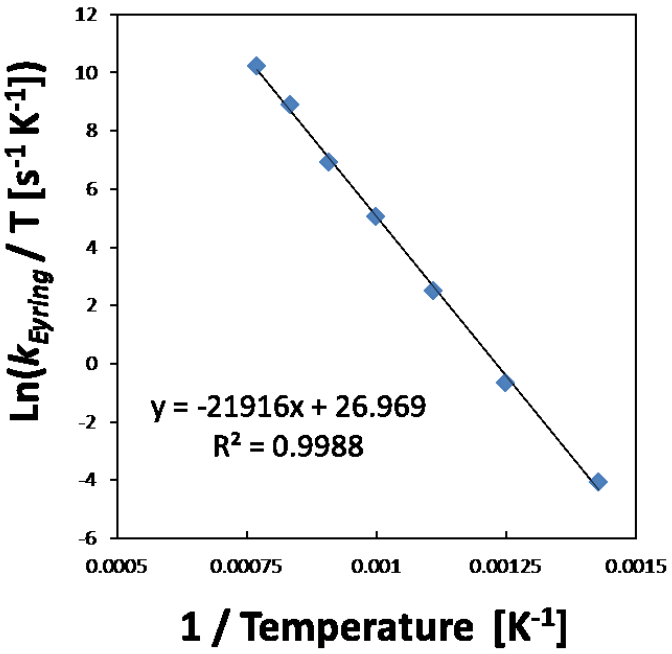

Figure 66-Eyring plot of rate constants from Table 21

5.3.5. Long simulation – Time correlation

Next we executed a long NVE trajectory using the EVB potential in order to obtain information about the energy transfer within the diamond lattice based on fluctuation-dissipation theory. A starting position and velocity configuration was taken from one of the previous NVE simulations that had produced a reactive event. This NVE trajectory was run just in every way as the previous one, but without the initial kinetic "kick". This simulation was run for 1 ns in total with a time step of 1 fs. The velocities were saved at each time step so that the kinetic energy of each atom as a time dependent function could be calculated. This kinetic energy was used to determine the time correlation of energy (equation 4) for two different subsets of atoms around the surface carbon atom where the pendant methyl was attached. The correlation functions produced provide information on the rate of energy transfer between the reactive subset and the diamond bulk.

$$C(t) = \langle \delta E(0) \delta E(t) \rangle = \langle E(0)E(t) \rangle - \langle E \rangle^2 \quad (4)$$

Specifically, for some initial non-equilibrium condition, e.g. corresponding to C-H bond formation at the surface leading to a 'hot' methyl group containing $\Delta E'(0)$ of initial energy in excess of thermal energy, the excess energy at a later time τ, $\Delta E'(\tau)$,should vary as shown in Eq. (5): [27]

$$\Delta E'(\tau) = \Delta E'(0)\frac{C(\tau)}{C(0)} \quad (5)$$

The time correlation functions for the energy dissipation have been calculated for two different-sized systems around the surface-bound methyl group, a subset of 16 and 34 atoms respectively of the full system. These functions have then been used to compute the expected excess energy to be found in each sub-system assuming that an initial non-equilibrium condition leads to an initial excess amount of energy of 450 kJ mol-1 (108 kcal mol-1). The resulting predicted time evolution of the excess energy is shown in Figure 67. As the energy dissipates through the bulk the energy equalises to the thermal energy of the subset. Both energy dissipation curves are plotted together to show that there is no fundamental difference in the rate of energy diffusion. The energy for both has practically approached the thermal energy of the subset by ~250 fs. This agrees qualitatively with the assessment of the energy loss in the C—H bond in Figure 61. The energy dissipation through the bulk is so quick that the rate is similar for the C—H bond by itself, and the 16 and 34 atom subset around the thermally hot CH_3 on the surface. Note that the energy of the system has been estimated simply by taking the *kinetic* energy of the atoms within the considered sub-system. The neglect of the potential energy terms presumably accounts for the high-frequency (and physically unrealistic) component of the predicted energy decay.

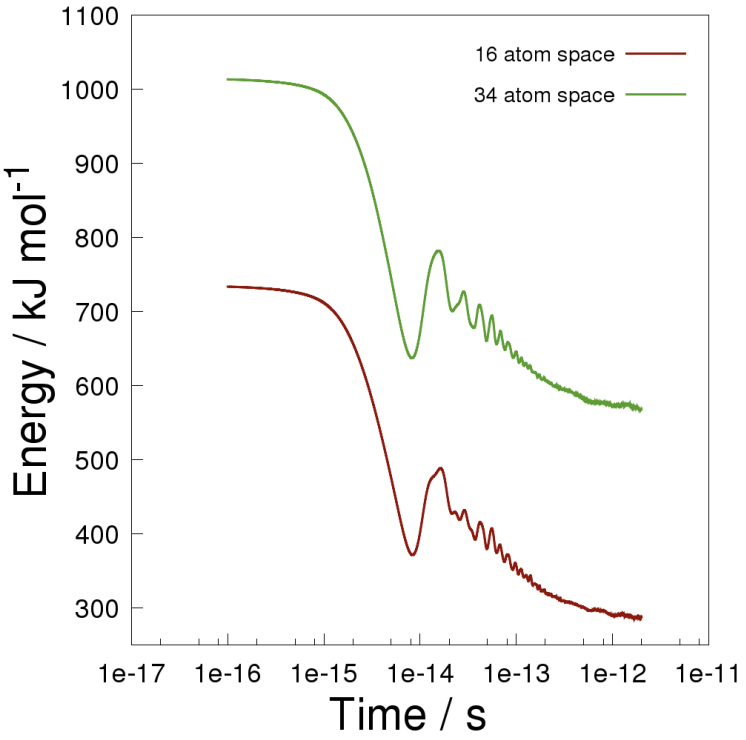

Figure 67-Excess energy decay function for two subsets of atoms around the locally hot methyl on the (100) diamond surface (Figure 53 (a))

5.4. Conclusions

The growth of CVD diamond is a competition between adsorption and etching. Although it has been observed experimentally, [6] the general mechanism by which it occurs is not well understood and debated in the literature. [4,5,28,29] It was proposed in this work that the desorption of a CH_3 adsorbate is a step to carbon loss from the surface. Two routes to methyl loss from the (100):(2×1):H diamond surface were investigated in the work presented above; a non-equilibrium route (breaking of the C-C bond before the dissipation of energy into the bulk from reaction shown in Figure 52) and a thermal decomposition.

An analytical reactive potential energy surface of the dissociation of H_3C-$C(CH_3)_3$ (neopentane) was created from a CCSD(T) corrected CASPT2 scan along the dissociation reaction coordinate using the EVB method. This potential was

then transferred for use on a diamond surface with only slight modification. The energy surface was used in molecular dynamics trajectories simulating CH_3 dissociation.

The non-equilibrium dissociation of methyl was investigated by running 160,000 non-correlated NVE trajectories. Each trajectory had an additional 108-148 kcal mol^{-1} of initial energy to replicate the locally energetic region just after the $H^{\cdot} + CH_2^{\cdot}$ recombination. The energy quickly dissipated through the bulk within 250 fs of the simulation for an overwhelming majority of the trajectories, as would be expected. However, a small percentage of dissociative events did occur. The percentage of prompt CH_3 dissociation was 0.18%, 0.65%, and 0.9% with a 108, 128, 148 kcal mol^{-1} 'kick' of excess initial energy.

Boxed molecular dynamics calculations were implemented at 700, 800, 900, 1000, 1100, 1200, and 1300 K using the EVB potential. Free energy profiles for CH_3 dissociation at each of these temperatures were generated and the Gibbs free energy of the reaction at each temperature was determined by their barrier heights. Rate constants for each temperature were calculated using the Eyring equation and an Eyring plot was used to determine the enthalpy and entropy of activation for the reaction as $\Delta H^{\ddagger}$ = 182 kJ mol^{-1} and $\Delta S^{\ddagger}$ = 26.7 J mol^{-1}. At 1100 K this gives a thermal rate of decomposition for CH_3 of 1.61×10^5 s^{-1}, which is much faster than the non-equilibrium rate of dissociation which was 9 s^{-1}.

5.5. References

(1) Booth, J.; Vazquez, S.; Martinez-Nunez, E.; Marks, A.; Rodgers, J.; Glowacki, D. R.; Shalashilin, D. V. Recent Applications of Boxed Molecular Dynamics: A Simple Multiscale Technique for Atomistic Simulations. *Philos. Trans. R. Soc. Math. Phys. Eng. Sci.* **2014**, *372*, 20130384.

(2) Butler, J. E.; Woodin, R. L.; Brown, L. M.; Fallon, P. Thin Film Diamond Growth Mechanisms [and Comment]. *Philos. Trans. R. Soc. Lond. Ser. Phys. Eng. Sci.* **1993**, *342*, 209–224.

(3) Villalpando, I.; John, P.; Porro, S.; Wilson, J. I. B. Hydrogen Plasma Etching of Diamond Films Deposited on Graphite. *Diam. Relat. Mater.* **2011**, *20*, 711–716.

(4) Netto, A.; Frenklach, M. Kinetic Monte Carlo Simulations of CVD Diamond growth—Interlay among Growth, Etching, and Migration. *Diam. Relat. Mater.* **2005**, *14*, 1630–1646.

(5) May, P. W.; Harvey, J. N.; Allan, N. L.; Richley, J. C.; Mankelevich, Y. A. Simulations of Chemical Vapor Deposition Diamond Film Growth Using a Kinetic Monte Carlo Model and Two-Dimensional Models of Microwave Plasma and Hot Filament Chemical Vapor Deposition Reactors. *J. Appl. Phys.* **2010**, *108*, 114909.

(6) Rawles, R. E.; Komarov, S. F.; Gat, R.; Morris, W. G.; Hudson, J. B.; D'Evelyn, M. P. Mechanism of Surface Smoothing of Diamond by a Hydrogen Plasma. *Diam. Relat. Mater.* **1997**, *6*, 791–795.

(7) Cheesman, A.; Harvey, J. N.; Ashfold, M. N. R. Studies of Carbon Incorporation on the Diamond {100} Surface during Chemical Vapor Deposition Using Density Functional Theory. *J. Phys. Chem. A* **2008**, *112*, 11436–11448.

(8) Brooks, B. R.; Brooks, C. L., 3rd; Mackerell, A. D., Jr; Nilsson, L.; Petrella, R. J.; Roux, B.; Won, Y.; Archontis, G.; Bartels, C.; Boresch, S.; et al. CHARMM: The Biomolecular Simulation Program. *J. Comput. Chem.* **2009**, *30*, 1545–1614.

(9) Frisch, M. J.; Trucks, G. W.; Schlegel, H. B.; Scuseria, G. E.; Robb, M. A.; Cheeseman, J. R.; Scalmani, G.; Barone, V.; Mennucci, B.; Petersson, G. A.; et al. *Gaussian 09, Revision A.1*; Gaussian, Inc.: Wallingford, CT, 2009.

(10) Werner, H.-J.; Knowles, P. J.; Knizia, G.; Manby, F. R.; Schütz, M. Molpro: A General-Purpose Quantum Chemistry Program Package. *Wiley Interdiscip. Rev. Comput. Mol. Sci.* **2012**, *2*, 242–253.

(11) Werner, H.-J.; Knowles, P. J.; Knizia, G.; Manby, F. R.; Schütz, M.; Celani, P.; Korona, T.; Lindh, R.; Mitrushenkov, A.; Rauhut, G.; et al. *MOLPRO, Version 2012.1, a Package of Ab Initio Programs*; molpro, 2012.

(12) Jensen, F. *Introduction to Computational Chemistry*; John Wiley & Sons, 2007.

(13) Warshel, A.; Weiss, R. M. An Empirical Valence Bond Approach for Comparing Reactions in Solutions and in Enzymes. *J. Am. Chem. Soc.* **1980**, *102*, 6218–6226.

(14) Kamerlin, S. C. L.; Warshel, A. The Empirical Valence Bond Model: Theory and Applications. *Wiley Interdiscip. Rev. Comput. Mol. Sci.* **2011**, *1*, 30–45.

(15) Glowacki, D. R.; Orr-Ewing, A. J.; Harvey, J. N. Product Energy Deposition of CN + Alkane H Abstraction Reactions in Gas and Solution Phases. *J. Chem. Phys.* **2011**, *134*, 214508.
(16) Farah, K.; Mueller-Plathe, F.; Boehm, M. C. Classical Reactive Molecular Dynamics Implementations: State of the Art. *Chemphyschem* **2012**, *13*, 1127–1151.
(17) Kim, Y.; Corchado, J. C.; Villà, J.; Xing, J.; Truhlar, D. G. Multiconfiguration Molecular Mechanics Algorithm for Potential Energy Surfaces of Chemical Reactions. *J. Chem. Phys.* **2000**, *112*, 2718–2735.
(18) Chang, Y. T.; Miller, W. H. An Empirical Valence Bond Model for Constructing Global Potential Energy Surfaces for Chemical Reactions of Polyatomic Molecular Systems. *J. Phys. Chem.* **1990**, *94*, 5884–5888.
(19) Glowacki, D. R.; Paci, E.; Shalashilin, D. V. Boxed Molecular Dynamics: A Simple and General Technique for Accelerating Rare Event Kinetics and Mapping Free Energy in Large Molecular Systems. *J. Phys. Chem. B* **2009**, *113*, 16603–16611.
(20) Glowacki, D. R.; Paci, E.; Shalashilin, D. V. Boxed Molecular Dynamics: Decorrelation Time Scales and the Kinetic Master Equation. *J. Chem. Theory Comput.* **2011**, *7*, 1244–1252.
(21) US Department of Commerce, N. Standard Reference Data http://www.nist.gov/srd/ (accessed Feb 17, 2014).
(22) Cheesman, A.; Harvey, J. N.; Ashfold, M. N. R. Computational Studies of Elementary Steps Relating to Boron Doping during Diamond Chemical Vapour Deposition. *Phys. Chem. Chem. Phys.* **2005**, *7*, 1121–1126.
(23) Richley, J. C.; Harvey, J. N.; Ashfold, M. N. R. On the Role of Carbon Radical Insertion Reactions in the Growth of Diamond by Chemical Vapor Deposition Methods. *J. Phys. Chem. A* **2009**, *113*, 11416–11422.
(24) Richley, J. C.; Harvey, J. N.; Ashfold, M. N. R. Boron Incorporation at a Diamond Surface: A QM/MM Study of Insertion and Migration Pathways during Chemical Vapor Deposition. *J. Phys. Chem. C* **2012**, *116*, 18300–18307.
(25) Richley, J. C.; Harvey, J. N.; Ashfold, M. N. R. Boron Incorporation at a Diamond Surface: A QM/MM Study of Insertion and Migration Pathways during Chemical Vapor Deposition. *J. Phys. Chem. C* **2012**, *116*, 18300–18307.
(26) Halgren, T. A. Merck Molecular Force Field. I. Basis, Form, Scope, Parameterization, and Performance of MMFF94. *J. Comput. Chem.* **1996**, *17*, 490–519.
(27) Chandler, D. Introduction to Modern Statistical Mechanics. *Introd. Mod. Stat. Mech. David Chandl. Pp 288 Foreword David Chandl. Oxf. Univ. Press Sep 1987 ISBN-10 0195042778 ISBN-13 9780195042771* **1987**, *-1*.
(28) Stallcup, R. E.; Perez, J. M. Scanning Tunneling Microscopy Studies of Temperature-Dependent Etching of Diamond (100) by Atomic Hydrogen. *Phys. Rev. Lett.* **2001**, *86*, 3368–3371.
(29) Skokov, S.; Weiner, B.; Frenklach, M. Elementary Reaction Mechanism for Growth of Diamond (100) Surfaces from Methyl Radicals. *J. Phys. Chem.* **1994**, *98*, 7073–7082.

Chapter 6

Summary

6.1. Conclusions

The growth of diamond by chemical vapour deposition is a mature technical process but many new variants are being developed, some of which were discussed in the introduction. However, the complete theoretical picture of the physical and chemical processes involved in this growth is incomplete. The work presented here was intended to link the atomistic theory of diamond growth with macroscopic observables.

In this thesis, work concerning the multi-scale computational modelling of diamond grown by the chemical vapour deposition (CVD) method has been presented. The development and systematic testing of a 3-dimensional kinetic Monte Carlo (kMC) model of the chemical vapour deposition of diamond growing on the (100) surface was discussed. This novel kMC simulation program, written in Fortran 90 (Appendix), was used to probe how atomistic processes such as the etching of CH_3 from the surface, the adsorption of CH_3 onto the surface, and the migration of CH_2 ad-species across the surface affect the surface morphology of the resulting simulated diamond. Finally a reactive analytical potential energy surface for the dissociation of CH_3 from the (100):(2×1):H surface was developed. Molecular dynamics simulations were used to probe the rates of non-equilibrium dissociation as well as the thermal decomposition of CH_3.

A systematic exploration of the parameter space of the 3-D kMC model was conducted in order to verify the sensitivity of the output of the program to changes in the model input parameters obtained from experiments and

theoretical calculations. The parameter that most affected the model was found to be the concentration of CH_3 near the surface. This influences the rate of adsorption and accordingly the growth rate and surface roughness. An accurate knowledge of the concentrations of gases above the surface must be known in order to have reliable output from the kMC model. In this model the data regarding the concentrations of gases is based on extensive theoretical modelling from the Bristol-Moscow collaboration. [1]

The validation of the model also yielded the following results. The growth rate was found to increase with the temperature of the substrate, peak at 1000 °C and then begin to decrease. This phenomenon has been observed in experiments; growth on the (100) increased and then peaks with a subsequent decrease as temperature increases. [2] Our kMC model is the first to theoretically reproduce this, though others have reproduced this trend on the (110) surface. [3] As the rate for deactivation was decreased the model produced smoother diamond at a much reduced growth rate which has also been observed experimentally. [4]

Three different models for the etching of an activated ad-species were tested in the kMC model. The original model[5,6] of etching was a rate constant based on a fraction of the CH_3 adsorption rate as it was found in experiments that the rate of carbon loss when the process gasses were turned off was 10% of the rate of adsorption with the gas on. The next model was a rate constant based on the Eyring equation with a linear dependence on the next nearest neighbour (NN). The third model was an Eyring equation with a dependence on the next nearest neighbour in the exponential function. Qualitatively the Eyring model with the exponential NN dependence produced rougher surfaces and the Eyring model with linear NN dependency produced smoother surfaces. The exponential model is the more theoretically justifiable model, as the bonding in nearest neighbours does not decrease linearly. As a carbon in the diamond lattice becomes more bonded, towards its tetrahedral structure, it becomes harder to remove (less energetically favourable).

The rate of CH_3 adsorption was also changed to include a linear dependence on the configuration of the nearest neighbours of the adsorbing site.

It was found that this change had a more substantial effect than any of the other changes made to the etching models. This change produced surfaces with a greatly increased surface roughness value. Also these surfaces had very well defined facets that qualitatively resemble crystallite formation found in actual CVD growth. In the case of the UNCD (HF) simulation these facets were approximately 2 nm in size which is close to the 5 nm crystal size observed under similar growth conditions. [7]

The critical nucleus, the smallest unetchable configuration that can nucleate a new layer, was found to be the 2-block dimer in all cases except for SCD and UNCD (MW) growth when migration was turned off; in this case it was the monomer. This is the same size structure that was assumed to be the critical nucleus in the 2-dimensional model.

The growth of CVD diamond is a competition between adsorption and etching. Although it has been observed experimentally, [8] the general mechanism by which etching occurs is not well understood and debated in the literature. [6,9-11] It was proposed in this work that the desorption of a CH_3 adsorbate is a step to carbon loss from the surface. Two routes to methyl loss from the (100):(2×1):H diamond surface were investigated in the work presented above; a non-equilibrium route and a thermal decomposition.

An analytical reactive potential energy surface of the dissociation of H_3C-$C(CH_3)_3$ (neopentane) was created from a CCSD(T) corrected CASPT2 scan along the dissociation reaction coordinate using the EVB method. This potential was then transferred for use on a diamond surface with only slight modification. The energy surface was used in molecular dynamics trajectories simulating CH_3 dissociation.

The non-equilibrium dissociation of methyl was investigated by running 160,000 non-correlated NVE trajectories. Each trajectory had an additional 108-148 kcal mol^{-1} of initial energy to replicate the locally energetic region just after and $H\cdot + CH_2\cdot$ recombination. The energy quickly dissipated through the bulk within 250 fs of the simulation for an overwhelming majority of the trajectories,

as would be expected. However, a small percentage of dissociative events did occur. The percentage of prompt CH_3 dissociation was 0.18%, 0.65%, and 0.9% with a 108, 128, 148 kcal mol^{-1} 'kick' of excess initial energy.

Boxed molecular dynamics calculations were implemented at 700, 800, 900, 1000, 1100, 1200, and 1300 K using the EVB potential. Free energy profiles for CH_3 dissociation at each of these temperatures were generated and the Gibbs free energy of the reaction at each temperature was determined by their barrier heights. Rate constants for each temperature were calculated using the Eyring equation and an Eyring plot was used to determine the enthalpy and entropy of activation for the reaction as $\Delta H^{\ddagger}$ = 182 kJ mol^{-1} and $\Delta S^{\ddagger}$ = 26.7 J mol^{-1}. At 1100 K this gives a thermal rate of decomposition for CH_3 of 1.61×10^{5} s^{-1}, which is much faster than the non-equilibrium rate of dissociation.

6.2. Further work

One of the major drawbacks to the kMC model presented in this thesis is that it only used reactions that take place on the (100) surface and the diamond surface is reduced to a simple cubic structure. The simplification of the surface is appropriate when just simulating the (100) surface, but a true representation of the surface cannot be produced based only on simulation of one growing surface. It would be much more appropriate to have all known reactions on every surface in the rate catalogue. This could be done with the on-lattice approximation and a predefined rate catalogue but it would be more successful with off-lattice and self-learning methods that calculate rate constants on the fly. [12–14] The improved model would be better able to predict surface structure features. However, this would increase the complexity of the program considerably as well as introducing significant efficiency concerns. In fact a project this large could probably be split into a number of smaller projects.

A less ambitious attempt to improve the current model would be to add surface reconstruction to the model of the (100) surface as it is currently not included. Theoretical studies of the inclusion of CH_3 into the dimer bond by a

ring opening and closing mechanism have been conducted at Bristol. [15] The macroscopic effects of these mechanisms could be more easily tested in models which included a reconstructed surface.

Smaller projects include the further study of the etching process. Theoretical studies of carbon being etched by more complicated mechanisms from more tightly bound configurations. The first of these could be the probing of the mechanism by which a carbon that is a part of 2×1 reconstruction could be lost to the gas phase. The energetics of such a reaction could then be used to estimate a rate constant for the process in the modified kMC (100) model with the surface reconstruction. Although for a more realistic simulation the full kMC model of all surface reactions should be developed.

6.3. References

(1) May, P. W.; Mankelevich, Y. A. From Ultrananocrystalline Diamond to Single Crystal Diamond Growth in Hot Filament and Microwave Plasma-Enhanced CVD Reactors: A Unified Model for Growth Rates and Grain Sizes. *J. Phys. Chem. C* **2008**, *112*, 12432–12441.

(2) Kweon, D.-W.; Lee, J.-Y.; Kim, D. The Growth Kinetics of Diamond Films Deposited by Hot-filament Chemical Vapor Deposition. *J. Appl. Phys.* **1991**, *69*, 8329–8335.

(3) Battaile, C. C.; Srolovitz, D. J. Kinetic Monte Carlo Simulation of Chemical Vapor Deposition. *Annu. Rev. Mater. Res.* **2002**, *32*, 297–319.

(4) Battaile, C. C.; Srolovitz, D. J.; Oleinik, I. I.; Pettifor, D. G.; Sutton, A. P.; Harris, S. J.; Butler, J. E. Etching Effects during the Chemical Vapor Deposition of (100) Diamond. *J. Chem. Phys.* **1999**, *111*, 4291–4299.

(5) May, P. W.; Harvey, J. N.; Allan, N. L.; Richley, J. C.; Mankelevich, Y. A. Simulations of Chemical Vapor Deposition Diamond Film Growth Using a Kinetic Monte Carlo Model. *J. Appl. Phys.* **2010**, *108*, 014905.

(6) May, P. W.; Harvey, J. N.; Allan, N. L.; Richley, J. C.; Mankelevich, Y. A. Simulations of Chemical Vapor Deposition Diamond Film Growth Using a Kinetic Monte Carlo Model and Two-Dimensional Models of Microwave Plasma and Hot Filament Chemical Vapor Deposition Reactors. *J. Appl. Phys.* **2010**, *108*, 114909.

(7) Wang, C.-S.; Tong, G.-H.; Chen, H.-C.; Shih, W.-C.; Lin, I.-N. Effect of N2 Addition in Ar Plasma on the Development of Microstructure of Ultra-Nanocrystalline Diamond Films. *Diam. Relat. Mater.* **2010**, *19*, 147–152.

(8) Rawles, R. E.; Komarov, S. F.; Gat, R.; Morris, W. G.; Hudson, J. B.; D'Evelyn, M. P. Mechanism of Surface Smoothing of Diamond by a Hydrogen Plasma. *Diam. Relat. Mater.* **1997**, *6*, 791–795.

(9) Stallcup, R. E.; Perez, J. M. Scanning Tunneling Microscopy Studies of Temperature-Dependent Etching of Diamond (100) by Atomic Hydrogen. *Phys. Rev. Lett.* **2001**, *86*, 3368–3371.

(10) Netto, A.; Frenklach, M. Kinetic Monte Carlo Simulations of CVD Diamond growth—Interlay among Growth, Etching, and Migration. *Diam. Relat. Mater.* **2005**, *14*, 1630–1646.

(11) Skokov, S.; Weiner, B.; Frenklach, M. Elementary Reaction Mechanism for Growth of Diamond (100) Surfaces from Methyl Radicals. *J. Phys. Chem.* **1994**, *98*, 7073–7082.

(12) Binder, K.; Heermann, D. *Monte Carlo Simulation in Statistical Physics: An Introduction*; Springer Science & Business Media, 2010.

(13) Landau, D. P.; Binder, K. *A Guide to Monte Carlo Simulations in Statistical Physics*; Cambridge University Press, 2009.

(14) Voter, A. F. INTRODUCTION TO THE KINETIC MONTE CARLO METHOD. In *Radiation Effects in Solids*; Sickafus, K. E.; Kotomin, E. A.; Uberuaga, B. P., Eds.; NATO Science Series; Springer Netherlands, 2007; pp. 1–23.

(15) Cheesman, A.; Harvey, J. N.; Ashfold, M. N. R. Studies of Carbon Incorporation on the Diamond {100} Surface during Chemical Vapor Deposition Using Density Functional Theory. *J. Phys. Chem. A* **2008**, *112*, 11436–11448.

APPENDIX

A copy of the kinetic Monte Carlo program written in Fortran 90 which was developed during the course of the PhD project with the input.txt and energy.txt file with must be in the same directory as the executable.

```
!-------------------------------------------------------------------------------
!                          3-D kinetic Monte Carlo simulation
!                  of growth of CVD diamond on the (100) surface
!
!                                       v2.0
!
!       Author - Jeff Rodgers
!       Date   - 4 Oct 2013
!
!       main.f90 is the main program from which the simulation starts and ends
!
!       Description -   This program simulates the growth of CVD diamond on
!                       The (100) surface. Many of the rate constant in the
!                       Catalogue are modified from the simplified 2-D model
!                       From the paper 'J. Appl. Phys. 108 (2010) 114909'.
!                       New to this model is etching modelled as an activated
!                       Process, with an exponential dependence on bonding to
!                       Nearest neighbours
!
!-------------------------------------------------------------------------------


program KMC

use general_module            !Environment modules loaded
use rates_module
use surface_module

implicit none

real(kind=8) :: ratesum, ran1,ran2

integer ::  i,j,k,cnt,chosen,prev_chosen,time_temp
integer, allocatable, dimension(:,:) :: height_arr

TotalTime = 0;chosen=0;dt = 0;lowest_num = 2;time_temp = 1

open(unit=18,file="adatom.txt")    !Open output streams to print what's
                     !going on during the program run!
open(unit=9,file="test.out")    !test.out now deprecated
open(unit=29,file="visual.out")
open(unit=39,file="growth_vs_time.txt")
open(unit=61,file="roughness_plot.txt")
open(unit=20,file="main_output.txt")

write (20,*) ,"-----------------------------------------------------------------"
call read_input_file()
call read_energy_file()
call paulsrates()
call initialise_variables()
write (20,*),"-----------------------------------------------------------------"

n = num_rts_per_site*grid_x*grid_y  !max number of posible rates(6 per grid site)

allocate(surface(3,grid_x,grid_y)); surface = 1
allocate(rategrid(3,n ))
allocate(reverserategrid(grid_x,grid_y ))
allocate(rates(n))
allocate(rsv(n))
allocate(height_arr(grid_x,grid_y))

call initialise_rates()
surface(1,:,:) = 0
if (isRandom) CALL init_random_seed()          !Random seed can be turned on or off with
boolean from input file

!The main Monte Carlo loop begins here
!This is where the magic happens!
mcsteps = 1;cnt=1
chosen = 1
prev_chosen = 1

rsv = 0                !Rate Sum Vector(rsv), ordered sum of rates
rsv(1) = rates(1)
```

```
do j = 2,n
      rsv(j) = rsv(j-1)+rates(j)
end do

do while (TotalTime < endTime)
      ratesum = sum(rates)
        !Rate Sum Vector(rsv), ordered sum of rates
      if (lowest_num .eq. 1) then
            rsv(1) = rates(1)
            lowest_num = 2
      end if
      do j = lowest_num,n
            rsv(j) = rsv(j-1)+rates(j)
      end do
      call random_number(ran1)
      ran2 = ran1 * ratesum
      call locate(rsv, ran2, chosen, n)
      lowest_num = 0
      if (chosen > n) then
            print *, "All of your rates are now zero"
            goto 999
      end if
      x_do = rategrid(1,chosen); y_do = rategrid(2,chosen);ratetype = rategrid(3, chosen)
      prev_chosen = chosen

      call execute_rate(x_do,y_do,chosen)
      call update_time(ran1, ratesum)
      height_arr =  surface(1,:,:)
      if (TotalTime .gt. (time_temp*output_Time_Step)) then
            call stats(height_arr)
            write(61,*) TotalTime,",",mcsteps,",",rmsdh,",",rms
            write(39,*) TotalTime, (0.08917*0.001*aveheight*3600)/TotalTime
            write(18,*)
TotalTime,adatom_Adsorption_Count,etch_Count,surface_Activation_Count,surface_Deactivatio
n_Count,&
adatom_Activation_Count,adatom_Deactivation_Count,surface_Migration_Count,beta_Count,doub
le_Activation_Count,&
double_Deactivation_Count,triple_Activation_Count,triple_Deactivation_Count,CH2_Adsorptio
n_Count,CH_Adsorption_Count,&
C_Adsorption_Count

            time_temp = time_temp + 1
      end if
!           write(9,*)
mcsteps,ratetype,TotalTime,adatom_Adsorption_Count,etch_Count,surface_Activation_Count,su
rface_Deactivation_Count,&
!adatom_Activation_Count,adatom_Deactivation_Count,surface_Migration_Count,beta_Count,dou
ble_Activation_Count,&
!double_Deactivation_Count,triple_Activation_Count,triple_Deactivation_Count,CH2_Adsorpti
on_Count,CH_Adsorption_Count,&
!C_Adsorption_Count

      mcsteps = mcsteps + 1
      cnt = cnt + 1
end do    !This is the end of one MC step
999 print *, "End of Program"

call write_output()

!Deallocate all allocatable arrays
deallocate(surface,rategrid,reverserategrid, rates, height_arr)
!Close all output streams
close(18);close(29);close(39);close(61);close(20);close(9)

!An awk script is called to make visual.out look more appealing to movie.py
      call system('awk -f vis.awk visual.out > tmp')
      call system('mv tmp visual.out')
      call system('mv visual.out visualise')
      close(29)

end program KMC


!Awk script vis.awk
!{
!print $1 "\t" $2 "\t" $3 "\t" $4 "\t" $5 "\t" $6 "\t" $7 "\t" $8
!}
```

```
adatom_activation.f90
!----------------------------------------------------------------------
!This subroutine executes an adatom activation process
!Surface type is changed to 4 and new rate is set for x,y and chosen
!----------------------------------------------------------------------

subroutine adatom_activation(x,y,chosen)
use surface_module
use rates_module
implicit none

integer, intent(in) :: x,y,chosen

if(surface(2,x,y).ne. green .and. surface(2,x,y) .ne. red&
 .and. surface(2,x,y) .ne. light_red) then
           write(*,*) "what the deuce? Not a deactivated adatom!"
          stop
end if
if (surface(2,x,y) .eq. green) then
          surface(2,x,y) = red
          adatom_Activation_Count = adatom_Activation_Count + 1
else if (surface(2,x,y) .eq. red) then
          surface(2,x,y) = light_red
          double_Activation_Count = double_Activation_Count + 1
else if (surface(2,x,y) .eq. light_red) then
          surface(2,x,y) = yellow
          triple_Activation_Count = triple_Activation_Count + 1
else
          write(*,*) "What the deuce man?"
end if

call set_new_rate(x,y, reverserategrid(x,y))

end subroutine adatom_activation


adatom_deactivation.f90
!----------------------------------------------------------------------
!This subroutine executes an adatom deactivation process
!Surface type is changed to 3 and new rate is set for x,y and chosen
!----------------------------------------------------------------------

subroutine adatom_deactivation(x,y,chosen)
use surface_module
use rates_module
implicit none

integer, intent(in) :: x,y,chosen

if(surface(2,x,y).ne.red .and. surface(2,x,y) .ne. light_red .and. surface(2,x,y) .ne.
yellow) then
          write(*,*) "From deactivation"
          write(*,*) "what the deuce? Not an activated adatom!"
          stop
end if
if (surface(2,x,y) .eq. red) then
          surface(2,x,y) = green
          adatom_Deactivation_Count = adatom_Deactivation_Count + 1

else if (surface(2,x,y) .eq. light_red) then
          surface(2,x,y) = red
          double_Deactivation_Count = double_Deactivation_Count + 1

else if (surface(2,x,y) .eq. yellow) then
          surface(2,x,y) = light_red
          triple_Deactivation_Count = triple_Deactivation_Count + 1
else
          write(*,*) "What the deuce?  Am I anything?"
          stop
end if

call set_new_rate(x,y, reverserategrid(x,y))

end subroutine adatom_deactivation


add_adatom.f90
!This subroutine executes an add adatom to the surface process
!Surface type is chaned to 4 and nucleate is called.  If the new
!adatom is next to an exiting surface site Surface type is changed to 1
!Then a new rate is set for x,y and chosen depending on surface type

subroutine add_adatom(x,y,chosen,theCase)
use surface_module
use rates_module
implicit none
```

```
integer, intent(in) :: x,y,chosen,theCase
logical :: can_stick_north,can_stick_east,can_stick_south,can_stick_west
if(surface(2,x,y).ne.magenta .and. surface(2,x,y).ne.red &
          .and. surface(2,x,y) .ne. light_red .and. surface(2,x,y) .ne. yellow) then
          write(*,*) "what the deuce? Not an activated surface!"
        write(*,*) "surface type is:",surface(2,x,y)
          stop
end if

select case (theCase)
          case (1)
                    surface(2,x,y) = green
                    adatom_Adsorption_Count = adatom_Adsorption_Count + 1
          case (2)
                    surface(2,x,y) = red
                    CH2_Adsorption_Count = CH2_Adsorption_Count + 1
          case (3)
                    surface(2,x,y) = light_red
                    CH_Adsorption_Count = CH_Adsorption_Count + 1
          case (4)
                    surface(2,x,y) = yellow
                    C_Adsorption_Count = C_Adsorption_Count + 1
          case default
                    write (*,*) "What the deuce?  Something broke..."
                    stop
end select
surface(1,x,y) = surface(1,x,y) + 1

if (can_stick_north(x,y).or.can_stick_east(x,y)&
.or.can_stick_south(x,y).or.can_stick_west(x,y)) then
          if (surface(2,x,y) .eq. green) then
                    surface(2,x,y) = grey
          else
                    surface(2,x,y) = magenta
          end if
          er = er + 1
end if

call set_new_rate(x,y,reverserategrid(x,y))

if (isWriting) then
  call visual(x,y,0,0,1)
end if

end subroutine add_adatom


betascission.f90
!-----------------------------------------------------------------------------
!         betascission() executes a betascission process.  Surface changed
!         to 1 and new rate set for x,y,chosen
!-----------------------------------------------------------------------------
subroutine betascission(x,y,chosen)
use surface_module
use rates_module
implicit none

integer, intent(in) :: x,y,chosen


surface(1,x,y) = surface(1,x,y) - 2
surface(2,x,y) = magenta
call set_new_rate(x,y,reverserategrid(x,y))
beta_Count = beta_Count + 1

if (isWriting) then
  call visual(x,y,0,0,4)
end if

end subroutine betascission


boundary.f90
!This subroutine imposes boundary conditions for 8 positions relative to x,y
!         8  1  2    - here X is the atom at position (x,y)
!         7  X  3
!         6  5  6

subroutine boundary(x, y, xn, yn, cardinal)
use general_module
implicit none

integer, intent(in) :: x,y,cardinal

integer, intent(out)  :: xn, yn
```

```
 if (cardinal.eq.1) then
   xn=x
   yn=y+1
   if (yn.gt.grid_y) yn=yn-grid_y
 else if (cardinal.eq.2) then
   xn = x+1
   yn = y+1
   if (xn.gt.grid_x) xn=xn-grid_x
   if (yn.gt.grid_y) yn=yn-grid_y
 else if (cardinal.eq.3) then
   xn = x+1
   yn = y
   if (xn.gt.grid_x) xn=xn-grid_x
 else if (cardinal.eq.4) then
   xn = x+1
   yn = y-1
   if (xn.gt.grid_x) xn=xn-grid_x
   if (yn.lt.1) yn=yn+grid_y
 else if (cardinal.eq.5) then
   xn = x
   yn = y-1
   if (yn.lt.1) yn=yn+grid_y
 else if (cardinal.eq.6) then
    xn = x-1
    yn = y-1
    if (xn.lt.1) xn=xn+grid_x
    if (yn.lt.1) yn=yn+grid_y
 else if (cardinal.eq.7) then
    xn = x-1
    yn = y
    if (xn.lt.1) xn=xn+grid_x
 else if (cardinal.eq.8) then
    xn = x-1
    yn = y+1
    if (xn.lt.1) xn=xn+grid_x
    if (yn.gt.grid_y) yn=yn-grid_y
 end if


end subroutine


can_functions.f90
!boolean function that returns true is (x,y) can beta
logical function can_beta(x,y)
use surface_module
use general_module
implicit none
integer, intent(in) :: x,y
integer :: xn, yn

can_beta = .false.
call get_neighbour(x,y)
if (grid_x .gt. 1 .and. grid_y .gt. 1) then
          if (surfnn(1) .eq. -2 .and. surfnn(2) .eq. -2 .and. surfnn(3).eq.-2 .and.
surfnn(4).eq. -2 .and. surface(1,x,y).ge.2) then
                    can_beta = .true.
          end if
end if
if (grid_y.le.1) then
          if (surfnn(2).le.-2.and.surfnn(4).le.-2.and.surface(1,x,y).ge.2)then
                    can_beta = .true.
          end if
end if
if (grid_x.le.1) then
          if (surfnn(1).le.-2.and.surfnn(3).le.-2.and.surface(1,x,y).ge.2) then
                    can_beta = .true.
          end if
end if


end function can_beta
!boolean function that returns true is (x,y) can jump
logical function can_jump(x,y)
use surface_module
use general_module
implicit none

integer, intent(in) :: x,y

integer :: xn, yn, jumpnum,ii
logical :: onedim
can_jump = .false.


jumpnum = 0
call get_neighbour(x,y)
```

```
if (grid_x .le. 1 .and. grid_y .gt. 1) then
          if (surfnn(1) .lt. 0) jumpnum = jumpnum +1
          if (surfnn(3) .lt. 0) jumpnum = jumpnum + 1
else if (grid_y .le. 1 .and. grid_x .gt. 1) then
          if (surfnn(2) .lt. 0) jumpnum = jumpnum +1
          if (surfnn(4) .lt. 0) jumpnum = jumpnum + 1
else if (grid_y .gt. 1 .and. grid_x .gt. 1.) then
          do ii = 1 ,4
                    if (surfnn(ii) .lt. 0) jumpnum = jumpnum +1
          end do
else
          jumpnum = 0
          write(*,*) "Why did this happen in can_jump?"
end if

if (grid_y .le. 1 .or. grid_x .le. 1 .and. jumpnum .ge. 1) then
          can_jump = .true.
else if (grid_y .gt.1 .and. grid_x .gt. 1 .and. jumpnum .ge. 2) then
          can_jump = .true.
else
          can_jump = .false.
end if

if (surface(1,x,y) .eq. 0) can_jump = .false.

end function can_jump


!boolean function that returns true if (x,y) can migrate east
logical function can_migrate_east(x,y)
use surface_module
use general_module
implicit none
integer, intent(in) :: x,y
integer :: xn, yn
logical is_radical

can_migrate_east = .false.
call boundary(x, y, xn, yn, 3)
!write(*,*) "Xn,Yn from mig_east",xn,yn
if (is_radical(xn,yn).and. (surface(1,xn,yn).lt.surface(1,x,y)).and.grid_x.gt.1)
can_migrate_east = .true.
end function can_migrate_east


!boolean function that returns true if (x,y) can migrate north
logical function can_migrate_north(x,y)
use surface_module
use general_module
implicit none
integer, intent(in) :: x,y
integer :: xn, yn
logical is_radical

can_migrate_north = .false.
call boundary(x, y, xn, yn, 1)
!write(*,*) "Xn,Yn from mig_north",xn,yn
if (is_radical(xn,yn) .and. (surface(1,xn,yn).lt.surface(1,x,y)).and.grid_y.gt.1)
can_migrate_north = .true.
end function can_migrate_north


!boolean function that returns true is (x,y) can migrate_south
logical function can_migrate_south(x,y)
use surface_module
use general_module
implicit none
integer, intent(in) :: x,y
integer :: xn, yn
logical is_radical
can_migrate_south = .false.
call boundary(x, y, xn, yn, 5)
!write(*,*) "Xn,Yn from mig_south",xn,yn
if (is_radical(xn,yn) .and. (surface(1,xn,yn).lt.surface(1,x,y)).and.grid_y.gt.1)
can_migrate_south = .true.

end function can_migrate_south


!boolean function that returns true is (x,y) can migrate_west
logical function can_migrate_west(x,y)
use surface_module
use general_module
implicit none
integer, intent(in) :: x,y
integer :: xn, yn
```

```
logical is_radical
can_migrate_west = .false.
call boundary(x, y, xn, yn, 7)
!write(*,*) "Xn,Yn from mig_west",xn,yn
if (is_radical(xn,yn) .and. (surface(1,xn,yn).lt.surface(1,x,y)).and.grid_x.gt.1)
can_migrate_west = .true.
end function can_migrate_west


!boolean function that returns true is (x,y) can stick
logical function can_stick_east(x,y)
use surface_module
use general_module
implicit none
integer, intent(in) :: x,y
integer :: xn, yn
can_stick_east = .false.
call boundary(x, y, xn, yn, 3)
if (surface(1,xn,yn) .ge. surface(1,x,y).and.grid_x.gt.1) can_stick_east = .true.
end function can_stick_east


!boolean function that returns true is (x,y) can stick
logical function can_stick_north(x,y)
use surface_module
use general_module
implicit none
integer, intent(in) :: x,y
integer :: xn, yn

can_stick_north = .false.
call boundary(x, y, xn, yn, 1)
if (surface(1,xn,yn) .ge. surface(1,x,y).and.grid_y.gt.1) can_stick_north = .true.

end function can_stick_north
!boolean function that returns true is (x,y) can stick_south
logical function can_stick_south(x,y)
use surface_module
use general_module
implicit none
integer, intent(in) :: x,y
integer :: xn, yn

can_stick_south = .false.
call boundary(x, y, xn, yn, 5)
if (surface(1,xn,yn) .ge. surface(1,x,y).and.grid_y.gt.1) can_stick_south = .true.

end function can_stick_south
!boolean function that returns true is (x,y) can stick_west
logical function can_stick_west(x,y)
use surface_module
use general_module
implicit none
integer, intent(in) :: x,y
integer :: xn, yn


can_stick_west = .false.
call boundary(x, y, xn, yn, 7)
if (surface(1,xn,yn) .ge. surface(1,x,y).and.grid_x.gt.1) can_stick_west = .true.
end function can_stick_west


!boolean function
logical function is_radical(x,y)
use surface_module
use general_module
implicit none
integer, intent(in) :: x,y
is_radical = .false.
if ((surface(2,x,y) .eq. magenta) .or. (surface(2,x,y) .eq. red) &
.or. (surface(2,x,y) .eq. light_red).or. (surface(2,x,y) .eq. yellow)) is_radical =
.true.
!write(*,*) "X,Y from is_radical",x,y,is_Radical,surface(2,x,y)
end function is_radical



etch_adatom.f90
!This subroutine executes an adatom etching process
!Surface type is chaned to 2 and 1 element is subtracted from
!the surface count array for (x,y), and new rate is set for x,y and chosen
!nchosen is used becuase etching is not the fist process of it's type

subroutine etch_adatom(x,y,chosen)
use surface_module
```

```
use rates_module
implicit none

integer, intent(in) :: x,y,chosen

if(surface(2,x,y) .ne. magenta .and. surface(2,x,y) .ne. red&
          .and. surface(2,x,y) .ne. light_red .and. surface(2,x,y) .ne. yellow) then
         write(*,*) "From etch with love"
           write(*,*) "what the deuce? Not an activated adatom!"
           stop
end if
if(surface(1,x,y) < 0) write (*,*) "Surface < 0, can't etch"
if(surface(1,x,y) .eq. 0) then
    write(*,*) "Hmmm this shouldn't etch"
    stop
end if
if(surface(1,x,y) > 0) then
           surface(2,x,y) = magenta
           surface(1,x,y) = surface(1,x,y) - 1
           etch_Count = etch_Count + 1
           if (isWriting) then
                     call visual(x,y,0,0,2)
           end if
end if

call set_new_rate(x,y,reverserategrid(x,y))

end subroutine etch_adatom


etch_rate.f90
subroutine etch_rate(NN,theRate)
use initial_module
use general_module
implicit none

integer, intent(in) :: NN
real(kind=8), intent(out) :: theRate
integer :: ddG

ddG = 4*4184

if (Etch .ne. 0) then
  theRate = (1.38E-23 * Ts / 6.63E-34) * EXP(-(Eetch + NN*ddG)/ (8.314 * Ts))
end if

end subroutine etch_rate


execute_rate.f90
!This subroutine is for executing a chosen ratetype.  Each process
!is an individual subroutine to enable ease of adding new processes

subroutine execute_rate(x, y, chosen)
use general_module
use rates_module
use surface_module
implicit none

integer, intent(in) :: x, y,chosen
!write (*,*) ratetype,x,y,surface(1,x,y)
select case(ratetype)
           case(1)
                     call surface_activation(x,y,chosen)
                     call update_neighbour(x,y)
           case(2)
                     call surface_deactivation(x,y,chosen)
                     call update_neighbour(x,y)
           case(3)
                     call add_adatom(x,y,chosen,1)
                     call randomise()
                     call update_neighbour(x,y)
           case(4)
                     call adatom_activation(x,y,chosen)
                     call update_neighbour(x,y)
           case(5)
                     call etch_adatom(x,y,chosen)
                     call randomise()
                     call update_neighbour(x,y)
           case(6)
                     call adatom_deactivation(x,y,chosen)
                     call update_neighbour(x,y)
!         case(7)
!                    call migrate(x,y,chosen)
!                    call randomise()
           case(8)
                     call betascission(x,y,chosen)
```

```
                call randomise()
                call update_neighbour(x,y)
        case(9)
                call add_adatom(x,y,chosen,2)
                call randomise()
                call update_neighbour(x,y)
        case(10)
                call add_adatom(x,y,chosen,3)
                call randomise()
                call update_neighbour(x,y)
        case(11)
                call add_adatom(x,y,chosen,4)
                call randomise()
                call update_neighbour(x,y)
        case(12)
                call add_adatom(x,y,chosen,5)
                call randomise()
                write(*,*) "Something messed up in the execute rate case selection!"
        case(13)
                call add_adatom(x,y,chosen,6)
                call randomise()
                write(*,*) "Something messed up in the execute rate case selection!"
        case(14)
                call add_adatom(x,y,chosen,7)
                call randomise()
                write(*,*) "Something messed up in the execute rate case selection!"
        case(15)
                call stick(x,y,chosen)
                call randomise()
                call update_neighbour(x,y)
        case(71)
                call migrate(x,y,chosen,1)    !Migrate North
                call randomise()
                call update_neighbour(x,y)
        case(72)
                call migrate(x,y,chosen,3)    !Migrate North
                call randomise()
                call update_neighbour(x,y)
        case(73)
                call migrate(x,y,chosen,5)    !Migrate North
                call randomise()
                call update_neighbour(x,y)
        case(74)
                call migrate(x,y,chosen,7)    !Migrate North
                call randomise()
                call update_neighbour(x,y)
        case default
                write(*,*) "Something messed up in the execute rate case selection!"
end select

end subroutine


general_module.f90
!This module provides a general global module for variables and
!constants used in many subroutines.

module general_module
implicit none
save

real(kind=8), parameter :: kb = 1.3806503e-23
real(kind=8), parameter :: h = 6.626068e-34
real(kind=8), parameter :: rc = 8.31447215
real(kind=8), parameter :: temp = 917.12
!real(kind=8), parameter :: Tns = 1173
!real(kind=8), parameter :: Ts = 1173
integer, parameter :: num_rts_per_site = 25!7

integer :: grid_x
integer :: grid_y
integer :: mcsteps
integer :: ratetype
integer :: n
integer :: x_do
integer :: y_do
integer :: whoami
integer :: lowest_num

real(kind=8) :: TotalTime
real(kind=8) :: endTime
real(kind=8) :: dt
real(kind=8) :: betarate
real(kind=8) ::  Fmr
real(kind=8) :: surfaceActivate
real(kind=8) :: surfaceDeactivate
real(kind=8) :: CH3add
```

```
real(kind=8) :: CH2add
real(kind=8) :: CHadd
real(kind=8) :: Cadd
real(kind=8) :: CH2insert
real(kind=8) :: CHinsert
real(kind=8) :: Cinsert
real(kind=8) :: adatomActivation
real(kind=8) :: adatomEtch
real(kind=8) :: adatomDeactivation
real(kind=8) :: adatomMigration
real(kind=8) :: SAMigration
real(kind=8) :: aveheight,rmsdh,rms,kurt
real(kind=8) :: A_k1, Ea_k1
real(kind=8) :: A_km1, Ea_km1
real(kind=8) :: Aetch, Eetch
real(kind=8) :: A_k2
real(kind=8) :: Ea_beta
real(kind=8) :: e_factor
real(kind=8) :: output_Time_Step

logical :: isRandom
logical :: isVisual
logical :: insertion
end module general_module


get_neighbour.f90
!This subroutine returns an array called surfnn(4).  Each element
!represents a cardinal direction for the point (x,y)
SUBROUTINE get_neighbour(x,y)

use surface_module

implicit none

integer, intent(in) ::  x,y


integer :: xnew,ynew
surfnn = 0
xnew=1
ynew=1
call boundary (x,y,xnew,ynew,1)
     surfnn(1)  = surface(1,xnew,ynew) - surface(1,x,y)
call boundary (x,y,xnew,ynew,3)
      surfnn(2)  = surface(1,xnew,ynew) - surface(1,x,y)
call boundary (x,y,xnew,ynew,5)
      surfnn(3)  = surface(1,xnew,ynew) - surface(1,x,y)
call boundary (x,y,xnew,ynew,7)
      surfnn(4)  = surface(1,xnew,ynew) - surface(1,x,y)


END SUBROUTINE get_neighbour


initialise_rates.f90
!This subroutine initialises the rates, rategrid, and
!reverserategrid arrays
subroutine initialise_rates()
use general_module
use rates_module
implicit none


integer :: i,j,k,ii
rates = 0;rategrid = 0;reverserategrid = 0

isWriting = isVisual

ii = 1    !ii = keeps track of multiple rates for one grid point

do k = 1, grid_y
  do j = 1, grid_x
          rates(ii) = surfaceActivate
        rategrid(1,ii) = j
        rategrid(2,ii) = k
        rategrid(3,ii) = 1
          reverserategrid(j,k) = ii
        ii = ii + 1
          do i = 1, num_rts_per_site - 1
                  rategrid(1,ii) = j
          rategrid(2,ii) = k
                    rategrid(3,ii) = 0
                    ii = ii + 1
          end do
  end do
end do
```

```
end subroutine initialise_rates


initialise_variables.f90
subroutine initialise_variables()
use general_module
use surface_module
implicit none


surface_Migration_Count = 0; adatom_Adsorption_Count =0; etch_Count = 0
surface_Activation_Count=0;surface_Deactivation_Count=0;adatom_Activation_Count=0;adatom_
Deactivation_Count=0
beta_Count = 0;double_Activation_Count=0;double_Deactivation_Count = 0
triple_Activation_Count=0;triple_Deactivation_Count = 0
lh = 0; er = 0

end subroutine initialise_variables


initial_module.f90
module initial_module
implicit none
save

real(kind=8) :: CHxconc,CH3conc,CH2conc,CHconc,Cconc,Hconc,H2conc,Ts,Tns
real(kind=8) :: k1,k2,km1,km2,k3,k4,k14,k5,k6,k7
real(kind=8) :: MCH3,MCH2,MCH,MC,Par,sCH3,gCH3,sCH2,gCH2,sCH,gCH,sC,gC,v
real(kind=8) :: Fyuri,Fbutler,Fbr
real(kind=8) :: CH3impactrate,CH2impactrate,CHimpactrate,Cimpactrate
real(kind=8) :: activaterate,deactivaterate
real(kind=8) :: Cinsertionrate,CHinsertionrate,CH2insertionrate
real(kind=8) :: kmig, Amig,Emig,ksmig,dbmigrate,migrate,migratio
real(kind=8) :: etchrate,etchfactor,dcalc, Fsp3
real(kind=8) :: hoppingrate,stickprob,stickfactor,CCbondlength
character(len=10) :: model,defmodel
integer :: SurfAct, SurfDeAct, Add, Etch,AddAct,AddDeAct,Mig,beta
end module initial_module


init_random_seed.f90
!This subroutine is call at the start of the program to make
!the pseudo random number generator more random by seeding
!it from the clock each time the program is called

SUBROUTINE init_random_seed()
IMPLICIT NONE

INTEGER :: i, n, clock
INTEGER, DIMENSION(:), ALLOCATABLE :: seed

CALL RANDOM_SEED(size = n)
ALLOCATE(seed(n))

CALL SYSTEM_CLOCK(COUNT=clock)

seed = clock + 37 * (/ (i - 1, i = 1, n) /)
CALL RANDOM_SEED(PUT = seed)

DEALLOCATE(seed)
END SUBROUTINE



locate.f90
!This subroutine finds a number u, in an ordered sum array x
!and returns index k such than x(k-1)< u <= x(k+1)
SUBROUTINE locate(x, u, k, n)

DOUBLE PRECISION,INTENT(IN)   :: u
INTEGER,INTENT(IN)            :: n

DOUBLE PRECISION, DIMENSION(n),intent(in)         :: x

INTEGER, INTENT(OUT) :: k
INTEGER :: i,j
k = 1
if (u == 0.0) k = n + 1

do
          if (k > n) exit
          if (x(k) >= u)      exit
          k = k+1
end do
!write (*,*) n, k, u
```

```
END SUBROUTINE locate


main.f90
!-------------------------------------------------------------------------------
!                  Simplified 3-D kinetic Monte Carlo simulation
!                  of growth of CVD diamond on the (100) surface
!
!                                       v 2.0 (beta)
!
!         Author - Jeff Rodgers
!       Date   - 4 Oct 2013
!
!       main.f90 is the main program from which the simulation starts and ends
!
!       Description -   This program simulates the growth of CVD diamond on
!                       the (100) surface. Many of the rate constant in the
!                       catalogue are taken from the simplified 2-D model
!                       from the paper 'J. Appl. Phys. 108 (2010) 114909'.
!                       New to this model is etching modeled as an activated
!                       process, with an exponential dependene on bonding to
!                       nearest neighbours
!
!-------------------------------------------------------------------------------


program KMC

use general_module            !Environment modules loaded
use rates_module
use surface_module

implicit none

real(kind=8) :: ratesum, ran1,ran2

integer ::          i,j,k,cnt,chosen,prev_chosen,time_temp
integer, allocatable, dimension(:,:) :: height_arr

TotalTime = 0;chosen=0;dt = 0;lowest_num = 2;time_temp = 1

open(unit=18,file="adatom.txt")         !Open output streams to print what's
                                        !going on during the program run!
open(unit=9,file="test.out")    !test.out now deprecated
open(unit=29,file="visual.out")
open(unit=39,file="growth_vs_time.txt")
open(unit=61,file="roughness_plot.txt")
open(unit=20,file="main_output.txt")

write (20,*) ,"-----------------------------------------------------------------"
call read_input_file()
call read_energy_file()
call paulsrates()
call initialise_variables()
write (20,*),"-----------------------------------------------------------------"

n = num_rts_per_site*grid_x*grid_y      !max number of posible rates(6 per grid site)

allocate(surface(3,grid_x,grid_y)); surface = 1
allocate(rategrid(3,n ))
allocate(reverserategrid(grid_x,grid_y ))
allocate(rates(n))
allocate(rsv(n))
allocate(height_arr(grid_x,grid_y))

call initialise_rates()
surface(1,:,:) = 0
if (isRandom) CALL init_random_seed()             !Random seed can be turned on or off
with boolean from input file

!The main Monte Carlo loop begins here
!This is where the magic happens!
mcsteps = 1;cnt=1
chosen = 1
prev_chosen = 1

rsv = 0                 !Rate Sum Vector(rsv), ordered sum of rates
rsv(1) = rates(1)
do j = 2,n
          rsv(j) = rsv(j-1)+rates(j)
end do

do while (TotalTime < endTime)
          ratesum = sum(rates)
         !Rate Sum Vector(rsv), ordered sum of rates
          if (lowest_num .eq. 1) then
```

```
                    rsv(1) = rates(1)
                    lowest_num = 2
          end if
          do j = lowest_num,n
                    rsv(j) = rsv(j-1)+rates(j)
          end do
          call random_number(ran1)
          ran2 = ran1 * ratesum
          call locate(rsv, ran2, chosen, n)
          lowest_num = 0
          if (chosen > n) then
                    print *, "All of your rates are now zero"
                    goto 999
          end if
          x_do = rategrid(1,chosen); y_do = rategrid(2,chosen);ratetype = rategrid(3,
chosen)
          prev_chosen = chosen

          call execute_rate(x_do,y_do,chosen)
          call update_time(ran1, ratesum)
          height_arr =  surface(1,:,:)
          if (TotalTime .gt. (time_temp*output_Time_Step)) then
                    call stats(height_arr)
                    write(61,*) TotalTime,",",mcsteps,",",rmsdh,",",rms
                    write(39,*) TotalTime, (0.08917*0.001*aveheight*3600)/TotalTime
                    write(18,*)
TotalTime,adatom_Adsorption_Count,etch_Count,surface_Activation_Count,surface_Deactivatio
n_Count,&
adatom_Activation_Count,adatom_Deactivation_Count,surface_Migration_Count,beta_Count,doub
le_Activation_Count,&
double_Deactivation_Count,triple_Activation_Count,triple_Deactivation_Count,CH2_Adsorptio
n_Count,CH_Adsorption_Count,&
C_Adsorption_Count

                    time_temp = time_temp + 1
          end if
!                   write(9,*)
mcsteps,ratetype,TotalTime,adatom_Adsorption_Count,etch_Count,surface_Activation_Count,su
rface_Deactivation_Count,&
!adatom_Activation_Count,adatom_Deactivation_Count,surface_Migration_Count,beta_Count,dou
ble_Activation_Count,&
!double_Deactivation_Count,triple_Activation_Count,triple_Deactivation_Count,CH2_Adsorpti
on_Count,CH_Adsorption_Count,&
!C_Adsorption_Count

          mcsteps = mcsteps + 1
          cnt = cnt + 1
end do    !This is the end of one MC step
999 print *, "End of Program"

call write_output()

!Deallocate all allocatable arrays
deallocate(surface,rategrid,reverserategrid, rates, height_arr)
!Close all output streams
close(18);close(29);close(39);close(61);close(20);close(9)

!An awk script is called to make visual.out look more appealing to movie.py
          call system('awk -f vis.awk visual.out > tmp')
          call system('mv tmp visual.out')
          call system('mv visual.out visualise')
          close(29)

end program KMC


migrate.f90
!This subroutine executes a migration process.  A species can migriate
!in a maximum of 4 possible directions.  If more than one direction a
!random number is used to choose which.


subroutine migrate(x,y,chosen,direction)
use surface_module
use rates_module
implicit none

integer, intent(in) :: x,y,chosen,direction
integer :: xn,yn
logical :: lemming_stick

lemming_stick = .false.

call boundary(x,y,xn,yn,direction)

if (surface(1,x,y) - surface(1,xn,yn) .gt. 1) then
          lemming_stick = .true.
```

```
end if

surface(2,x,y) = magenta
surface(1,x,y) = surface(1,x,y) - 1
call set_new_rate(x,y,reverserategrid(x,y))

surface(2,xn,yn) = red
surface(1,xn,yn) = surface(1,xn,yn) + 1
if (lemming_stick) surface(2,xn,yn) = grey
call set_new_rate(xn,yn,reverserategrid(xn,yn))

!write(18,*) "height",surface(1,x,y)+1,"height",surface(1,xn,yn) - 1

surface_Migration_Count = surface_Migration_Count + 1

if (isWriting) then
        call visual(x,y,xn,yn,3)
end if

end subroutine migrate


randomise.f90
subroutine randomise()
use initial_module
use general_module
use surface_module
use rates_module
implicit none

integer, dimension(:), allocatable :: arr
integer :: x,y,ii,how_many, rad,thenum
real(kind=8) :: ran

!write (*,*) "Before"
!write (*,*) surface(2,:,:)
how_many =0
rad = 0
do x = 1, grid_X
          do y = 1, grid_y
                    if (surface(2,x,y) .eq. grey .or. surface(2,x,y) .eq. magenta) then
                              if (surface(2,x,y) .eq. magenta) then
                                        rad = rad + 1
                              end if
                              surface(2,x,y) = 0
                              how_many = how_many + 1
                    end if
          end do
end do
allocate(arr(how_many))
!write (*,*) 100*real(rad)/real(how_many)
arr = grey
do while (rad > 0)
          call random_number(ran)
          thenum=int(ran*how_many)+1
          if (arr(thenum) .eq. grey) then
                    arr(thenum) = magenta
                    rad = rad - 1
          end if
end do
if (rad > 0)write(*,*) "Rad after", rad
ii = 1
do x = 1, grid_X
          do y = 1, grid_y
                    if (surface(2,x,y) .eq. 0) then
                              surface(2,x,y) = arr(ii)
                              ii = ii + 1
                              call set_new_rate(x,y,reverserategrid(x,y))
                              call update_neighbour(x,y)
                    end if
          end do
end do
deallocate(arr)

!write (*,*) "After"
!write (*,*) surface(2,:,:)
end subroutine


rates_list.f90
subroutine paulsrates()
use initial_module
use general_module
implicit none


!--------------calculate starting parameters
```

```
!chemical reactions defined as:
!  (1)    H(g)  +  CdH  =  H2(g)  + Cd
!  (2)    H(g)  +  cd   =  CdH
!  (3)    CH3(g) + Cd-Cd = CH2-Cd-CdH
!  (4)    CHx(g) + Cd-Cd  = CH(x-1)-Cd-CdH

CHxconc = CH2conc + CHconc + Cconc
!H abstraction rate constant, reaction (1)
k1 = A_k1 * (Tns) ** .5 * EXP(-Ea_k1 / Ts)  !units cm3 s-1 (values from our JAP 2007
paper)

!H2 addition to surface radical rate constant, reverse of reaction (1)
km1 = A_km1 * (Tns) ** .5 * EXP(-Ea_km1 / Ts)

!H addition to surface radical rate constant, reaction (2)
k2 = A_k2 * (Tns) ** .5

!Backward step, i.e. desorption of H from C-H surface, reverse of (2),
!assuming CH bond energy barrier is 413 kJ/mol and pre-exp factor is 1e13 s-1
!and that it is Arrhenius.  km2 ~ 0 for all Ts.
km2 = (1E+13 / 6.023E+23) * EXP(-413000 / (8.314 * Ts))

!CH3 insertion into surface dimer radical rate constant, reaction (3)
k3 = 2.4E-13 * (Tns) ** .5

!CHx insertion into dimer radical, reaction (4), is same as that for CH3
k4 = k3

!Rate constant for defect formation (Butler)
k14 = 1.12E+16 * EXP(-201600 / (8.314 * Ts)) / Ts

! fraction of open (monorad) sites
Fyuri = 1 / (1 + .3 * EXP(3430 / Ts) + .1 * EXP(-4420 / Ts) * H2conc / Hconc)
Fbutler = k1 / (k1 + k2)     ! simplified version of Butler!s model, from JAP 99 104907
IF (model == "yuri") THEN      !Yuri!s model
  Fmr = Fyuri
ELSE                           !Butler!s model
  Fmr = Fbutler
END IF
Fbr = Fmr * Fmr              ! no. biradical sites

!CH3 impact rate
MCH3 = 15                                                          ! mass of CH3 in g
Par = sCH3 * gCH3                                                  ! Sticking coefficient
for CH3 addition
v = 100 * (8000 * 8.314 * Tns / (3.142 * MCH3)) ** .5               ! velocity term of
CH3 in cm/s
CH3impactrate = (Par * CH3conc * v * .25) / 1.56E+15               ! on all sites

!CH2 impact rate
MCH2 = 14                                                           ! mass of CH2 in g
Par = sCH2 * gCH2                                                   ! Sticking
coefficient for CH2 addition
v = 100 * (8000 * 8.314 * Tns / (3.142 * MCH2)) ** .5                ! velocity term of
CH2 in cm/s
CH2impactrate = (Par * CH2conc * v * .25) / 1.56E+15                ! on all sites

!CH impact rate
MCH = 13                                                            ! mass of CH in g
Par = sCH * gCH                                                     ! Sticking
coefficient for CH addition
v = 100 * (8000 * 8.314 * Tns / (3.142 * MCH)) ** .5                 ! velocity term of
CH in cm/s
CHimpactrate = (Par * CHconc * v * .25) / 1.56E+15                  ! on all sites

!C impact rate
MC = 12                                                             ! mass of C in g
Par = sC * gC                                                       ! Sticking
coefficient for C addition
v = 100 * (8000 * 8.314 * Tns / (3.142 * MC)) ** .5                  ! velocity term of C
in cm/s
Cimpactrate = (Par * Cconc * v * .25) / 1.56E+15                    ! on all sites

!surface CH2 activation rate
activaterate = k1 * Hconc + km2

!surface CH2* deactivation rate
deactivaterate = km1 * H2conc + k2 * Hconc

!C insertion rate constant
k5 = 8.587E-11 * EXP(-19836 / (8.314 * Ts))       !Based on Arrhenius fit to James model
Cinsertionrate = k5 * Cconc

!CH insertion rate constant
k6 = EXP(2000000 * (1 / Ts) ** 2 - (1868.7 / Ts) - 24.923)    !Based on Arrhenius fit to
James model
```

```
CHinsertionrate = k6 * CHconc

!CH2(s) insertion rate constant
k7 = k6                                 !using same fit as for CH
CH2insertionrate = k7 * CH2conc * .01       !assuming [CH2(s)] is ~1% of [CH2]

!CH2 migration rate constant
kmig = Amig * EXP(-Emig / (8.314 * Ts))     !rate constant for hopping s^-1
hoppingrate = kmig * (1 - (1 - Fmr) ** 4)       !modified version of mig rate (s^-1) for
mapping 2D hops onto 1D lattice

!surface radical migration rate constant (Frenklach paper)
ksmig = 4.8 * 1E12 * EXP(-155400 / (8.314 * Ts))   !rate constant for radical hopping
if (grid_x == 1 .or. grid_y == 1) then
          dbmigrate = kmig * (1 - (1 - Fmr) ** 4)      !modified mig rate (s^-1) for
mapping 2D hops onto 1D
          IF (dbmigrate > activaterate) THEN
            migrate = dbmigrate             !CH2 migration rate same as radical mig rate
          ELSE
            migrate = activaterate          !or CH2 mig rate same as surface activation
rate if this is bigger
          END IF
          migratio = INT(hoppingrate / migrate)       !no. back & forth hops it'll make
before a new radical is created
else
          migrate = kmig
end if

!etching rate constant
!etchrate = Aetch * DEXP(-Eetch / (8.314d0 * Ts))
!etchfactor = 1.569E5 * EXP(-128400.0 / (8.314 * Ts))
!etchfactor = e_factor                          !etchrate is 3.3x less than growth rate
(approx)
!etchrate = etchfactor * CH3impactrate
!etchrate = (1.38E-23 * Ts / 6.63E-34) * EXP(-NN*Eetch / (8.314 * Ts))
call etch_rate(0,etchrate)

!beta-scission rate constant (Jeremy)
betarate = (1.38E-23 * Ts / 6.63E-34) * EXP(-Ea_beta / (8.314 * Ts))

if (SurfAct .eq. 0) then
          surfaceActivate = 0.0
else
          surfaceActivate = activaterate
end if

if (SurfDeAct .eq. 0) then
          surfaceDeactivate = 0.0
else
          surfaceDeactivate = deactivaterate
end if

if (Add .eq. 0)then
          CH3add = 0.0
          CH2add = 0.0
          CHadd = 0.0
          Cadd = 0.0
          CH2insert = 0.0
          CHinsert = 0.0
          Cinsert = 0.0
else
          CH3add = CH3impactrate
          CH2add = CH2impactrate
          CHadd = CHimpactrate
          Cadd = Cimpactrate
          CH2insert = CH2insertionrate
          CHinsert = CHinsertionrate
          Cinsert = Cinsertionrate
end if

if (AddAct .eq.0) then
          adatomActivation = 0.0
else
          adatomActivation = activaterate
end if

if (AddDeAct .eq. 0) then
          adatomDeactivation = 0.0
else
          adatomDeactivation = deactivaterate
end if

if (Etch .eq. 0) then
          adatomEtch = 0.0
else
          adatomEtch = etchrate
end if
```

```
if (Mig .eq. 0) then
        adatomMigration = 0.0
else
        adatomMigration = migrate
end if
if (beta .eq. 0) betarate = 0.0

write (20,'(a20,f15.5)') "Surface Activation", surfaceActivate
write (20,'(a20,f15.5)') "Surface Deactivation", surfaceDeactivate
write (20,'(a20,f15.5)') "Add CH3 rate",CH3add
write (20,'(a20,f15.5)') "Add CH2 rate",CH2add
write (20,'(a20,f15.5)') "Add CH rate",CHadd
write (20,'(a20,f15.5)') "Add C rate",Cadd
write (20,'(a20,f15.5)') "Adatom Activation", adatomActivation
write (20,'(a20,f15.5)') "Adatom Deactivation", adatomDeactivation

write (20,'(a20,f15.5)') "Etch rate",adatomEtch
write (20,'(a20,f15.5)') "Migration rate",adatomMigration
write (20,'(a20,f15.5)') "Beta-Scission rate",betarate




end subroutine paulsrates


rates_module.f90
module rates_module
implicit none
save

integer, dimension(:,:), allocatable :: rategrid
integer, dimension(:,:) , allocatable :: reverserategrid
real(kind=8), dimension(:), allocatable :: rates, rsv

logical :: isWriting

end module rates_module


read_energy_file.f90
!Does what it says!
subroutine read_energy_file()
use initial_module
use general_module
implicit none

character(150) :: rubbish

open(unit=8,file="energy.txt")

read (8,*) rubbish
read (8,*) rubbish
read (8,*) A_k1, Ea_k1
read (8,*) rubbish
read (8,*) A_km1, Ea_km1
read (8,*) rubbish
read (8,*) Aetch, Eetch
read (8,*) rubbish
read (8,*) A_k2
read (8,*) rubbish
read (8,*) Amig, Emig
read (8,*) rubbish
read (8,*) e_factor
read (8,*) rubbish
read (8,*) Ea_beta


END subroutine read_energy_file


read_input_file.f90
!Does what it says!
subroutine read_input_file()
use initial_module
use general_module
implicit none

character(150) :: rubbish

open(unit=8,file="input.txt")

read (8,*) rubbish
```

```
read (8,*) rubbish
read (8,*) SurfAct, SurfDeAct,Add,Etch,AddAct,AddDeAct,Mig,beta
read (8,*) rubbish
read (8,*) isRandom
read (8,*) rubbish
read (8,*) insertion
read (8,*) rubbish
read (8,*) model
read (8,*) rubbish
read (8,*) defmodel
read (8,*) rubbish
read (8,*) Ts
read (8,*) rubbish
read (8,*) Tns
read (8,*) rubbish
read (8,*) Hconc
read (8,*) rubbish
read (8,*) H2conc
read (8,*) rubbish
read (8,*) CH3conc,sCH3,gCH3
read (8,*) rubbish
read (8,*) CH2conc,sCH2,gCH2
read (8,*) rubbish
read (8,*) CHconc,sCH,gCH
read (8,*) rubbish
read (8,*) Cconc,sC,gC
read (8,*) rubbish
read (8,*) grid_x
read (8,*) rubbish
read (8,*) grid_y
read (8,*) rubbish
read (8,*) endTime
read (8,*) rubbish
read (8,*) output_Time_Step
read (8,*) rubbish
read (8,*) isVisual

END subroutine read_input_file


set_new_rate.f90
!fter a rate is executed on a point element. The rates affected by this
!change are updated in the catalouge

!bulk diamond lattice (not surface blocks) ----------> 0 (Not yet added)

!surface group --------------------------------------> grey - 1
!activated surface group ----------------------------> magenta - 2
!temporarily adsorbed CH2 not yet activated   -------> green - 3
!singly-activated surface CH2 which can migrate -----> red - 4
!doubly-activated surface CH which can migrate ------> light red - 5
!triply-activated surface C which can migrate -------> yellow - 6

subroutine set_new_rate(x,y,chosen)
use general_module
use rates_module
use surface_module
implicit none

logical :: can_migrate, can_jump, can_stick,can_beta,&
can_migrate_north,can_migrate_east,can_migrate_south,can_migrate_west,&
can_stick_north,can_stick_east,can_stick_south,can_stick_west

integer :: neigh_par,tmp

integer, intent(in) :: x, y, chosen

integer :: which,ii

which = surface(2,x,y)

do ii = chosen, chosen + (num_rts_per_site - 1)
          rategrid(3,ii ) = 0
          rates(ii ) = 0.0
end do

neigh_par = 0
call get_neighbour(x,y)
do ii = 1, 4
        tmp = surfnn(ii)
        if (tmp .ge. 0) then
                neigh_par = neigh_par + tmp
        end if
end do


call etch_rate(neigh_par,adatomEtch)
```

```
!write(*,*) adatomEtch, neigh_par

if (chosen .lt. lowest_num .or. lowest_num .eq. 0) lowest_num = chosen
if (which .eq. grey) then                          !grey
          rategrid(3,chosen) = 1
          rates(chosen) = surfaceActivate
!-------------------------------------------------------------------
else if (which .eq. magenta) then                  !magenta
          rategrid(3,chosen) = 2
          rates(chosen) = surfaceDeactivate
          rategrid(3,chosen + 1) = 3
          rates(chosen + 1) = CH3add
          rategrid(3,chosen + 2) = 5
          if (can_jump(x,y) .and. surface(1,x,y) .gt. 1) then
                    rates(chosen + 2) = 0.00
                    if (surface(1,x,y) == 0 ) write(*,*) "Hmmm? You settin' the wrong
rate"
          else if (surface(1,x,y) .gt. 1) then
                    rates(chosen + 2) = adatomEtch/5000
        else
              rates(chosen + 2) = 0.0
          end if
          rategrid(3,chosen + 3) = 9
          rates(chosen + 3) = CH2add
          rategrid(3,chosen + 4) = 10
          rates(chosen + 4) = CHadd
          rategrid(3,chosen + 5) = 11
          rates(chosen + 5) = Cadd
          if (insertion) then
                    rategrid(3,chosen + 6) = 12
                    rates(chosen + 6) = CH2insert
                    rategrid(3,chosen + 7) = 13
                    rates(chosen + 7) = CHinsert
                    rategrid(3,chosen + 8) = 14
                    rates(chosen + 8) = Cinsert
          end if
          rategrid(3,chosen + 9) = 8
          if (can_beta(x,y)) rates(chosen + 9) = betarate
!-------------------------------------------------------------------------
else if (which .eq. green) then                    !green
          rategrid(3,chosen) = 4
          rates(chosen) = adatomActivation
          if (insertion) then
                    rategrid(3,chosen + 1) = 12
                    rates(chosen + 1) = CH2insert
                    rategrid(3,chosen + 2) = 13
                    rates(chosen + 2) = CHinsert
                    rategrid(3,chosen + 3) = 14
                    rates(chosen + 3) = Cinsert
          end if
!-------------------------------------------------------------------------
else if (which .eq. red) then           !red
          rategrid(3,chosen) = 6
          rates(chosen) = adatomDeactivation
          rategrid(3,chosen + 1) = 3
          rates(chosen + 1) = CH3add
          rategrid(3,chosen + 2) = 9
          rates(chosen + 2) = CH2add
          rategrid(3,chosen + 3) = 10
          rates(chosen + 3) = CHadd
          rategrid(3,chosen + 4) = 11
          rates(chosen + 4) = Cadd
          rategrid(3,chosen + 5) = 5
          rates(chosen + 5) = adatomEtch
          rategrid(3,chosen + 6) = 4
          rates(chosen + 6) = adatomActivation
          rategrid(3,chosen+7) = 71
          if (can_migrate_north(x,y)) rates(chosen + 7) = adatomMigration
          rategrid(3,chosen+8) = 72
          if (can_migrate_east(x,y)) rates(chosen + 8) = adatomMigration
          rategrid(3,chosen+9) = 73
          if (can_migrate_south(x,y)) rates(chosen + 9) = adatomMigration
          rategrid(3,chosen+10) = 74
          if (can_migrate_west(x,y)) rates(chosen + 10) = adatomMigration
          rategrid(3,chosen+11) = 15
          if (can_stick_north(x,y)) rates(chosen + 11) = adatomMigration
          rategrid(3,chosen+12) = 15
          if (can_stick_east(x,y)) rates(chosen + 12) = adatomMigration
          rategrid(3,chosen+13) = 15
          if (can_stick_south(x,y)) rates(chosen + 13) = adatomMigration
          rategrid(3,chosen+14) = 15
          if (can_stick_west(x,y)) rates(chosen + 14) = adatomMigration
          rategrid(3,chosen + 15) = 8
          if (can_beta(x,y)) rates(chosen + 15) = betarate
!-------------------------------------------------------------------------
else if (which .eq. light_red) then
```

```
          rategrid(3,chosen) = 6
          rates(chosen) = adatomDeactivation
          rategrid(3,chosen + 1) = 3
          rates(chosen + 1) = CH3add
!         rategrid(3,chosen + 3) = 9
!         rates(chosen + 3) = CH2add
!         rategrid(3,chosen + 4) = 10
!         rates(chosen + 4) = CHadd
          rategrid(3,chosen + 2) = 11
          rates(chosen + 2) = Cadd
          rategrid(3,chosen + 3) = 5
          rates(chosen + 3) = adatomEtch
          rategrid(3,chosen + 4) = 4
          rates(chosen + 4) = adatomActivation
        rategrid(3,chosen+5) = 15
        if (can_stick_north(x,y)) rates(chosen + 5) = adatomMigration
        rategrid(3,chosen+6) = 15
        if (can_stick_east(x,y)) rates(chosen + 6) = adatomMigration
        rategrid(3,chosen+7) = 15
        if (can_stick_south(x,y)) rates(chosen + 7) = adatomMigration
        rategrid(3,chosen+8) = 15
        if (can_stick_west(x,y)) rates(chosen + 8) = adatomMigration

!-------------------------------------------------------------------------
else if (which .eq. yellow) then
          rategrid(3,chosen) = 6
          rates(chosen) = adatomDeactivation
          rategrid(3,chosen + 1) = 3
          rates(chosen + 1) = CH3add
!         rategrid(3,chosen + 2) = 9
!         rates(chosen + 2) = CH2add
!         rategrid(3,chosen + 3) = 10
!         rates(chosen + 3) = CHadd
          rategrid(3,chosen + 4) = 11
          rates(chosen + 4) = Cadd
          rategrid(3,chosen + 5) = 5
          rates(chosen + 5) = adatomEtch
        rategrid(3,chosen+6) = 15
        if (can_stick_north(x,y)) rates(chosen + 6) = adatomMigration
        rategrid(3,chosen+7) = 15
        if (can_stick_east(x,y)) rates(chosen + 7) = adatomMigration
        rategrid(3,chosen+8) = 15
        if (can_stick_south(x,y)) rates(chosen + 8) = adatomMigration
        rategrid(3,chosen+9) = 15
        if (can_stick_west(x,y)) rates(chosen + 9) = adatomMigration

end if
end subroutine


stats.f90
subroutine stats(ht_arr)
use general_module
use surface_module
implicit none


integer :: i,j,k
real(kind=8) :: latt,CC100dist,rmstemp,r,htmp
integer, intent(in), dimension(grid_x,grid_y) :: ht_arr

rmstemp = 0.0
htmp=0
r=0.0
do i = 1, grid_x
          do j = 1, grid_y
                    htmp = htmp +  ht_arr(i,j)
!         write(*,*) htmp, ht_arr(1,i)
          end do
end do
aveheight = real(htmp)/real(grid_x*grid_y)
do i = 1, grid_x
          do j = 1, grid_y
!         write(*,*) ht_arr(1,i)
                    r = real((ht_arr(i,j)-aveheight)**2)
                    rmstemp = rmstemp + r
          end do
end do
rmsdh = sqrt(rmstemp/real(grid_x*grid_y))

r = 0.0
rmstemp = 0.0
do i = 1, grid_x
          do j = 1, grid_y
!         write(*,*) ht_arr(1,i)
                    r = real((ht_arr(i,j))**2)
                    rmstemp = rmstemp + r
```

```
          end do
end do
rms = sqrt((1/real(grid_x * grid_y))*rmstemp)


end subroutine stats


stick.f90
!This subroutine executes a migration process.  A species can migriate
!in a maximum of 4 possible directions.  If more than one direction a
!random number is used to choose which.


subroutine stick(x,y,chosen)
use surface_module
use rates_module
implicit none

integer, intent(in) :: x,y,chosen
integer :: xn,yn

if (surface(2,x,y) .eq. red) then
          surface(2,x,y) = grey
else
          surface(2,x,y) = magenta
end if
lh = lh + 1
surface_Migration_Count = surface_Migration_Count + 1
call set_new_rate(x,y,reverserategrid(x,y))
call update_neighbour(x,y)
end subroutine stick


surface_activation.f90
subroutine surface_activation(x,y,chosen)
use surface_module
use rates_module
implicit none

integer, intent(in) :: x,y,chosen
integer :: i
if(surface(2,x,y).ne.grey) then
          write(*,*) "what the deuce? Not a deactivated surface!"
          write(*,*) "surface type is:", surface(2,x,y)
          stop
end if
surface(2,x,y) = magenta
call set_new_rate(x,y, reverserategrid(x,y))

surface_Activation_Count = surface_Activation_Count + 1

end subroutine surface_activation


surface_deactivation.f90
subroutine surface_deactivation(x,y,chosen)
use surface_module
use rates_module

implicit none

integer, intent(in) :: x,y,chosen

integer :: xn, yn, ii
if(surface(2,x,y).ne.magenta) then
          write(*,*) "what the deuce? Not an activated surface!"
          write(*,*) "surface type is:",surface(2,x,y)
          stop
end if
surface(2,x,y) = grey
call set_new_rate(x,y, reverserategrid(x,y))
surface_Deactivation_Count = surface_Deactivation_Count + 1

end subroutine surface_deactivation


surface_module.f90
module surface_module
implicit none
save

integer, parameter :: grey = 1
integer, parameter :: magenta = 2
integer, parameter :: green = 3
integer, parameter :: red = 4
```

```
integer, parameter :: light_red = 5
integer, parameter :: yellow = 6

integer, dimension(:,:,:), allocatable :: surface
real(kind=8), dimension(:,:), allocatable :: xyz
integer, dimension(4) :: surfnn,bounds,sbounds
integer :: er, lh

integer :: adatom_Adsorption_Count
integer :: etch_Count
integer :: surface_Activation_Count
integer :: surface_Deactivation_Count
integer :: adatom_Activation_Count
integer :: adatom_Deactivation_Count
integer :: surface_Migration_Count
integer :: beta_Count
integer :: double_Activation_Count
integer :: double_Deactivation_Count
integer :: triple_Activation_Count
integer :: triple_Deactivation_Count
integer :: CH2_Adsorption_Count
integer :: CH_Adsorption_Count
integer :: C_Adsorption_Count


end module surface_module


update_neighbour.f90
!This subroutine returns an array called surfnn(4).  Each element
!represents a cardinal direction for the point (x,y)
SUBROUTINE update_neighbour(x,y)

use surface_module
use rates_module
implicit none

integer, intent(in) ::  x,y


integer :: xn,yn
call boundary(x,y,xn,yn,1)
call set_new_rate(xn,yn,reverserategrid(xn,yn))
call boundary(x,y,xn,yn,3)
call set_new_rate(xn,yn,reverserategrid(xn,yn))
call boundary(x,y,xn,yn,5)
call set_new_rate(xn,yn,reverserategrid(xn,yn))
call boundary(x,y,xn,yn,7)
call set_new_rate(xn,yn,reverserategrid(xn,yn))

call set_new_rate(x,y,reverserategrid(x,y))

END SUBROUTINE update_neighbour


update_time.f90
subroutine update_time(ran,ratesum)
use general_module
implicit none

real(kind=8), intent(in) :: ran,ratesum

dt = -log(ran)/ratesum
TotalTime = TotalTime + dt

end subroutine


visual.f90
!This subroutine adds to visualisation list

subroutine visual(x,y,xn,yn,addortake)  !,beta)
use surface_module
use rates_module
implicit none

integer, intent(in) :: x,y,xn,yn,addortake
select case(addortake)
          case(1)
                    write(29,*) "Add", x,y,surface(1,x,y) + 1
          case(2)
                    write(29,*) "Take", x,y,(surface(1,x,y) + 1) + 1
          case(3)
                    write(29,*) "Add", xn,yn,surface(1,xn,yn)+1, "Take",
x,y,(surface(1,x,y) + 1)+1
          case(4)
```

```
                    write(29,*) "Take", x,y,surface(1,x,y)+1+1, "Take",
x,y,(surface(1,x,y) + 2)+1
end select
end subroutine visual


write_output.f90
subroutine write_output()
use general_module
use surface_module
use rates_module
implicit none


integer :: i,j,k,littlestep,step,cnt,themin,themax,thedim
real(kind=8) :: latt,CC100dist,rmstemp,r,htmp
integer, dimension(grid_x,grid_y) :: height_arr

open(unit=11,file="surf.out")

CC100dist = 0.08917 !distance between (100) layers in nm
latt = 1.5
themin = minval(surface(1,:,:))
themax = maxval(surface(1,:,:))
height_arr =  surface(1,:,:)
call stats(height_arr)
write(20,*) "Min", themin
write(20,*) "Max", themax
write(20,*) "avergae height and rms"
write (20,*) "Average Height" , aveheight
write (20,*) "Roughness",rmsdh*CC100dist,"nm"
!write(20,*) sqrt(rmstempm15.0)
!TotalTime = TotalTime / 60 / 60
write(20,*)"----------------------------------------------------------------"
write(20,*) "Surface Activation Happend",  surface_Activation_Count,&
 "times",100*real(surface_Activation_Count)/real(mcsteps)
write(20,*) "Surface Deactivation Happend",surface_Deactivation_Count,"times"&
,100*real(surface_Deactivation_Count)/real(mcsteps)
write(20,*)"Adatom Activation Happend",adatom_Activation_Count,"times"&
,100*real(adatom_Activation_Count)/real(mcsteps)
write(20,*) "Adatom Deactivation Happend",adatom_Deactivation_Count, "times"&
,100*real(adatom_Deactivation_Count)/real(mcsteps)
write(20,*)"Adatom Double Activation Happend",double_Activation_Count, "times"&
,100*real(double_Activation_Count)/real(mcsteps)
write(20,*)"Adatom Double Deactivation Happend",double_Deactivation_Count, "times"&
,100*real(double_Deactivation_Count)/real(mcsteps)
write(20,*)"Adatom Triple Activation Happend",triple_Activation_Count, "times"&
,100*real(triple_Activation_Count)/real(mcsteps)
write(20,*)"Adatom Triple Deactivation Happend",triple_Deactivation_Count, "times"&
,100*real(triple_Deactivation_Count)/real(mcsteps)
write(20,*) "Migration Happend",surface_Migration_Count, "times"&
,100*real(surface_Migration_Count)/real(mcsteps)
write(20,*) "CH3 Adsorption Happend",adatom_Adsorption_Count, "times"&
,100*real(adatom_Adsorption_Count)/real(mcsteps)
write(20,*) "CH2 Adsorption Happend",CH2_Adsorption_Count, "times"&
,100*real(CH2_Adsorption_Count)/real(mcsteps)
write(20,*) "CH_Adsorption Happend",CH_Adsorption_Count, "times"&
,100*real(CH_Adsorption_Count)/real(mcsteps)
write(20,*) "C_Adsorption Happend",C_Adsorption_Count, "times"&
,100*real(C_Adsorption_Count)/real(mcsteps)
write(20,*) "Desorption Happend",etch_Count, "times"&
,100*real(etch_Count)/real(mcsteps)
write(20,*) "Beta Scission Happend",beta_Count, "times"&
,100*real(beta_Count)/real(mcsteps)
write(20,*) "Total = ", surface_Migration_Count + adatom_Adsorption_Count +&
 etch_Count+surface_Activation_Count+surface_Deactivation_Count&
+adatom_Activation_Count+adatom_Deactivation_Count+beta_Count+double_Activation_Count+&
double_Deactivation_Count + triple_Activation_Count + triple_Deactivation_Count&

+CH2_Adsorption_Count+ CH_Adsorption_Count+C_Adsorption_Count, mcsteps
write(20,*)"----------------------------------------------------------------"
write(20,*)  "Growth Rate (um/hr):",(CC100dist*0.001*aveheight*3600)/TotalTime
write(20,*)  "Total Simulation time:",TotalTime,"secs"

999 print *, "End of Program"
step = maxval(surface(1,:,:))
step = step + 1+1
write(20,*) step
allocate(xyz(3,grid_x*grid_y*step))
cnt = 1
xyz = 0
do i = 1, grid_x
  do j = 1, grid_y
    do k = themin , themax
      xyz(1,cnt) = i*latt
      xyz(2,cnt) = j*latt
      if (k < surface(1,i,j)) then
```

```
        xyz(3,cnt) = k*latt
      else
        xyz(3,cnt) = surface(1,i,j)*latt
      end if
      cnt = cnt + 1
   end do
  end do
end do
Open (unit = 53, file="surface.xyz")
write(53,*) cnt-1
write(53,*) "comment line"
do i = 1, cnt-1
    Write (53,*) "C",xyz(1,i),xyz(2,i),xyz(3,i)
end do
close(53)
write(20,*) "Number of L-H type processes", lh, "Percentage", 100.0*real(lh)/real(lh+er)
write(20,*) "Number of E-R type processes", er, "Percentage", 100.0*real(er)/real(lh+er)
write(20,*) lh, er
write(11,*) "{"
do i = 1, grid_x
  write(11,*) "{", height_arr(i,:),"}"
end do
 write(11,*) "}"
close(11)
deallocate(xyz)
end subroutine write_output
```

Activation energies and prefactors
!H abstraction rate constant, reaction (1) : A_k1, Ea_k1
3.2E-12,3430
!H2 addition to surface radical rate constant, reverse of reaction (1) : A_km1, Ea_km1
3.2e-13,7850
!Etching
1.33e+16,239500
!H addition to surface radical rate constant, reaction (2) : A_k2
9.6e-13
A and Ea for migration (s-1 and J/mol)
6.13e13, 128400
!etchfactor - a percentage of the CH3 addition rate: e_factor
0.3
!beta-scission rate constant (Jeremy): Ea_beta
180000

```
Input file for Growth simulation program
SurfAct, SurfDeAct, Add, Etch, Ad. Act, Ad. DeAct, mig, beta
1,1,1,1,1,1,1,1
Random Seed (logical T/F)
.true.
Insertion reactions on(logical T/F)
.false.
model for radical site density (yuri or butler)
yuri
model for defect density (yuri or butler)
yuri
substrate temp Ts in Kelvin
1173
gas temp Tns near the surface in Kelvin
1267
H atom concentration at surface (cm-3)
1.85E+14
H2 molecule conc at surface (cm-3)
1.52E+17
CH3 conc at surface (cm-3)   s   and  g factors
1.46E+13 , 0.5, 0.15
CH2 conc at surface (cm-3)   s   and  g factors
3.66E+08 , 0.6, 0.2
CH  conc at surface (cm-3)   s   and  g factors
2.74E+08 , 0.7, 0.25
C   conc at surface (cm-3)   s   and  g factors
3.37E+09 , 1.0, 0.3
grid_x
50
grid_y
50
End Time
51.0
Output Time Step
0.1
visualisation
.true.
```